Investigating the Single Crystal to Single Crystal Transformations of Highly Porous Metal-Organic Frameworks Through the Crystalline Sponge Method

by

Gabriel Brunet

A thesis submitted in conformity with the requirements
for the degree of Master of Science in Chemistry

Department of Chemistry and Biomolecular Sciences
University of Ottawa

Investigating the Single Crystal to Single Crystal Transformations of Highly Porous Metal-Organic Frameworks Through the Crystalline Sponge Method

Gabriel Brunet

Master of Science in Chemistry

Department of Chemistry and Biomolecular Sciences
University of Ottawa

2016

Abstract

The development of a new technique capable of analyzing compounds crystallographically without first needing to crystallize them has been recently described. The present thesis aims to demonstrate the potential of such a technique, which utilizes crystalline sponges, in order to regularly order guest compounds in a porous media. The structural stability of the molecular sponges, which are highly porous metal-organic frameworks (MOFs), is first investigated, revealing that the Co-based MOF, **1**, undergoes two remarkable transformations. This thesis also demonstrates how the technique can be employed to visualize the motion and occupancy of gaseous guests in a MOF. The Zn-based MOF, **4**, was found to physisorb and chemisorb molecular iodine, leading to the formation of a variety of polyiodide species. The flexible nature of the host was determined to be an essential component in the exceptionally large iodine uptake capacity of the MOF. These results illustrate that the crystalline sponge method can be an effective strategy for directly visualizing guest molecules and obtaining vital information on the interactions formed between the host and guest.

Acknowledgments

I would like to express my most sincere gratitude to my supervisor, Prof. Muralee Murugesu, whom I have had the pleasure of working with from my undergraduate studies to the completion of my Masters degree. I have highly appreciated the guidance and support you have given me in developing my capacities as a chemist and a researcher. I am extremely proud of being the first from our group to submit a thesis related to metal-organic frameworks, a topic which I am now very passionate about. I would like to commend my supervisor for his diverse expertise and identifying the potential impact of these materials. I have thoroughly enjoyed the numerous clever analogies you have shared with us over the past few years.

I would like to recognize the contributions of Dr. Ilia Korobkov, our X-ray crystallographer. Much of this work was dependent on the X-ray results, and I am very grateful for having someone with your skills participate so actively in my research. I wish you a lot of success in your new position.

I would also like to thank our collaborators Prof. Tom Woo and Mohammad Aghaji for their highly insightful computational work. Sincere thanks to Prof. Yaroslav Fillinchuk and Dr. Koen Robeyns for my research stay in Belgium, in addition to assisting me with X-ray absorption spectroscopy.

Finally, I would like to thank all previous and current lab group members for their input on this work, including Dr. Fatemah Habib who taught me the basics of scientific research. A special mention to Dr. Damir Safin for helping out in the early stages of the research and providing invaluable insight. I also thank Dr. Amélie Pialat for her assistance with TGA measurements. I would also like to recognize Katie Harriman for her entertaining song selections during lab sessions, and for being such a great person to talk to. Finally, I am very grateful to Rebecca Holmberg, who has been an amazing colleague and friend to work with throughout my graduate studies.

Table of Contents

Contents

Acknowledgments iii

Table of Contents iv

List of Tables vii

List of Figures viii

List of Appendices xi

Chapter 1: Introduction 1

- 1.1 Porous materials 1
- 1.2 Zeolites 3
- 1.3 Covalent Organic Frameworks 7
- 1.4 Metal-Organic Frameworks 11
- 1.5 The Crystalline Sponge Method and Single-Crystal to Single-Crystal Transformations 15
- 1.6 References 18

Chapter 2: The Hidden Transformations of a Molecular Sponge 21

- 2.1 Introduction 22
- 2.2 Experimental section 25
  - 2.2.1 General considerations 25
  - 2.2.2 Synthesis 25
  - 2.2.3 Physical measurements 26
  - 2.2.4 Single Crystal X-ray Diffraction Studies 27
  - 2.2.5 Magnetic measurements 30
- 2.3 Results and discussion 31
  - 2.3.1 Synthesis 31

2.3.2 Structural analysis ... 33

2.3.3 IR spectroscopy analysis ... 42

2.3.4 Thermogravimetric analysis ... 44

2.3.5 Diffuse reflectance spectroscopy analysis ... 45

2.3.6 Magnetic properties ... 48

2.4 Conclusion ... 53

2.5 References ... 55

Chapter 3: Exceptionally High Iodine Uptake in a Metal-Organic Framework Visualized Through Stepwise Crystallographic Transformations ... 59

3.1 Introduction ... 60

3.2 Experimental section ... 63

3.2.1 General considerations ... 63

3.2.2 Synthesis ... 63

3.2.3 Physical measurements ... 65

3.2.4 Single Crystal X-ray Diffraction Studies ... 65

3.2.5 Computational studies ... 66

3.3 Results and discussion ... 67

3.3.1 Synthesis ... 67

3.3.2 First structural intermediate ... 68

3.3.3 Second structural intermediate ... 72

3.3.4 Third structural intermediate ... 76

3.3.5 Diffuse reflectance spectroscopy analysis ... 81

3.4 Conclusion ... 83

3.5 References ... 85

Chapter 4: Metallocene and Organic Guest Inclusion in a Porous Coordination Network as Evidenced by the Crystalline Sponge Method for X-ray Analysis ... 87

4.1 Introduction ... 88

4.2 Experimental section 90

4.2.1 Synthesis 90

4.2.2 Physical measurements 92

4.2.3 Single Crystal X-ray Diffraction Studies 92

4.3 Results and discussion 92

4.3.1 Synthesis 92

4.3.2 Ferrocene inclusion 93

4.3.3 Ferrocene carboxaldehyde inclusion 96

4.3.4 Ethylbenzene and styrene inclusion 98

4.4 Conclusion 101

4.5 References 102

Chapter 5: Conclusion 104

5.1 Conclusion and outlook 104

Appendices 107

List of Tables

Table 1 Summary of the crystal structure data and refinement for compounds **1a**, **1b** and **3** 30

Table 2 Selected bond distances (Å) and angles (°) for **1b** 37

Table 3 Selected bond distances (Å) and angles (°) for **3** 42

Table 4 Summary of the crystal structure data and refinement for compounds **4–7** 66

Table 5 Assignment, occupancy and bond distances of iodine guests in compound **5**................ 70

Table 6 Assignment, occupancy and bond distances of iodine guests in compound **6**................ 73

Table 7 Assignment, occupancy and bond distances of iodine guests in compound **7**................ 79

Table 8 Summary of metallocene uptake by MOFs... 89

Table 9 Summary of the crystal structure data and refinement for compounds **8–11** 93

Table 10 Bond distances of ferrocene in compound **8** 95

List of Figures

Figure 1. The designable features of porous materials ... 2

Figure 2. Tetrahedral coordination environment of metallic ions (i.e. Si^{4+}) found in zeolites. Example of the corning sharing connectivity between tetrahedral ... 4

Figure 3. Schematic representation of zeolite A ... 6

Figure 4. Systematic increases in the number of publications on the topic of metal-organic frameworks ... 12

Figure 5. Schematic representation of the crystalline sponge method, where a MOF single-crystal is treated with a drop of liquid guest and subsequently analyzed by X-ray diffraction ... 16

Figure 6. Picture of single crystals of **1b-3** and their corresponding transformations viewed under optical microscope at room temperature ... 26

Figure 7. X-ray powder diffraction patterns for the semi-amorphous compound **2** (purple), and microcrystalline pale pink powder, identified as **3** (blue). The simulated diffraction patterns for **1b** (black) and **3** (red) are also displayed ... 32

Figure 8. Photos highlighting the gradual transformation of three crystals of **1b** to **2** over time, with varying crystallinities and morphologies, as viewed under optical microscope at room temperature 33

Figure 9. Stick and space-filling model of the $[Co_6(NCS)_{12}(TPT)_4]$ octahedral cage found in **1b** (M_6L_4) ... 35

Figure 10. Partially labeled molecular structure of the $[Co(NCS)_2(TPT)_4]$ fragment illustrating the octahedral coordination environment of the cobalt metal centers ... 35

Figure 11. Molecular fragment of **1b**, illustrating the coordination environments of the two crystallographically different cobalt centers ... 36

Figure 12. Stick model of the $[Co_{12}(NCS)_{24}(TPT)_8]$ cuboctahedral cage found in **1b** ($M_{12}L_8$) viewed along two different directions. The space filling model is also shown to display the accessibility of the pore for guest molecules ... 37

Figure 13. Stick and space-filling model of the $[Co_{12}(NCS)_{24}(TPT)_{24}]$ octahedral cage found in **1b** ($M_{12}L_{24}$) ... 38

Figure 14. Partially labeled molecular structure of the $[Co(NCS)_2(TPT)_2(H_2O)_2]$ molecular fragment in **3** ... 40

Figure 15. Top: Crystal packing of **3** along the *c*-axis, with the different colors (pink, cyan and orange) corresponding to a different layer. The coordination polyhedra display the location of the cobalt metal centers with respect to their sheet. Bottom: Crystal packing of **3** along the *b*-axis displaying the sheet-like arrangement 41

Figure 16. FTIR spectra of TPT (black), **1b** (red), **2** (purple) and **3** (blue) at 298 K.................. 43

Figure 17. The thermogravimetric analyses (TGA) were carried out between 25–800 ^{o}C for **1b** (black), **2** (red) and **3** (blue). Measurements were performed under nitrogen atmosphere (25 mL/min) with a heating rate of 5 ^{o}C/min.. 45

Figure 18. Normalized Kubelka-Munk spectra for TPT and **3**... 46

Figure 19. Normalized Kubelka-Munk spectra depicting the color change from orange (**1b**) to green (**2**) over time, with the black arrows displaying the significant changes in adsorption behavior.. 47

Figure 20. Temperature dependence of the magnetic susceptibility for complexes **1b–3** in a χT vs. T plot at 1000 Oe.. 49

Figure 21. Magnetization versus field measurements at 1.8, 3, 5 and 7 K for **1b**, **2** and **3**, plotted as *M* vs *H* (left) and *M* vs *H/T* (right) 50

Figure 22. Frequency dependence of the in-phase χ' (top) and out-of-phase χ'' (bottom) magnetic susceptibilities for **1b** under an applied optimum dc field of H_{dc} = 600 Oe................................ 51

Figure 23. Summary of the structural transformations observed for the molecular sponge **1b**... 53

Figure 24. Schematic representation of the contraction and expansion of the Zn-based MOF upon the removal or addition of guest substrates... 60

Figure 25. Photographs demonstrating the color change associated with the exposure of single-crystals of **4** to I_2 vapors, as viewed under optical microscope 67

Figure 26. Stick and space-filling model of a partially labeled molecular fragment of **5** emphasizing the I_2 guest which forms strong halogen-halogen interactions with the iodide ions of the framework, effectively forming an $[I_4]^{2-}$ unit.. 69

Figure 27. Packing arrangement of **5** along the *b*-axis. The two interpenetrated networks are shown in blue and orange, while the nitrobenzene and iodine guest molecules are shown in green and purple, respectively 71

Figure 28. Molecular structure of a single pore of **6**, illustrating the disordered and partially occupied I_2 guests. In the 88% occupancy case, there is the same $[I_4]^{2-}$ unit as in **5** (left), while in the 12% occupancy instance there is a chemisorbed I_3^- group along with an I_2 molecule participating in weak halogen bonding (right)... 74

Figure 29. Packing arrangement of **6** along the *b*-axis. The two interpenetrated networks are shown in blue and orange, while the nitrobenzene and iodine guest molecules are shown in green and purple, respectively 75

Figure 30. The thermogravimetric analyses (TGA) were carried out between 25–715 ^{o}C for **4** and between 25–1000 ^{o}C for **5–7** and for single crystals of **4** after 72 h of exposure to I_2. Measurements were performed under nitrogen atmosphere (25 mL/min) 77

Figure 31. X-ray crystal structure of a single pore of **4** viewed along its channel direction. Evolution of the guests, where nitrobenzene solvent molecules are sequentially exchanged for iodide species, are illustrated for the same pore following 3, 6 and 15 h of exposure time to I_2 vapors. The amount of guest molecules contained per unit cell are listed, along with changes in the space group and unit cell volumes for compounds **4–7** 78

Figure 32. Packing diagram of **7** along the *b*-axis, illustrating the two interpenetrating networks in blue and orange along with the four different pores (listed A to D) and their respective iodine guests shown in purple 80

Figure 33. Normalized Kubelka-Munk spectra of **4** saturated with I_2 followed over time at ambient conditions for a period of 120 h 82

Figure 34. FTIR spectra of **4** (black), **4** completely saturated by I_2 (red) and **4** saturated by I_2 and left at ambient conditions for 120 h (blue) 83

Figure 35. Schematic diagram demonstrating the stepwise crystallographic process employed for investigating the uptake of molecular iodine in compound **4** 84

Figure 36. Compounds that were investigated using the crystalline sponge method, by groups other than the Fujita group. 90

Figure 37. A view of two ferrocene molecules placed in the middle of the pores (left) and packing arrangement of **8** with the different guests molecules highlighted in different colors (right) 95

Figure 38. Packing arrangement of **9** along the *b*-axis (left) demonstrating the various guest molecules. Space-filling and ball-and-stick models illustrating the π-stacking of ferrocene carboxaldehyde with the TPT ligands (top and bottom right) 97

Figure 39. Packing arrangement of **10** along the *b*-axis illustrating the ethylbenzene guests in red. Molecular disorder and hydrogen atoms are omitted for clarity 99

Figure 40. Packing arrangement of **11** along the *b*-axis illustrating the styrene guests in green and the closest intermolecular short contacts. Molecular disorder and hydrogen atoms are omitted for clarity 100

List of Appendices

Appendix A: Spin-allowed transitions for octahedral high-spin Co^{II}.. 107

Appendix B: Ac checks for compounds **1b**, **2** and **3** 108

Appendix C: DFT calculations of **5**.. 109

Appendix D: DFT calculations of **6**.. 111

Appendix E: Determination of iodine content.. 113

Appendix F: Normalized Kubelka-Munk spectra of TPT, ZnI_2, **4** and I_2 114

Appendix G: Partial ^1H NMR spectra of compound **8** in DMSO 115

Appendix H: Full ^1H NMR spectra of compound **11** in DMSO 116

List of Abbreviations

2D	2-dimensional
3D	3-dimensional
ac	Alternating current
BTC	Benzene-1,3,5-tricarboxylic acid
CCDC	Cambridge Crystallographic Data Center
COF	Covalent Organic Framework
dc	Direct current
DFT	Density Functional Theory
DRS	Diffuse Reflectance Spectroscopy
ESRF	European Synchrotron Radiation Facility
EXAFS	Extended X-ray Absorption Fine Structure
FCC	Fluid Catalytic Cracking
FTIR	Fourier Transform Infrared Spectroscopy
IUPAC	International Union of Pure and Applied Chemistry
MeOH	Methanol
MOF	Metal-Organic Framework
NMR	Nuclear Magnetic Resonance
NQR	Nuclear Quadrupole Resonance
PAE	Poly(Arylene Ethylnylene)
PAF	Porous Aromatic Framework
PSM	Post-Synthetic Modification
PTFE	Polytetrafluoroethylene
PXRD	Powder X-ray Diffraction
SBU	Secondary Building Unit
SCXRD	Single-crystal X-ray Diffraction
SMM	Single Molecule Magnet
SQUID	Super-conducting Quantum Interference Device
TGA	Thermogravimetric Analysis
TPT	2,4,6-tris-(4-pyridyl)-1,3,5-triazine
TTF	Tetrathiafulvalene
UV	Ultraviolet
Å	Angstrom
cm	Centimeter
H	Magnetic field
Hz	Hertz
K	Kelvin
kcal	Kilocalorie
M	Molar concentration and magnetization
min	Minute
mL	Millilitre
mM	Millimolar
mmol	Millimole
nm	Nanometer
Oe	Oersted
T	Temperature

U_{eff}	Effective energy barrier
V	Volume
χ	Molar magnetic susceptibility
χ'	In-phase magnetic susceptibility
χ''	Out-of-phase magnetic susceptibility
br	Broad
s	Strong (IR), singlet (NMR)
m	Medium (IR)
w	Weak
d	Doublet
t	Triplet

Chapter 1

Introduction

1.1 Porous materials

The word “porous” alludes to the presence of pores or holes in a material’s surface and is a feature exhibited by a wide variety of naturally occurring substances, including minerals, clays and biological tissues. The study of naturally occurring porous minerals, namely silicates, has led to the discovery that their porous structures can be reproduced synthetically. These substances can be described in terms of their porosity, which is a measure of the voids or empty space contained within the total volume of the material. They can be further described using the International Union of Pure and Applied Chemistry (IUPAC) nomenclature for pore size, where micropores display openings of less than 2 nm, mesopores between 2 and 50 nm, and macropores for openings greater than 50 nm.[1] The inherent role of the pores is to act as a passage between the external and internal surface of a solid, allowing materials, such as gases and liquids to pass into the solid.[2] It is important to note that in order for a material to be deemed porous, two requirements must be met. First, the material must contain a large number of pores, and secondly, the pores are specifically designed to optimize or improve the performance of the material.[3] Furthermore, there are a number of key structural characteristics that must be considered for porous materials, including pore size opening, pore surface functionality and framework composition and topology (Figure 1). The pore size opening will be a major limiting factor for the intake of guests, since it will physically restrict access to the insides of the porous material. Consequently, the size and geometry of the pores should represent the starting point in determining whether porous materials can uptake specific molecules. One of the great advantages of synthetic porous materials is the ability to functionalize the surface area of the pores. The introduction of chemical functional groups will alter the interaction between the porous material and the molecules residing or passing through the cavities. At the same time, this will change the chemical composition and the molecular dimensions of the porous medium. One prevalent strategy to optimize the properties of a porous material relies on changing the functionality of the pores without changing the underlying topology.[4] This permits a systematic approach to evaluating the direct impact of a particular functional group on the properties of the porous compound.

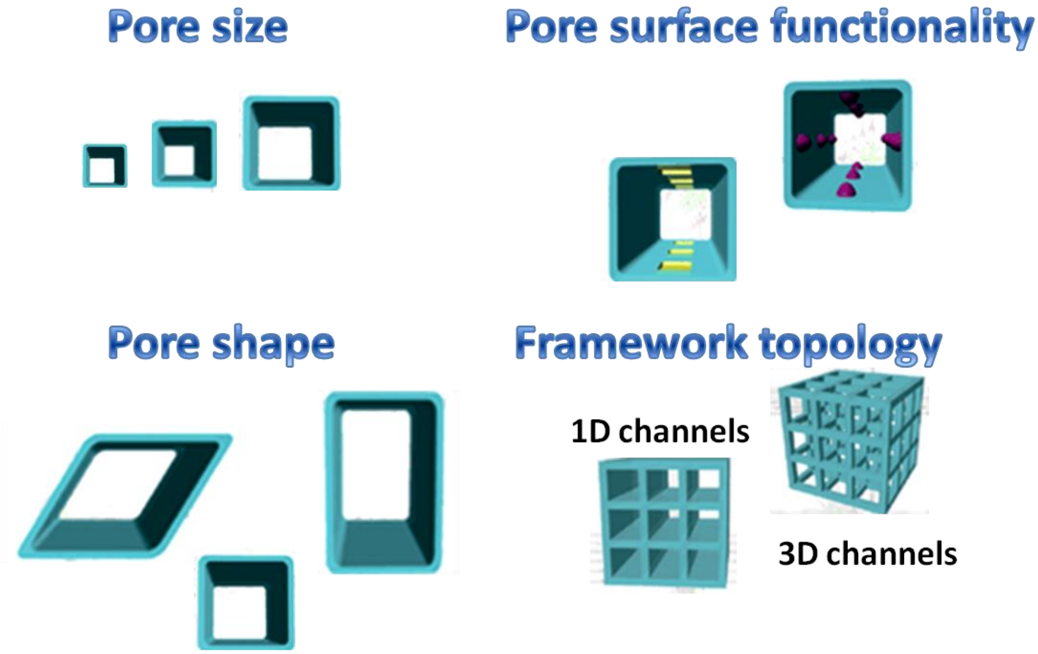

Figure 1: The designable features of porous materials. This figure is inspired by Kitagawa *et al.* (2009).[4]

Another vital structural characteristic of porous materials is their chemical composition and topology. Different topologies will necessarily lead to varying pore structures, from channels to discrete pores, and their composition will have a significant influence on the interactions between the porous material and the encroaching guest. The study of porous materials concerns itself with host-guest chemistry, which describes the fascinating structural relationships between two compounds held together by noncovalent interactions. Herein, the term “host” will refer to the material which can accommodate another compound, while the “guest” is the molecule which will become incorporated in another structure. The ability to control the arrangement of discrete molecular entities leading to permanent porosity has resulted in porous materials having a significant commercial value. The following porous solids have set the standard for the encapsulation of guest compounds, with each exhibiting unique chemical compositions and molecular structures; however they do not represent an exhaustive list or description of all porous materials.

1.2 Zeolites

Zeolites encompass a huge area of research in the field of porous materials owing to their well-established technological applications. Compared to the other porous media discussed in this thesis, zeolites are the oldest and arguably the most well-studied. The Swedish mineralogist A. F. Cronstedt is credited with the discovery of the first natural zeolite, stilbite, in 1756 and recognized that they consisted of alkali and alkaline earth metals.[5] For the next 200 years following their discovery, zeolite minerals were found to occur naturally in basaltic and volcanic rocks,[6] however due to the difficulty in the accessing these sources, their extraction for commercial purposes was considerably hampered. In the late 1950’s, the use of X-ray diffraction to examine geological rocks resulted in the discoveries of very large deposits of natural zeolites throughout the United States, namely chabazite, erionite, mordenite and clinoptilolite.[6] Currently, we have identified over 40 naturally occurring zeolite structures.[7] The first synthetic zeolite, levynite, was obtained by St Claire Deville in 1862 through hydrothermal synthesis.[8] This marked the first step in establishing a new field of materials science which is still running strong to this day. In fact, there are over 200 unique zeolite frameworks that are presently known.[7]

Structurally, zeolites are defined as crystalline aluminosilicates that contain micropores. Crystallinity refers to the high degree of structural order within the solid where the atoms and molecules are periodically arranged. Furthermore, zeolites are built exclusively from three elements: aluminum, silicon and oxygen. These atoms are arranged in tetrahedral units of $[SiO_4]^{4-}$ and $[AlO_4]^{5-}$ giving zeolite frameworks with varying chemical compositions and three-dimensional microporous structures (Figure 2). The tetrahedra are linked to each other by sharing oxygen ions. This defining feature of having extended networks made entirely from four-coordinated atoms provides a rich variety of structures that may contain large cavities or channels.

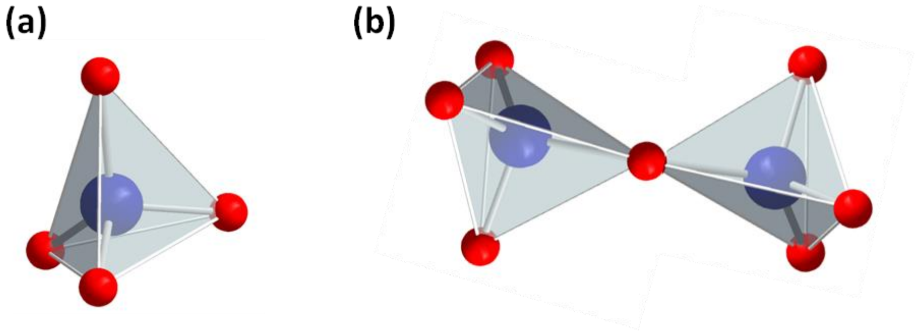

Figure 2: (a) Tetrahedral coordination environment of the metallic ions (i.e. Si^{4+}) found in zeolites. (b) Example of the corning sharing connectivity between tetrahedras.

The structural description of extended networks such as zeolites, involves the identification of the secondary building unit (SBU). In zeolites, the tetrahedra form the primary building units and their assembly results in the formation of SBUs which effectively describes the framework topology. This concept is also commonly utilized for other porous materials, including Metal-Organic Frameworks (MOFs), which will be described later on. The chemical composition of zeolites is another important parameter since it will dictate how many ions must be contained within the voids in order to balance the charges. Each $[AlO_4]^{5-}$ tetrahedron contributes one additional negative charge that is balanced by a cation residing within the porous structure. This cation can be readily be replaced by other cations, giving zeolites significant ion exchange properties. According to Lowenstein's rule, an aluminum centered tetrahedron cannot be connected to another aluminum centered tetrahedron.[9] Consequently, Al–O–Al linkages are forbidden, and aluminum atoms are surrounded by four silicon atoms. As a corollary of this, aluminosillicate zeolite structures have Si : Al ratios ≥ 1.

An important application of zeolites is found in molecular sieving materials. Their uniform pore size and high stability in a number of solvents, including water, makes them ideal separation candidates. Furthermore, by modification of the extra-framework cation, a change in the pore size dimensions can be induced. Worthy of note is Zeolite A, which, when counter-balanced by sodium, has a pore opening of approximately 4 Å. The sodium ion can easily be exchanged for the larger potassium ion, reducing the pore opening to 3 Å. This simple example illustrates the somewhat flexible nature of the zeolite framework, where the identity of the guest molecules has a direct impact on the topology of the zeolite. The number of extra-framework cations is proportional to the aluminum content of the zeolite, and thus the maximum number of cation exchange sites will be for Si : Al ratios approaching 1, as in Zeolite A (Figure 3). In the case where the negative charges of the zeolite framework are balanced by protons, the acidity of the zeolite can then be altered, leading to numerous applications among which acid catalysis plays a major role. The protons and other exchangeable cations are the acid sites within the zeolite framework, while the oxygen atoms of the lattice form the basic sites. The proton guests covalently bind to the negatively charged oxygen atoms, forming hydroxyl groups. These hydroxyl groups acts as Brønsted acid sites, capable of donating the proton to basic guest molecules. Moreover, the exchangeable cations interact with the negatively charged oxygen atoms of the lattice, through weaker electrostatic bonds, and are able to accept an electron pair rendering these sites Lewis acids.[11]

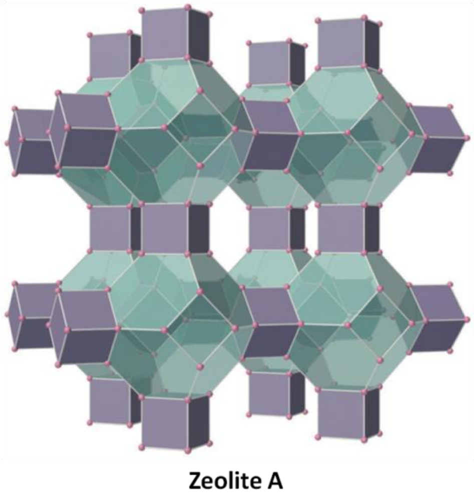

Figure 3: Schematic representation of zeolite A.[10]

In terms of current applications, zeolites are proven performers in multiple commercial products. Their ion-exchange properties are exploited in water softening, where the initial extra-framework cations (often Na^+ and K^+) are replaced by Ca^{2+} and Mg^{2+} . They are often found in detergents and washing powders in order to increase washing efficiency.[12] Similarly, they have been known to capture heavy metals and radioactive isotopes through similar mechanisms, making them useful materials in the treatment of wastewater and nuclear waste.[13] Their main commercial use however is in the field of catalysis. Their catalytic properties are based on three important characteristics previously discussed: regularity of the pores, acidity and ion-exchange capabilities. Among the various catalytic processes, fluid catalytic cracking (FCC) is one of the major applications of zeolites. Essentially, heavy oil fractions are converted into smaller, more valuable products, including gasoline and diesel.[14] The alkanes of the heavy fractions are brought into contact with the zeolite at high temperatures and produces high percentages of hydrocarbons containing 5 to 10 carbon atoms. The pore structure controls the selective formation of products in this small range and the acidic properties allow the cracking of the C–C bonds, through formation of carbenium ions. It is important to note that zeolites do display a number of advantages over other porous materials such as thermal and water stability, which is more difficult to obtain in other classes of porous frameworks. Nevertheless, they do present some limitations on the types of topologies that can be obtained, through exclusive use of tetrahedral species. Moreover, the negatively charged framework of zeolites requires cations to reside in pores or channels in order to balance the charges. While this may be advantageous for certain applications, it may also hinder others. Current research in porous materials seeks to improve on the benchmarks established by the zeolites. One such emerging material is built purely upon organic elements, in contrast to the inorganic zeolites, and are assembled to give porous crystalline polymers.

1.3 Covalent Organic Frameworks

Covalent Organic Frameworks (COFs) are a relatively new class of porous materials that are constructed from organic building units. The materials community has seen a surge of interest in this field, following the discovery of a rational synthetic route for obtaining porous organic frameworks connected *via* covalent bonds. In fact, it is only since 2005 that O. Yaghi and co-workers demonstrated the use of crystal engineering techniques for the synthesis of COF structures.[15] It is important to note that porous organic frameworks have existed for over 40 years, for example in hyper-cross-linked polymer networks,[16] however recent work has significantly reinvigorated the field. To further understand the renewed interest in porous organic frameworks, two subcategories of these materials must be introduced. The first subcategory consists of amorphous porous materials, which lack long range ordering. This leads to irregular framework topologies and a large distribution of pore sizes. Moreover, their characterization becomes a considerable challenge due to their amorphous nature, and consequently optimizing them for specific applications becomes very arduous. For these reasons, and as will be discussed in greater detail later on, the work presented herein highlights a number of single crystal structures, allowing the highest level of precision for molecular structure determination. The recent reports of porous organic frameworks as crystalline materials are partly responsible for the re-emergence of these compounds.[15,17] The difficulty in synthesizing COFs as crystalline materials arises from the strong covalent bonding, which does not permit a self-correction mechanism. In frameworks containing weaker bonding, this mechanism would allow errors in the assembly process to be corrected through repeated breaking of the bonds, permitting the growth of large single crystals. In COFs, the bonding between organic subunits is essentially irreversible, however new strategies have emerged leading to microcrystalline and even single crystal COFs.[15,17,18]

As previously mentioned, the synthesis of COFs is achieved through polymerization of organic precursors. Initially, organic polymers with COF-like topologies were obtained through Pd-catalyzed cross-coupling reactions. Terminal alkynes reacting with aromatic bromides or iodides in amine solvents would results in the formation of new C–C bonds (Scheme 1). This well-known reaction in organic chemistry is termed the Heck-Cassar-Sonogashira-Hagihara reaction.

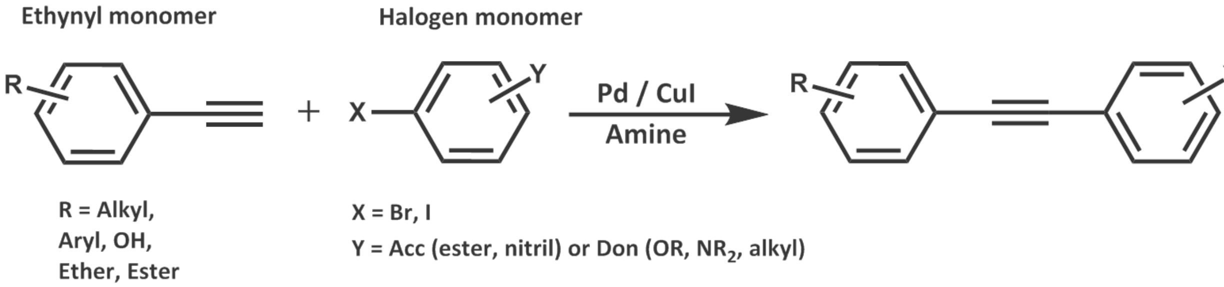

Scheme 1: Overall reaction of the Heck-Cassar-Sonogashira-Hagihara cross-coupling reaction used in the synthesis of PAEs.

Especially popular were the poly(aryleneethylnylene)s (PAEs) which were explored for their applications in light-emitting devices and sensors.[19] From the general reaction outlined in Scheme 1, the synthesis of a polymer is possible by having an additional alkyne as part of the functional group in the ethynyl monomer. This synthetic strategy would lead to a 1D chain, however, incorporation of a larger number of terminal alkynes in the ethynyl monomer would favor the formation of 2D and 3D networks. The main difficulty of PAEs for traditional porous material applications was their structural characterization. While the connectivity between organic building blocks could be easily identified, determination of the packing arrangement proved to be a more significant challenge. Indeed, the cross-coupling reactions would lead to generally amorphous compounds, due to the strong covalent C–C bonds which do not permit the self-correction mechanism, rendering structural analyses more challenging. The improvement of crystallinity was achieved through the formation of reversible covalent bonds rather than strong bonds that would lead to permanent structures. Examples of reversible covalent bonds can be found in boronic esters and imines, where the newly formed bond can be broken under certain conditions or under the action of certain external stimuli (i.e. heat). This approach was first utilized by O. Yaghi in the synthesis of COFs leading to a number of microcrystalline compounds studied through powder X-ray diffraction (PXRD).[15,20] At the time, these structures exhibited some of the highest reported surface areas along with pore sizes in the mesopore range. It is important to note that even with an improvement of the crystallinity, some structural debate remains among a few COFs solved through PXRD methods. In search of higher performing porous materials, crystal engineering plays a vital role in the design of new materials. Through accurate molecular structures, it is possible to fine-tune and tailor the framework in order to optimize the desired properties. Subsequently, the use of X-ray techniques allow the elucidation of the most accurate and reliable structural elucidation. The work presented herein has made significant usage of X-ray diffraction for the aforementioned reasons, and permits the direct observation of the guests encapsulated by the host.

The most recent approach towards enhancing crystallinity in COFs was described by J. Wuest and co-workers, and utilizes the dimerization of nitroso groups.[21] Nitroso polymerization was first observed by Nietzki and Kehrmann between two units of *p*-dinitrosobenzene, and is now known to be a reversible process (Scheme 2).[22] The Wuest group constructed a family of COFs, inspired by the nitroso polymerization reaction, spontaneously yielding large crystals suitable for single crystal X-ray diffraction. Thus, it is possible to envision new single crystal COFs with distinct properties and topologies obtained through tailoring of the organic building units.

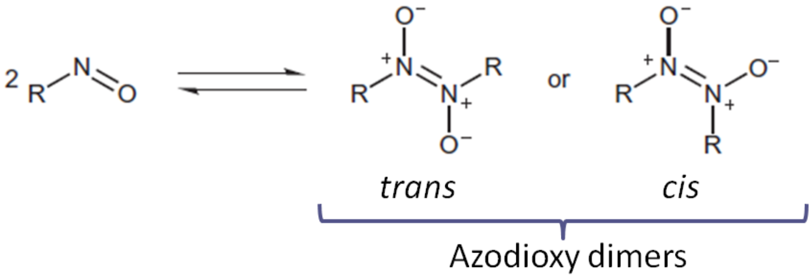

Scheme 2: Reversible dimerization of nitroso groups leading to the formation of single crystal COFs.

The performance of COFs at the current stage is far from comparable to other porous materials such as zeolites, however, these relatively new materials show great promise in a number of prominent technologies. One of the main challenges in COF chemistry is their chemical and thermal stability. With many COFs being based upon dehydration reactions (i.e. Schiff-bases and boronic esters) the presence of water can reverse the polymerization leading to destruction of the framework. Likewise, COFs display lower thermal stabilities than other well investigated porous materials. Nevertheless, being built exclusively from light weight elements offers the potential of low mass densities and low costs in comparison to other capture materials. Furthermore, COF synthesis is environmentally friendly, generally yielding non-toxic side products, such as water, and often requiring relatively small amounts of solvents.

1.4 Metal-Organic Frameworks

While the materials seen so far have concerned themselves with covalent bonds, metal-organic frameworks (MOFs) consist of a unique class of compounds, mixing both organic and inorganic components in order to generate porous structures. These hybrid organic-inorganic materials have emerged as an extensive class of solid polymeric materials with exceptional potential in numerous technological and industrial applications. Significant interest in MOFs stems from their ability to store key gases, such as hydrogen and methane, under favorable conditions as well as their selective capture of guest molecules. Of particular importance is the selective capture of CO_2 for the purification of natural gas. While other porous media, such as zeolites, are suitable for the process, the energy input required for the release of CO_2 is high leading to low energetic efficiency and high costs.[23] Therefore, MOFs offer an exciting avenue in the improvement of well-established technologies leading to reduced costs, and enhanced outputs. Other applications of MOFs include catalysis, drug delivery, sensing, luminescence and many more.

MOFs were first discovered in 1989 by R. Robsen and co-workers, highlighting their unprecedented structures.[24] Since then, countless MOFs have been synthesized, with varying compositions, pore spaces and functionalities, making it one of the most prolific areas of research in inorganic chemistry the past 15 years (Figure 4). These systems are built from coordination bonds, also known as dative covalent bonds, and are described as a Lewis base donating an electron pair to a Lewis acid. In MOF chemistry, the Lewis acid site is commonly a metal atom, while the Lewis bases are called ligands. One area which deserves specific attention is the classification of such compounds. It is important to properly distinguish the nomenclature and terminology of coordination compounds and MOFs, as it is often an area of confusion. More specifically, the criterion which distinguishes a MOF from a simple coordination polymer will be investigated. The IUPAC definition of a coordination polymer is a "coordination compound with repeating coordination entities extending in 1, 2, or 3 dimensions".[25] A subset of coordination polymers are coordination networks. Coordination networks also contain repeating entities in 1, 2, or 3 dimensions however they have the additional feature of cross-links between "individual chains, loops, or spiro-links".[25] A further subcategory of coordination networks are the MOFs themselves. In this case, the coordination network exhibits potential void space through linkages of the metal units by the organic ligands. Thus, MOFs belong to a specific category of coordination polymers that display potential porosity.

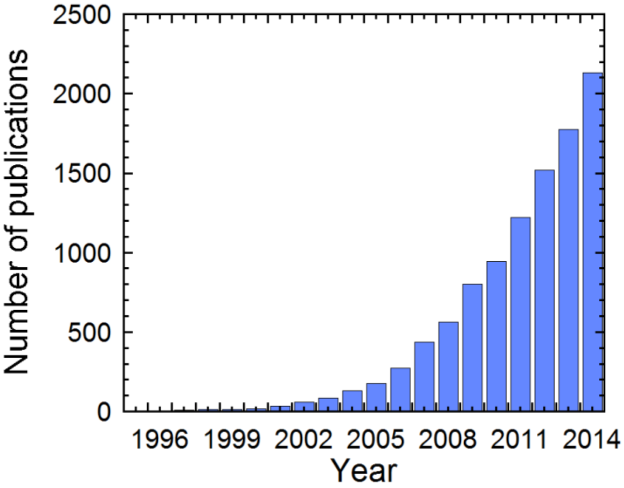

Figure 4: Systematic increases in the number of publications on the topic of metal-organic frameworks. Data were obtained by a search of the ISI Web of Knowledge in August 2015 for the keywords "metal-organic framework".

In similar fashion to zeolites, MOF structures are also described using SBU terminology. Where zeolites have restrictions on possible topologies and SBUs, dictated by their purely Si and Al composition, MOFs have nearly limitless structural potential. Furthermore, due to the weaker bonding found in coordination bonds, MOFs are often obtained as crystalline materials, reflecting their long-range periodic ordering. This is attributed to the self-correction mechanism, where errors during molecular assembly can be corrected through breaking of the bonds. MOFs are typically obtained from "one-pot" syntheses by mixing metal ions with organic ligands by method of slow diffusion or under hydrothermal and solvothermal conditions. Owing to their enormous structural and chemical diversity, a number of MOFs have been reported with large surface areas (up to 7000 m^2/g), high thermal and chemical stabilities and large void volumes (up to 90%).[26]

The main advantage of utilizing MOFs as porous materials stems from their facile functionalization. This allows a greater degree of control on the physical environment of the pores and cavities within the MOF, thereby tuning the interactions between the guest and the hosts. This conceptually simple task has led to specialized and sophisticated applications for MOF materials in multiple research areas previously mentioned. The idea is to add functional groups that would enhance the physical or chemical properties of the MOF while retaining the same framework topology. As a result, the influence of the new functionality on the properties can be directly investigated. MOF functionality is generally achieved by two methods: direct and post-synthetic methods. The direct method consists of introducing the organic precursors with the altered functionality directly in the “one-pot” procedure, hopefully reproducing an identical framework. This method relies on the use of well-defined building blocks that maintain structural integrity, and is termed reticular synthesis. The second route concerns post synthetic modifications (PSM), indicating that the framework undergoes chemical modifications after it has been successfully synthesized. The latter method can bring functionality to both organic and inorganic components of the MOF. As outlined in a review article by S. M. Cohen *et al.*, covalent modifications involve changes in the organic linker whereas covalent coordinate modifications deal with changes in the coordination environment of the metal centers, and thus the SBU.[27] Both PSM methods should not alter the overall framework topology.

With the goal of synthesizing MOFs that display porosity, a common practice to achieve large surface areas and pore openings is the use of linearly extending organic linkers. However, it is important to mention that the incorporation of long linkers has a strong tendency to cause framework interpenetration. MOF interpenetration refers to the entanglement of two networks without chemical bonds, yet requires the breaking of bonds in order to be separated. While interpenetration is generally undesired, since it reduces porosity and available pore space, it can provide some advantages such as promoting favorable guest-host interactions. One of the two MOFs presented in this work displays a doubly-interpenetrated framework that maintains high porosity despite interpenetration.

Another exceptional feature of MOFs, differentiating them from other porous media, is their flexibility. Normally, crystalline solids are quite rigid; however MOFs have been known to display reversible swelling under external stimuli such as pressure, temperature, light and gas/solvent adsorption. Critical in the observation of this swelling behavior is the retention of the integrity of the MOF framework. Indeed, the structural characterization of breathable MOFs remains a significant challenge due to the frequent breaking down of crystals into powders following the solid-phase transformation. X-ray crystallography is the only current tool capable of unequivocally characterizing the swelling behavior. The contraction and expansion of a host framework will be investigated in the work presented herein, induced by a change in the guest molecules. This work will illustrate, through single-crystal to single-crystal transformations, how the flexibility of inorganic-organic hybrid materials can be influenced by changing the nature of the host-guest interactions.

1.5 The Crystalline Sponge Method and Single-Crystal to Single-Crystal Transformations

The study of MOFs which display porosity inherently concerns the interactions between the host and guests regardless of the potential application. The guests play a major role in the overall physicochemical properties exhibited by the MOF, and therefore, obtaining an in-depth understanding of the identity of the guest molecules and their preferred locations and orientations is a vital component towards the rational improvement of MOF systems. As briefly aforementioned, this structural information can be exceedingly difficult to obtain due to the challenges in maintaining adequate crystallinity for X-ray diffraction studies. While nuclear magnetic resonance, infrared and mass spectrometry are indispensible tools for chemists, they do not provide the same level molecular structural analysis that can be provided through X-ray techniques. The limitation for using single-crystal X-ray diffraction is that the desired molecule must be obtainable as single-crystals. A revolutionary method, published in *Nature*, describes a protocol to obtain crystal structures of target molecules which does not require crystallization of the sample.[28] The synthetic strategy relies on the use of MOFs with molecular cages that would trap specific guest molecules. The porous coordination networks that exhibit high molecular-recognition are termed “crystalline sponges”. These crystalline sponges uptake target guest molecules which become regularly ordered within the MOF structure. Thus, the molecular structure of the guests can be elucidated alongside the host framework. This method is particularly attractive for a number of reasons. First, Fujita and co-workers have demonstrated that only trace amounts of the guest compound (on the nanogram scale) are required for the technique to be successfully carried out.[28] Accordingly, this is a viable technique for guest molecules that are in short supply or difficult to produce. Secondly, the crystalline sponge method allows crystal-free crystallography. In order words, the target molecule does not have to be crystallized or even a solid, in order to obtain its molecular structure. This presents a significant advancement in X-ray crystallography, where compounds that have been previously impossible to crystallize, can now potentially be fully characterized using single-crystal X-ray diffraction. The general procedure for the crystalline sponge is outlined in Figure 5. A single crystal of the molecular sponge, or MOF, is treated with a drop of the liquid guest. Once the guest has been incorporated into the MOF, the single crystal can then be subjected to single-crystal X-ray diffraction to afford the host with the new guest.

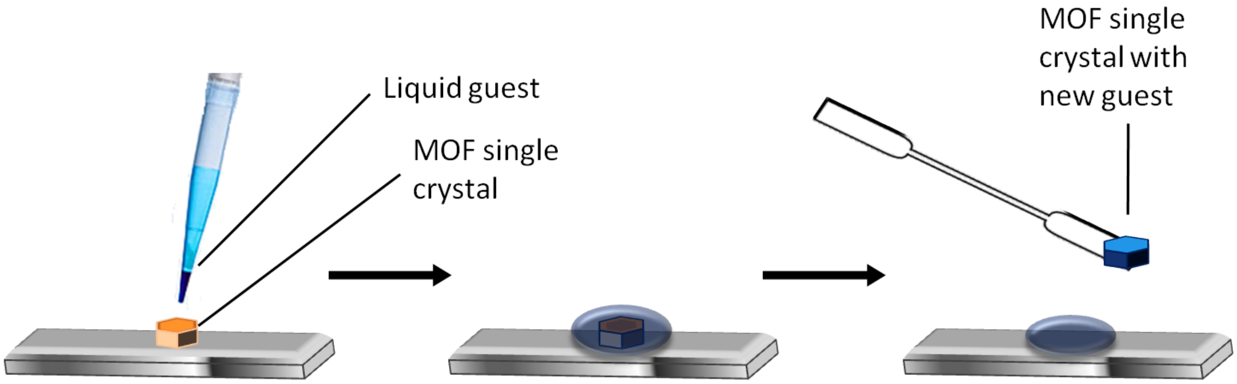

Figure 5: Schematic representation of the crystalline sponge method, where a MOF single-crystal is treated with a drop of liquid guest and subsequently analyzed by X-ray diffraction. This figure is inspired by Fujita *et al.* (2013).[27]

It is noteworthy that molecular sponges are not an entirely novel idea. In 1993, Byrn *et al.* co-crystallized a large number of guest molecules within porphyrin networks,[29] however, the recent work by Fujita and co-workers has reignited the field of molecular sponges and attracted much attention in the scientific community. Since then, a small number of papers have reported employing these molecular sponges to accommodate guest compounds. For example, Buchwald and co-workers have elucidated the structure of a thioperoxide that transfers trifluoromethyl-sulfur groups to carbon atoms.[30] Crystallization of the thioperoxide was a significant challenge since it remains a liquid down to very low temperatures, and hence, the crystalline sponge method offered a solution to this structural problem. Fujita has also studied the mechanism of Pd-catalyzed aromatic bromination reaction by encapsulating the substrate within the pores.

While studies that employ the crystalline sponge method are relatively scarce, the method promises a number of new applications in the near-future, as demonstrated by the work herein.

The biggest challenge in employing the crystalline sponge method is obtaining adequate crystal data, and is the contributing factor to the small number of publications pertaining to this revolutionary method. Indeed, since the initial report by Fujita and co-workers, which attempted to demonstrate the utility of this practice towards an absolute structural determination, a number of inconsistencies and difficulties were identified. Namely, the identification of miyakosyne A, a chemical made in very small quantities by a marine sponge has been challenging to characterize due to its extreme scarcity. Fujita's method, which relies on X-ray crystallography, provided the best chance for determining the configuration of the third and last unresolved chiral center. While the *Nature* publication alluded to an *S* configuration,[28] difficulties in data quality led to a correction of the original report explaining the incorrect stereochemical determination of the marine natural product. Consequently, maintaining the integrity of the MOF single-crystals are absolutely vital to the method and must be carefully handled throughout the entire process. Along the same lines, selection of suitable high-quality single-crystals for the crystalline sponge method is of utmost importance. An in-depth protocol describing the crystalline sponge method was recently published by the Fujita group in order to help researchers have a higher success rate with the method.[31] Notably, the selection of smaller crystals rather than large single-crystals may help the identification of the guest, which is counterintuitive from a crystallographic point of view. Smaller crystals potentially allow for a higher concentration of guest molecules within the framework aiding the structural refinement process. Other parameters to improve the quality of the data include lowering the X-ray measurement temperature below 80 ^{o}C and optimizing the conditions of the soaking for the desired guest. It is also important to note that the molecular sponges themselves carry some limitations. The pore size dimensions and the lack of favorable interactions may limit the guest's ability to enter the MOF. Additionally, harsh chemicals such as acids or amines may decompose the MOF itself. Therefore, the development of new MOFs to accommodate a wider range of guest molecules, including proteins, can be envisioned. Nevertheless, this thesis will focus on the stability and the guest encapsulation behavior of well-investigated porous MOFs.

1.6 References

[1] Rouquerol, J.; Avnir, D.; Fairbridge, C. W.; Everett, D. H.; Hayes, J. H.; Pernicone, N.; Ramsay, J. D. F.; Sing, K. S. W.; Unger, K. K. *Pure and Appl. Chem.* **1994**, *66*, 1739.

[2] Ahuja, G.; Pathak, K. *Indian J. Pharm. Sci.* **2009**, *71*, 599.

[3] Liu, P. S.; Chen, G. F. *Porous Materials: Elsevier* **2014**, 1, ISBN: 978-0-12-407788-1.

[4] (a) Eddaoudi, M.; Kim, J.; Rosi, N.; Vodak, D.; Wachter, J.; O'Keefe, M.; Yaghi, O. M. *Science* **2002**, *295*, 469. (b) Yuan, P.; Southon, P.D.; Liu, Z.; Green, M. E. R.; Hook, J. M.; Antill, S. J.; Kepert, C. J. *J. Phys. Chem. C*, **2008**, *112*, 15742. (c) Stein, A.; Wang, Z.; Fierke, M. A. *Adv. Mater.* **2009**, *21*, 265. (d) Uemera, T.; Yanai, N.; Kitagawa, S. *Chem. Soc. Rev.* **2009**, *38*, 1228.

[5] Cronstedt, A. F. Ron och beskriting om en obekant barg ant, som kallas zeolites. *Akad. Handl. Stockholm* **1756**, *18*, 120.

[6] Flanigen, E. M.; Broach, R. W.; Wilson, S. T. *Zeolites in Industrial Separation and Catalysis* **2010**, Wiley-VCH Verlag GmbH & Co. KGaA, Weinheim, Germany. DOI: 10.1002/9783527629565.ch1.

[7] International Zeolite Association, Database of Zeolite Structures, http://www.iza-structure.org/databases/, accessed July 14 2015.

[8] Deville, H. de St Claire *Comptes Rendus Acad. Sci.* **1862**, *52*, 324.

[9] Catlow, C. R. A.; George, A. R.; Freeman, C. M. *Chem. Commun.* **1996**, 1311.

[10] Averill, B.; Eldredge, P. *General Chemistry: Principles, Patterns, and Applications* **2011**, ISBN: 978-0805337990

[11] Schoonheydt, R. A.; Geerlings, P.; Pidko, E. A.; van Santen, R. A. *J. Mater. Chem.* **2012**, *22*, 18705.

[12] Townsend, R. P.; Coker, E. N. *Stud. Surf. Sci. Catal.* **2001**, *137*, 467.

[13] (a) Blanchard, G.; Maunaye, M.; Martin, G. *Water Research* **1984**, *18*, 1501. (b) Borai, E. H.; Harjula, R.; Malinen, L.; Paajanen, A. *J. Hazard. Mater.* **2010**, *182*, 225.

[14] Biswas, J.; Maxwell, I. E. *Appl. Cat.* **1990**, *63*, 197.

[15] Cote, A.; Benin, A.; Ockwig, N.; O'Keefe, M.; Matzger, A.; Yaghi, O. M. *Science* **2005**, *310*, 1166.

[16] (a) Davankov, V. A.; Rogozhin, S. V.; Tsyurupa, M. P. USSR Inventor's Certificate no. 299165, 19969; US Patent 3729457, **1971**. (b) Xu, S.; Luo, Y.; Tan, B. *Macromol. Rapid Commun.* **2013**, *34*, 471.

[17] (a) Uribe-Romo, F; Doonan, C.; Furukawa, H.; Oisaki, K.; Yaghi, O. M. *J. Am Chem. Soc.* **2011**, *133*, 11478. (b) Kandambeth, S.; Mallick, A.; Lukose, B.; Mane, M.; Heine, T.; Banerjee, R. *J. Am. Chem. Soc.* **2012**, *134*, 19524. (c) Beaudoin, D.; Maris, T.; Wuest, J. D. *Nat. Chem.* **2013**, *5*, 830.

[18] (a) Kuhn, P.; Antonietti, M.; Thomas, A. *Angew. Chem. Int. Ed.* **2008**, *47*, 3450. (b) Bunck, D. N.; Dichtel, W. R. *Angew. Chem. Int. Ed.* **2012**, *51*, 1885.

[19] Bunz, U. H. F. *Chem. Rev.* **2000**, *100*, 1605.

[20] (a) El-Kaderi, H. M.; Hunt, J. R.; Mendoza-Cortés, J. L.; Côté, A. P.; Taylor, R. E.; O'Keeffe, M.; Yaghi, O. M. *Science* **2007**, *316*, 268. (b) Côté, A. P.; El-Kaderi, H. M.; Furukawa, H.; Hunt, J. R.; Yaghi, O. M.; *J. Am. Chem. Soc.* **2007**, *129*, 12914.

[21] Beaudoin, D.; Maris, T.; Wuest, J. D. *Nat. Chem.* **2013**, *5*, 830.

[22] Nietzki, R.; Kehrmann, F. *Chem. Ber.* **1887**, *20*, 613.

[23] Britt, D.; Furukawa, H.; Wang, B.; Glover, T. G.; Yaghi, O. M. *PNAS* **2009**, *106*, 20637.

[24] Hoskins, B. F.; Robsen, R. *J. Am. Chem. Soc.* **1989**, *111*, 5962.

[25] Batten, S. R.; Champness, N. R.; Chen, X.-M.; Garcia-Martinez, J.; Kitagawa, S.; Öhrström, L.; O'Keeffe, M.; Suh, M. P.; Reedijk, J. *Pure Appl. Chem.* **2013**, *85*, 1715.

[26] (a) Eddaoudi, M.; Moler, D. B.; Li, H.; Chen, B.; Reineke, T. M.; O'Keeffe, M.; Yaghi, O. M. *Acc. Chem. Res.* **2001**, *34*, 319. (b) Farha, O. K.; Eryazici, I.; Jeong, N. C.; Hauser, B. G.; Wilmer, C. E.; Sarjeant, A. A.; Snurr, R. Q.; Nguyen, S. T.; Yazaydin, A. O.; Hupp, J. T. *J. Am. Chem. Soc.* **2012**, *134*, 15016.

[27] Tanabe, K. K.; Cohen, S. M. *Chem. Soc. Rev.* **2011**, *40*, 498.

[28] Inokuma, Y.; Yoshiokia, S.; Ariyoshi, J.; Arai, T.; Hitora, Y.; Takada, K.; Matsunaga, S.; Rissanen, K.; Fujita, M. *Nature* **2013**, *495*, 461.

[29] Byrn, M. P.; Curtis, C. J.; Hsiou, Y.; Khan, S. I.; Sawin, P. A.; Tendick, S. K.; Terzis, A.; Strouse, C. E. *J. Am. Chem. Soc* **1993**, *115*, 9480.

[30] Vinogradova, E. V.; Müller, P.; Buchwald, S. L. *Angew. Chem. Int. Ed.* **2013**, *53*, 3125.

[31] Inokuma, Y.; Yoshioka, S.; Ariyoshi, J.; Arai, T.; Fujita, M. *Nat. Protoc.* **2014**, *9*, 246.

Chapter 2

The Hidden Transformations of a Molecular Sponge

Abstract

Our investigations on the stability of a well-known three-dimensional molecular sponge $\{[(\mathrm{Co(NCS)_2})_3(\mathrm{TPT})_4]\cdot x(\mathrm{H_2O})\cdot y(\mathrm{MeOH})\}_n$ (**1b**), constructed from $\mathrm{Co(NCS)_2}$ and the branching 2,4,6-tris(4-pyridyl)-1,3,5-triazine (TPT) ligand, is presented. When the crystalline material is removed from solution, a remarkable color change from orange to green is observed, corresponding to the formation of a semi-amorphous material $\{[(\mathrm{Co(NCS)}_{\alpha})_3(\mathrm{TPT})_{\beta}](\mathrm{NCS})_{2-\alpha}(\mathrm{TPT})_{4-\beta}\cdot a(\mathrm{H_2O})\}_n$ (**2**), where $\alpha = 1$ or 2 and $\beta = 2$ or 3, elicited by a solid-state to solid-state transformation. Diffuse reflectance spectroscopy studies were carried out to examine this transformation, indicating a change in the coordination environment of the $\mathrm{Co^{II}}$ metal centers from octahedral to tetrahedral. Another transformation, resulting from an increase in the $\mathrm{Co(NCS)_2}$ concentration from evaporation of the methanol layer, leads to a structural rearrangement, giving a two-dimensional sheet network$\{[(\mathrm{Co(NCS)_2(H_2O)_{0.65}(MeOH)_{0.35}})_3(\mathrm{TPT})_2]\cdot 2.4(\mathrm{H_2O})\}_n$ (**3**). Direct current (dc) magnetic susceptibility measurements in the temperature range of 1.8–300 K reveal significant magnetic anisotropy for all compounds. Furthermore slow relaxation of the magnetization can also be observed for **2** and **3**, however, only **1b** clearly exhibits Single-Molecule Magnet (SMM)-like behavior under an applied dc field of 600 Oe, giving an anisotropic barrier $U_{\mathrm{eff}} = 7.0$ K.

2.1 Introduction

For decades porous materials have been used to trap and store guest substrates with a wide range of potential applications; however, naturally occurring porous materials, such as clays and zeolites, exhibit a variety of pores sizes in the same sample allowing a lesser degree of control and selectivity for desired guest molecules. Researchers have been interested in the smart design of uniform porous materials by controlling the size of the pores and anticipating the resulting host-guest interactions.[1] While metal-organic materials have existed for some time, it was not until the 1990's that such structures captured the attention of the scientific community through the elegant work of Yaghi and others.[2] Following evidence that metal-organic materials could exhibit permanent porosity, the term Metal-Organic Framework, abbreviated to MOF, was introduced.[3] Since then, development of MOFs and other nanoporous materials are of great interest for the adsorption and storage of guest molecules.[4] The most commonly explored guest substrates are gases, among which adsorption of H_2 and CO_2 are the most attractive applications at the present time.[5]

MOFs can be considered as three-dimensional (3D) hybrid materials that are constructed, most commonly, from inorganic nodes and rigid organic linkers, thus providing the necessary robustness to prevent the pores from collapse since "*nature abhors a vacuum*". In particular, the trigonal 3-connector 2,4,6-tris(4-pyridyl)-1,3,5-triazine (TPT) ligand (Scheme 3) has afforded a large number of stable and highly symmetrical MOFs.[6] Smart control of the nature of both inorganic and organic parts of MOFs allows the design of frameworks with targeted molecular recognition due to specific guest-host interactions.[7] This strategy was further investigated by Fujita and co-workers for the utilization of MOFs as molecular cages for the soaking of different substrates from solutions.[8] This elegant work was centered around the fact that these MOFs can be used as "molecular sponges" for performing single-crystal X-ray diffraction (SCXRD) of guest molecules after soaking.[9] This technique, in some way, revolutionizes SCXRD, by enabling structure determination for molecules that are not possible to crystallize and, in recent years has been successfully employed by others.[10]

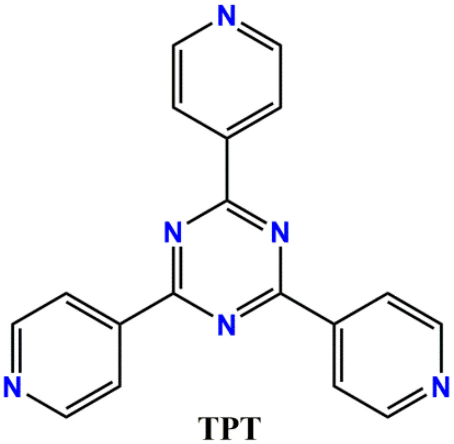

TPT

Scheme 3. 2,4,6-tris(4-pyridyl)-1,3,5-triazine (TPT) ligand.

Two molecular sponges have been reported by the Fujita group, one of which is a cobalt-based three-dimensional MOF, while the other is a doubly-interpenetrated Zn-based MOF. Inspired by these outstanding findings, we decided to apply the crystalline sponge method using the MOF constructed from $Co(NCS)_2$ and TPT for the soaking of magnetic molecules;[11] compounds we have extensively studied so far.[12] As will be described later on, the Co-based molecular sponge contains three different molecular cages of different pore sizes permitting the accommodation of a large number of guest compounds. Furthermore, the available pore space is expected to be large than that of the Zn-based molecular sponge. For this reason, the accommodation of single-ion magnets or mononuclear single molecule magnets inside the pores of the Co-based MOF would be more plausible. The synthetic strategy consisted of understanding the interactions between the paramagnetic cobalt host and the magnetic guests, in order to directly investigate the effect of the host on the overall magnetic properties. Thus, SCXRD on the inclusion compound would permit direct magneto-structural correlations. Up until very recently, the incorporation of SMM's into MOFs has never been achieved before. In July 2015 however, M. Wriedt and co-workers have demonstrated the insertion of the prototypical $[Mn_{12}O_{12}(O_2CCH_3)_{16}(OH_2)_4]$ SMM cluster into a mesoporous MOF.[13] Encouraging this approach was the report by Fujita *et al.* on the incorporation of fullerene guests. Notably, C_{60} and C_{70} were shown to be encapsulated in the void spaces of Co-based MOF through a significant color change in the single-crystals from orange to black. Moreoever, the MOF displayed selectively towards the two fullerenes, where the C_{70} guests were preferentially extracted from a 1:1 mixture of C_{60} and C_{70}.[11] These results strongly suggested the suitability of the MOF for larger guest compounds, which required for the soaking of magnetic molecules of interest.

During our numerous attempts to prepare the parent MOF however, we were faced with intriguing and striking results, probably influenced by the observed instability of the reported Co-based molecular sponge. In order to exploit the full potential of the MOF, it is critical to have an in-depth understanding of the stability and physical properties of the molecular sponge. With this in mind, the present chapter focuses on new insights and a detailed investigation of the previously described MOF, named by the authors as $\{\{[(Co(NCS)_2)_3(TPT)_4]\cdot 25(o\text{-dichlorobenzene})\cdot 5(MeOH)\}_n$ (**1a**).[11] This emerging MOF also exhibits potential in becoming a multifunctional material by combining its well-studied porosity with magnetism, a rather scarce feature in inorganic porous solids. Among the limited number of magnetic MOFs displaying slow relaxation of the magnetization, cobalt is an attractive 3d element due to its highly anisotropic nature and ability to bind in a variety of coordination modes.[14] Consequently, we have set out to investigate the magnetic behavior of the compounds presented herein. We also provide new insights on the established structure and composition of **1a**.

2.2 Experimental section

2.2.1 General considerations

All manipulations, unless otherwise stated, were performed under aerobic/ambient conditions. All materials were used as received from TCI, Strem Chemicals and Sigma Aldrich without further purification.

2.2.2 Synthesis

The 2,4,6-tris(4-pyridyl)-1,3,5-triazine (TPT) ligand[15] and the parent Co-based molecular sponge, $\{[(Co(NCS)_2)_3(TPT)_4]\cdot x(H_2O)\cdot y(MeOH)\}_n$ (**1b**),[11] were synthesized according to previously reported methods. The synthesis of TPT involves dissolving 18-crown-6 (1.0 g, 3.8 mmol) and KOH (0.225 g, 4.0 mmol) in 10 mL of ethanol and stirring for 10 mins. The solution is then concentrated under reduced pressure to give a pale yellow oil product. To this oil, 10 g of 4-cyanopyridine was added and heated to 220 ^{o}C. The color of the mixture changed to red within a short period of time. After stirring at this temperature for 4 h, the mixture was cooled to room temperature and 30 mL of pyridine was added. Stirring this mixture for several minutes gave a reddish crystalline compound that was filtered and washed with pyridine (twice with 25 mL) and toluene (25 mL). The red product was dissolved in 60 mL of 2M HCl. After removing any solid residue by filtration, the solution was adjusted to slightly basic using concentration aqueous NH_3 and pH paper. The resulting white powder was filtered, washed with water and dried in air to afford TPT in ~60% yield. NMR ^{1}H ($CDCl_3$, 400 MHz): δ 8.63 (d, 6H), 8.93 (d, 6H). Selected IR (cm^{-1}): 3063 (w), 1574 (m), 1512 (s), 1449 (w), 1416 (w), 1371 (s), 1318 (m), 1304 (m), 1225 (w), 1158 (w), 1061 (m), 1052 (m), 992 (w), 886 (w), 793 (s), 666 (m), 640 (s).

Compound **1b** was obtained by dissolving TPT (6.3 mg, 20 μmol) in 4.0 mL of *o*-dichlorobenzene and 1.0 mL of methanol in a test tube (diameter 1 cm and height of 10 cm) through sonication. A methanol solution of $Co(NCS)_2$ (40mM, 1.0 mL) was layered carefully on top of the TPT solution using a 1.0 mL syringe. The resulting solution was allowed to stand for one week at room temperature, resulting in block-like orange single-crystals (yield 44 %) and pale pink powder (yield 12 %). An in-depth analysis of the IR and diffuse reflectance spectroscopy will be presented later on (*vide infra*).

The removal of single crystals of **1b** (orange block crystals) from the mother liquor, and exposing them to aerobic or inert atmospheres, led to the formation of a dark green semi-amorphous material, $\{[(Co(NCS)_{\alpha})_3(TPT)_{\beta}](NCS)_{2-\alpha}(TPT)_{4-\beta}\cdot a(H_2O)\}_n$ (**2**). Moreover, extensive evaporation of the methanol layer over a period of one week during the synthesis of **1b** led to a change in color of a few crystals from orange to pink resulting in the formation of $\{[(Co(NCS)_2(H_2O)_{0.65}(MeOH)_{0.35})_3(TPT)_2]\cdot 2.4(H_2O)\}_n$ (**3**) and a large amount of microcrystalline pale pink powder, which was also identified as **3**. The use of chlorobenzene instead of *o*-dichlorobenzene during the synthesis of **1b** leads to the formation of pale pink powder **3** as a major product and very few crystals of **1b** (Figure 6).

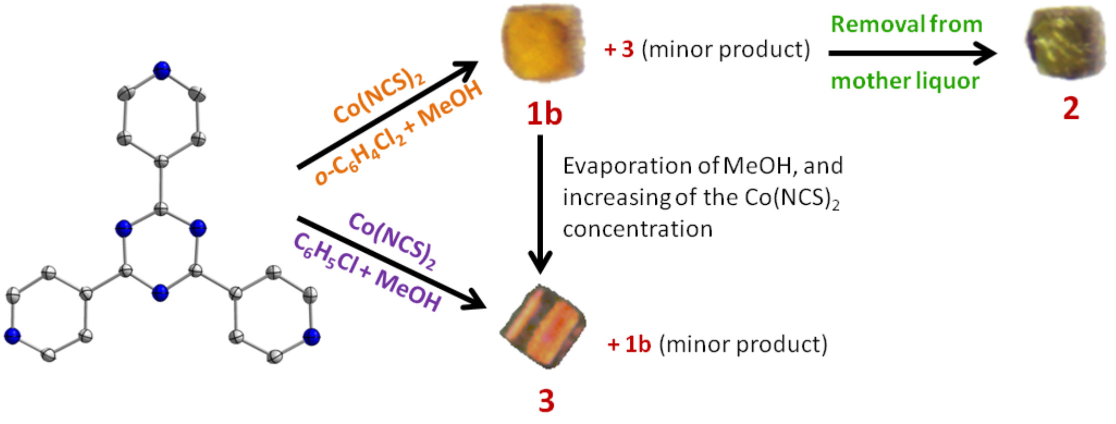

Figure 6: Picture of single crystals of **1b-3** and their corresponding transformations viewed under optical microscope at room temperature.

2.2.3 Physical measurements

Infrared spectra were recorded with a Varian 640 FTIR spectrometer equipped with an ATR in the 500–4000 cm^{-1} range. Diffuse reflectance spectra were measured with a Varian

Cary-100 spectrophotometer using polytetrafluoroethylene (PTFE) as a reference. Kubelka-Munk spectra were normalized to allow for meaningful comparisons. Thermogravimetric analysis (TGA) data were recorded using a Q5000 IR TGA instrument at a heating rate of 5 ^{o}C/min between room temperature and 800 ^{o}C, under a constant flow of air or nitrogen (25 mL/min). Powder X-ray diffraction (PXRD) for bulk samples were carried out using a Rigaku Ultima IV X-ray powder diffractometer. The parallel beam mode was employed to collect the data (λ = 1.541836 Å). NMR analyses were conducted using a Bruker Avance 400 MHz spectrometer equipped with an automatic sample charger and a 5 mm auto-tuning broadband probe with Z gradient.

2.2.4 Single Crystal X-ray Diffraction Studies

Data collection results for **1b** and **3**, represent the best data sets obtained in several trials for each sample. Prior to data collection, crystals of **1b** were preserved in the mother liquor and subsequently mounted on thin glass fibers using paraffin oil. For **1b**, the crystals were preserved in the mother liquor prior to data collection and then cooled to 200 K. Data set for the crystal of 3 was collected at room temperature using colorless nail polish to attach the crystal to the thin glass fiber pin. Data was collected on a Bruker AXS KAPPA single crystal diffractometer equipped with a sealed Mo tube source (wavelength 0.71073 Å) APEX II CCD detector. Raw data collection and processing were performed with APEX II software package from Bruker AXS.[16] Diffraction data for both samples were collected with a sequence of 0.3° ω scans at 0, 90, 180 and 270° in φ to provide the acceptable redundancy of data. Initial unit cell parameters were determined from 60 data frames with 0.3° ω scan each collected at the different sections of the Ewald sphere. Semi-empirical absorption corrections based on equivalent reflections were applied.[17] Systematic absences in the diffraction data-set and unit-cell parameters were consistent with trigonal *R*–3*m* (№ 166) space group for **1b** and trigonal *R*–3 (№ 148) space group for **3**.

Solutions in the centrosymmetric space groups for both compounds yielded chemically reasonable and computationally stable results of refinement. The structures were solved by direct methods, completed with difference Fourier synthesis, and refined with full-matrix least-squares procedures based on F^2.

Diffraction data for **1b** was collected to 0.75 Å resolution, however, due to small crystal size and weak diffraction, it was discovered that both $R_{(\mathrm{int})}$ and $R(\sigma)$ exceed 35% for the data below 1.10 Å resolution. Therefore, the data was truncated to 1.05 Å resolution for refinement, based on the $R(\sigma)$ value. The asymmetric unit for this crystallographic model of **1b** contains two cobalt metal centers located on inversion centers as well as two fragments of the ligand with one full ligand located on a 3-fold axis while the second one occupies another inversion center of the space group. When the anisotropic atomic model was applied on the final stages of refinement, thermal motion parameters for the one of the pyridine rings based at C5 and N3 suggested a rotational disorder not related to the symmetry elements. Disorder was successfully modeled, however the set of thermal motion (SIMU, DELU) restrains were applied to achieve acceptable fragment geometries and thermal motion values. Disordered fragment occupancies were refined with satisfactory results at 50% : 50%. After successfully modeling the core of the MOF with full anisotropic refinement, several randomly scattered residual electron density peaks were discovered in the void space of the structure. The most prominent peak had an intensity of 1.67 electrons. Only eight strongest peaks exceeded the value of one electron, averaging at 1.27 electrons per peak. To conserve acceptable data to parameters ratio while improving core model refinement results, the original reflection file for **1b** was treated with the SQUEEZE routine of PLATON[18] giving a refined void space per cell equal to 30334.2 Å^3 and an electron count of 8423 per cell. Final model refinement was performed against SQUEEZE alternated reflection file.

Diffraction data for the crystal of complex **3** were collected to 0.75Å. The structural model for this compound reveals an asymmetric unit containing one cobalt metal center located on an inversion center and a full TPT ligand located on the 3-fold axis of the space group. After anisotropic refinement of the core model, the presence of several rather strong electron density peaks near cobalt metal centers suggested the presence of an additional moiety coordinated to the metal. After careful consideration of all the possibilities, these electron density peaks were interpreted as an occupational disorder between coordinated water and methanol molecules. Initially, occupancies for both molecules were free to refine, however, both occupancies were constrained to refined values of 65% : 35% for water and methanol, respectively. Thermal parameters for both fragments were set free for refinement, however, to provide acceptable values, additional thermal constrains (EADP) were employed. In addition to the disordered water molecule coordinated to the metal center, residual electron density suggested the presence of another partially occupied water molecule coordinated to the first one through a hydrogen bond. Similar treatment with occupancy refinement produced 35% occupational value for the second water molecule. It should be mentioned that even after modeling, the position of the second water molecule, yielded a refinement routine that consistently produced a few randomly scattered residual electron density peaks in the void space of the structure. The most prominent peak had an intensity of 4.05 electrons. Only eight strongest peaks exceeded the value of one electron, averaging 1.94 electrons per peak. To conserve an acceptable data to parameters ratio, while improving core model refinement results, the original reflection file for **3** was treated with the SQUEEZE routine of PLATON[18] with a refined void space per cell equal to 1792.4 Å^3 and an electron count of 555 electrons per cell.

Final model refinement was performed against a SQUEEZE alternated reflection file. For both structural models, all hydrogen atomic positions were calculated based on the geometry of the related non-hydrogen atoms. All hydrogen atoms were treated as idealized contributions during the refinement. All scattering factors are contained in several versions of the SHELXTL program library; with the latest version being v.6.12.[19] Crystallographic data and selected data parameters are reported in Table 1. The crystal structures have been deposited at the Cambridge Crystallographic Data Centre and allocated the deposition numbers CCDC 1008410 (**1b**) and 1008411 (**3**).

Table 1: Summary of the crystal structure data and refinement for compounds **1a**, **1b** and **3**.

Complex	**1a***	**1b**	**3**
Formula	$C_{26}H_{16}N_{10}CoS_2$	$C_{78}H_{48}Co_3N_{30}S_6$	$C_{44.10}H_{45}Co_3N_{18}O_{8.40}S_6$
FW, g mol^{-1}	591.56	1774.61	1330.73
Space group	*Fm*-3*m*	*R*-3*m*	*R*-3
Crystal system	cubic	trigonal	trigonal
T, K	90(2)	200(2)	296(2)
a, Å	37.461(5)	26.7888(6)	26.6894(6)
b, Å	37.461(5)	26.7888(6)	26.6894(6)
c, Å	37.461(5)	65.6133(18)	9.8119(3)
α, ^{o}	90	90	90
β, ^{o}	90	90	90
γ, ^{o}	90	120	120
V, Å^3	52 571(12)	40 778(2)	6052.9(3)
Z	24	6	3
ρ_{calcd}, g cm^{-3}	0.448	0.434	1.095
μ (Mo, Kα), mm^{-1}	0.255	0.246	0.812
reflns collected	1954	5084	3286
$R1$, $wR2$ ($I > 2\sigma(I)$)[a]	0.0998, 0.2830	0.0600, 0.1650	0.0670, 0.1867
$R1$, $wR2$ (all data)	0.1286, 0.2978	0.1259, 0.2095	0.0878, 0.2087

[a] $R = R1 = | |F_o| - |F_c|/|F_o|$; $wR2 = \{[w(F_o - F_c^2)^2] / [w(F_o^2)^2]\}^{1/2}$; $w = 1/[\sigma_2(F_o^2) + (ap)^2 + bp]$, where $p = [\max(F_o^2, 0) + 2 F_c^2]/3$; and $Rw = [w(|F_o| - | F_c|)^2 /w|F_o|^2]^{1/2}$, where $w = 1 / \sigma^2(|F_o|)$. *Values taken from reference [11].

2.2.5 Magnetic measurements

The magnetic susceptibility measurements were obtained using a Quantum Design Superconducting Quantum Interference Device (SQUID) magnetometer MPMS-XL7 that functions between 1.8 and 300 K for direct current (dc) applied fields ranging from -7 to 7 T. Measurements were performed on polycrystalline samples of 14.7, 5.4 and 8.6 mg of complexes **1b**, **2** and **3**, respectively. Compound **1b** was measured in paraffin oil to prevent transformation of **1b** to **2**, while compounds **2** and **3** were wrapped in a polyethylene membrane. Alternating current (ac) susceptibility measurements were performed under an oscillating ac field of 3.78 Oe and ac frequencies that ranged from 0.1 to 1500 Hz. Ferromagnetic impurities that were absent in all samples were investigated by collecting magnetization data at 100 K. All magnetic data were corrected for sample holders as well as other diamagnetic contributions.

2.3 Results and discussion

2.3.1 Synthesis

The rigid 2,4,6-tris(4-pyridyl)-1,3,5-triazine (TPT) ligand has been successfully employed in the construction of numerous MOFs and supramolecular systems.[20] Among these reported materials, the molecular sponge synthesized by Fujita and co-workers, has tremendous potential applications in host-guest chemistry and in modern X-ray crystallography for its ability to refine molecular structures of non-crystallizing systems. Our numerous attempts to obtain the reported compound, **1a**, by carefully reproducing the synthetic procedure failed and continually led to the formation of **1b**.[11] As such, complex **1b** is readily obtained by layering a methanol solution of $Co(NCS)_2$ onto the solution of TPT in a mixture of *o*-dichlorobenzene and methanol. Surprisingly, according to SCXRD, complex **1b** contains molecules of water and/or methanol as lattice solvents (*vide infra*). It is noteworthy that the structure reported by Fujita and co-workers for the synthesis of compound **1a** were replicated for **1b**, however, it was reported that the lattice solvents contained exclusively *o*-dichlorobenzene and methanol.[11] This was not apparent in the reported X-ray structure and the assumption was made primarily using elemental analysis data.

An additional important finding during our manipulations with **1b** involves a progressive and gradual color change from light orange to green which occurs when single crystals of **1b** are removed from solution and kept under aerobic or inert atmospheres, resulting in the formation of the dark green semi-amorphous material $\{[(Co(NCS)_{\alpha})_3(TPT)_{\beta}](NCS)_{2-\alpha}(TPT)_{4-\beta}\cdot a(H_2O)\}_n$ (**2**) (Figure 7 for PXRD). During this process, visible cracking of the crystals, as well as a slight volume contraction, can be observed. To illustrate this transformation, single crystals of **1b** were removed from mother liquor and their time evolution in air at room temperature was followed by optical microscopy, as shown in Figure 8. In addition, the presence of heat, *e.g.* from a light source, accelerates this irreversible conversion. Such a transformation of this molecular sponge has never been reported. This critical irreversible transformation to a semi-amorphous material prevents any further use of this system as a molecular sponge for SCXRD applications due to the loss of crystallinity and structural change. Therefore, in order to maintain the structural integrity of **1b** out of its mother liquor, the compound must be immediately immersed in oil or suitable solvents, such as toluene and *o*-dichlorobenzene, to prevent this degradation.

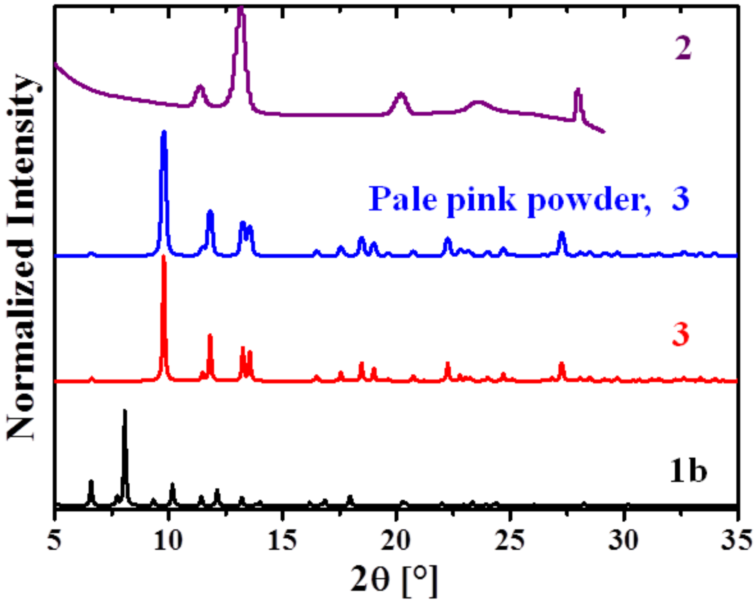

Figure 7: X-ray powder diffraction patterns for the semi-amorphous compound **2** (purple), and microcrystalline pale pink powder, identified as **3** (blue). The simulated diffraction patterns for **1b** (black) and **3** (red) are also displayed.

Furthermore, if **1b** is left in its mother liquor over a period of one week, a change in color of the crystals from orange to pink can be observed along with the formation of microcrystalline pale pink powder. This transformation results in a new compound,

$\{[(Co(NCS)_2(H_2O)_{0.65}(MeOH)_{0.35})_3(TPT)_2]\cdot 2.4(H_2O)\}_n$ (**3**). The co-crystallizing microcrystalline pale pink powder was also identified as **3** (Figure 7). This conversion can be caused by the slow evaporation of the layered methanol resulting in an increase of the $Co(NCS)_2$ concentration. Replacing *o*-dichlorobenzene with chlorobenzene during the synthesis of **1b** leads to the direct formation of **3** in the form of pale pink powder as the major product and few crystals of **1b**. This remarkable difference can be explained by the significantly lower density of chlorobenzene compared to *o*-dichlorobenzene, which in turn supports faster diffusion of the methanol layer of $Co(NCS)_2$ into the solution of TPT. Consequently, an increase of the reaction rate between $Co(NCS)_2$ and TPT would favor the formation of **3**.

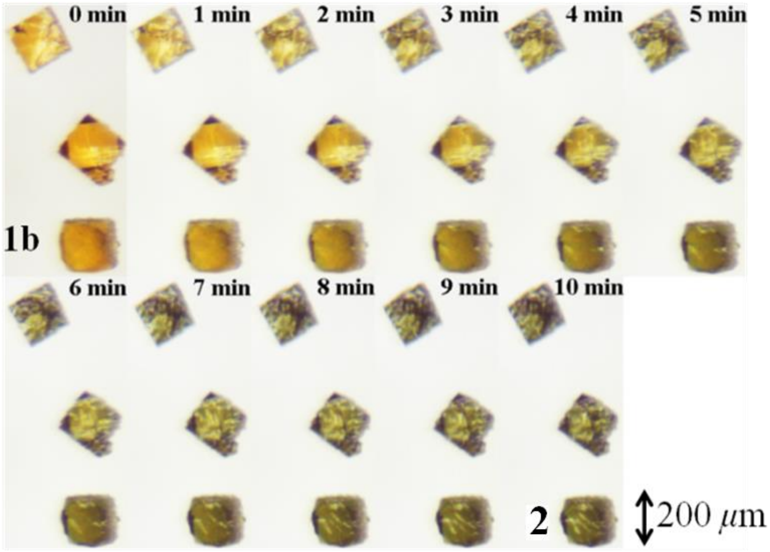

Figure 8: Photos highlighting the gradual transformation of three crystals of **1b** to **2** over time, with varying crystallinities and morphologies, as viewed under optical microscope at room temperature.

2.3.2 Structural analysis

Single crystals of **1b** and **3** suitable for SCXRD analysis were obtained from mother liquors during the synthesis. It should be noted that several different crystals of **1b** and **3** have been checked by SCXRD testifying to their identity. Recently, Fujita and co-workers reported the structure of **1a** to be refined in the cubic space group $Fm–3m$.[11] It is well known that several criteria have to be considered for a correctly refined structure. Among them SHELXL calculates the most important criteria namely R_1 (observed data, $I > 2\sigma(I)$), wR_2 (all data) and the so-called goodness of fit, S. Acceptable values for all these criteria are <7%, <20% and 0.8–1.5, respectively. Careful analysis of the cif file of **1a** shows the following values: R_1 (observed data, $I > 2\sigma(I)$) = 9.98%, wR_2 (all data) = 29.78% and $S = 2.01$. These values strongly suggest the structure was not well refined, and that the reported space group and unit cell parameters may be incorrect. With this in mind, we have focused our attention to find the correct refinement model for **1b**. According to the X-ray data, the structure of **1b** was best refined in the trigonal space group $R–3m$ with the unit cell parameters $a = 26.7888(6)$, $c = 65.6133(18)$ Å and $\gamma = 120°$. The resulting refinement criteria, R_1 (observed data, $I > 2\sigma(I)$) = 6.00%, wR_2(all) = 20.95%, $S = 1.04$, support the suggested model.

Although there is a strong disagreement between the refinement of the X-ray data, in general, the crystal structure of **1b** closely resembles the structure of **1a**. The 3D coordination network reveals an infinite aggregation of three cage-like frameworks, *viz.* octahedral $[Co_6(NCS)_{12}(TPT)_4]$, cuboctahedral $[Co_{12}(NCS)_{24}(TPT)_8]$ and $[Co_{12}(NCS)_{24}(TPT)_{24}]$ polyhedra. The octahedral cage consists of six Co^{II} vertexes and four TPT panels (Figure 9). It is noteworthy that this molecular entity closely resembles that of a discrete cage assembled from six Pd^{II} ions and four TPT ligands.[11] The difference originates from the capping ligands which consist of a bidentate tetramethylenediamine ligand in the Pd^{II} compound while in **1b** the octahedral cage is isolated by terminal thiocyanates. The elegant work of Fujita and co-workers has demonstrated the recognition properties of this octahedral cage for small organic guests such as tetrathiafulvalene (TTF).[11] The guest recognition is promoted by π-stacking and charge transfer interactions between TTF and the ligand of the framework.

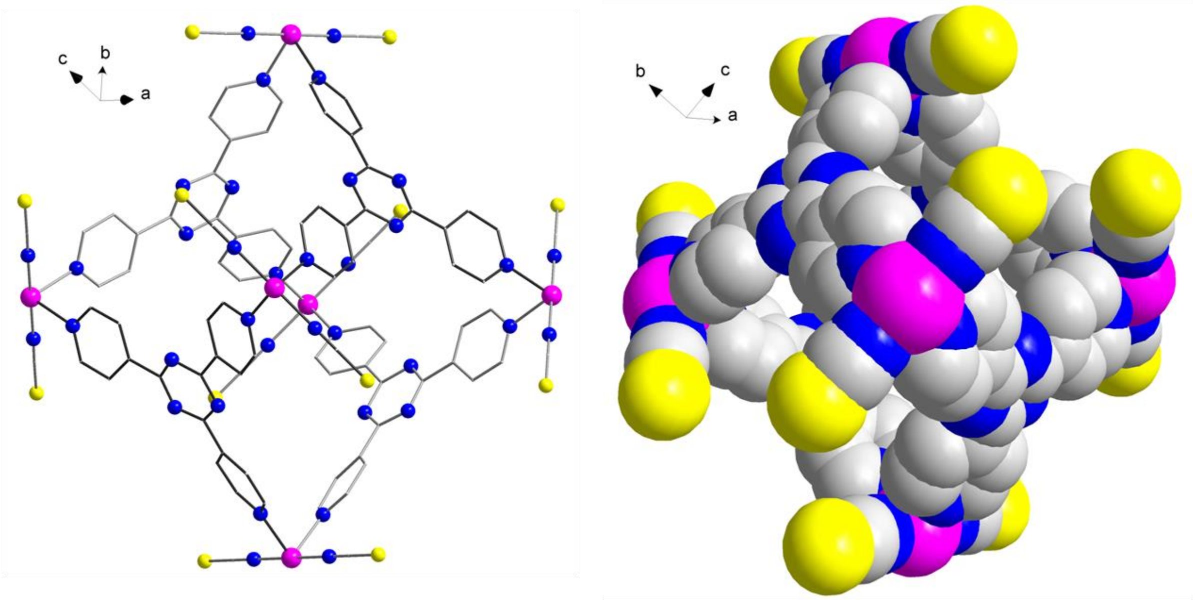

Figure 9: Stick and space-filling model of the $[Co_6(NCS)_{12}(TPT)_4]$ octahedral cage found in **1b** (M_6L_4).

The coordination environment surrounding each cobalt metal center is comprised of four nitrogen atoms originating from the pyridine moieties of the TPT ligand and two terminally bonded thiocyanate groups, effectively forming an octahedral coordination environment (Figure 10).

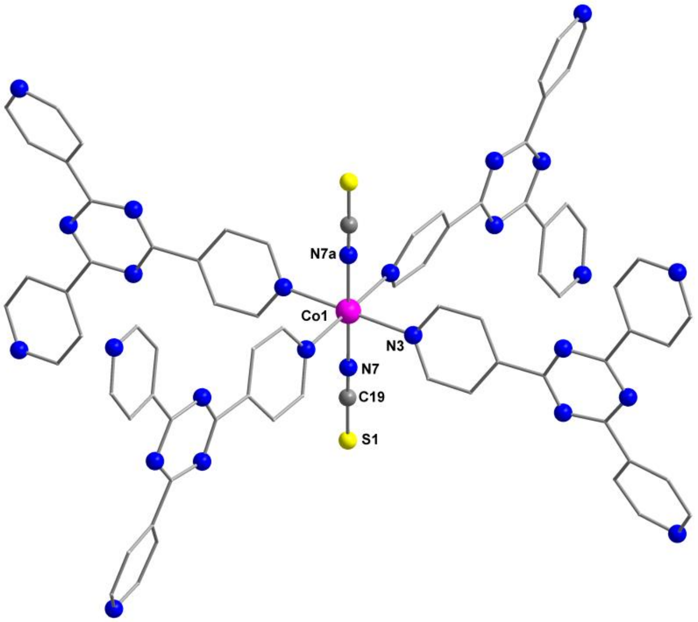

Figure 10: Partially labeled molecular structure of the $[Co(NCS)_2(TPT)_4]$ fragment illustrating the octahedral coordination environment of the cobalt metal centers. Color code: purple (Co), blue (N), gray (C), yellow (S). Hydrogen atoms are omitted for clarity.

It is important to note that there are two crystallographically independent cobalt atoms that display slightly different coordination environments (Figure 11). The Co1 ion displays a 4-fold rotational symmetry axis along the axial positions of the compressed octahedron, while Co2 is in a lower symmetry environment with a slightly distorted octahedral geometry. The NCS^{-} anions were found to be N-bound to Co^{II} in a pronounced linear fashion with the (Co)N–C–S and Co–N–C(S) bond angles being nearly 180°. The Co–N(Py) bond lengths are very similar, with values ranging from 2.17 to 2.21 Å, while the Co–N(thiocyanate) distances are significantly shortened with values of about 2.07 Å (see Table 2 for complete bond distances and angles). The shortest Co···Co distances between adjacent and opposite metal centers in the $[Co_6(NCS)_{12}(TPT)_4]$ polyhedron have been determined to be 13.40 and 18.94 Å. Furthermore, the X-ray analysis revealed that all pyridine rings of the TPT ligand are 50% disordered over two overlapping positions. The volume of the potential void in **1b** was calculated to be 30334.2 Å^3, which is about 74.4% of the unit cell volume. Such large voids in Fujita's work were proven to be critical in encapsulating guest molecules thus making **1b** a desirable molecular sponge.

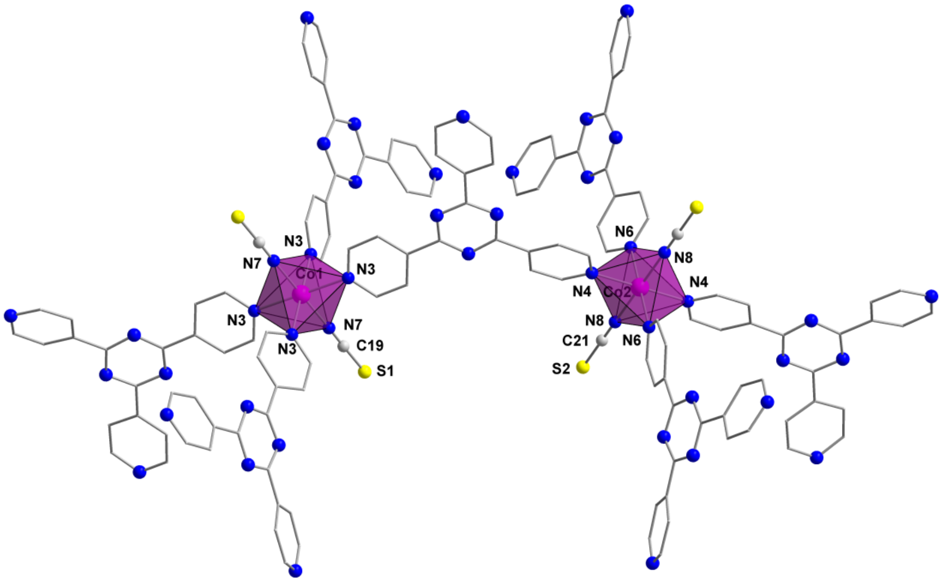

Figure 11: Molecular fragment of **1b**, illustrating the coordination environments of the two crystallographically different cobalt centers. Color code: purple (Co), blue (N), gray (C), yellow (S). Hydrogen atoms are omitted for clarity.

Table 2: Selected bond distances (Å) and angles (°) for **1b**.

Bond distances (Å)					
Co(1)-N(3)	2.21	Co(2)–N(6)	2.21	N(8)–C(21)	1.10
Co(1)–N(7)	2.07	Co(2)–N(8)	2.07	S(1)–C(19)	1.58
Co(2)–N(4)	2.17	N(7)–C(19)	1.11	S(2)–C(21)	1.60
Bond angles (°)					
N(3)–Co(1)–N(7)	90.1	N(6)–Co(2)–N(8)	90.0	S(1)–C(19)–N(7)	178.9
N(4)–Co(2)–N(6)	92.6	Co(1)–N(7)–C(19)	179.1	S(2)–C(21)–N(8)	180.0
N(4)–Co(2)–N(8)	90.0	Co(2)–N(8)–C(21)	180.0		

Further molecular recognition in **1b** can be achieved through the three distinct cage environments found within the frameworks. As previously mentioned, **1b** contains two other polyhedral cages in addition to the octahedral M_6L_4 cage. Indeed, a cuboctahedral cage consisting of twelve Co^{II} ions and eight TPT panels is formed through the interstitial voids (Figure 12). This molecular cage exhibits a pore entrance of approximately 9 x 9 $Å^2$ while the internal area is delineated by two TPT ligands separated by distances of ~20 Å.

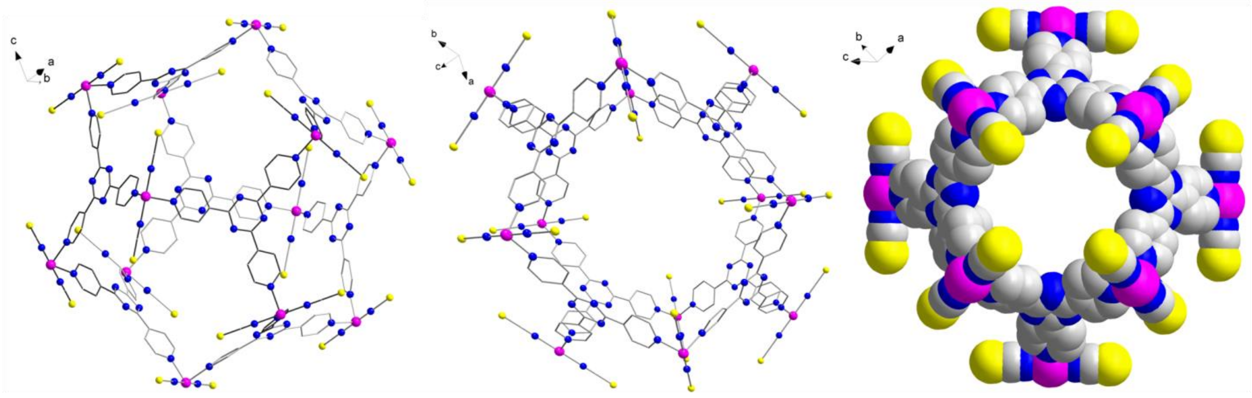

Figure 12: Stick model of the $[Co_{12}(NCS)_{24}(TPT)_8]$ cuboctahedral cage found in **1b** ($M_{12}L_8$) viewed along two different directions. The space filling model is also shown to display the accessibility of the pore for guest molecules.

The final and third molecular cage can be constructed from twelve Co^{II} atoms and twenty-four TPT ligands, forming the largest interstitial space of **1b** (Figure 13). We can envision that guest molecules will exhibit certain selectivity towards the three molecular cages. Indeed, proper shape and sizes of the pores will restrict access to certain guests while others may promote more favorable and stronger interactions leading to higher uptakes. These large $M_{12}L_{24}$ cages have exhibited selectivity towards the incorporation of fullerenes with different sizes. In fact, the preferential extraction of C_{70} from C_{60} in an equal mixture of the two compounds provides great potential for enrichment and isolation applications.[11]

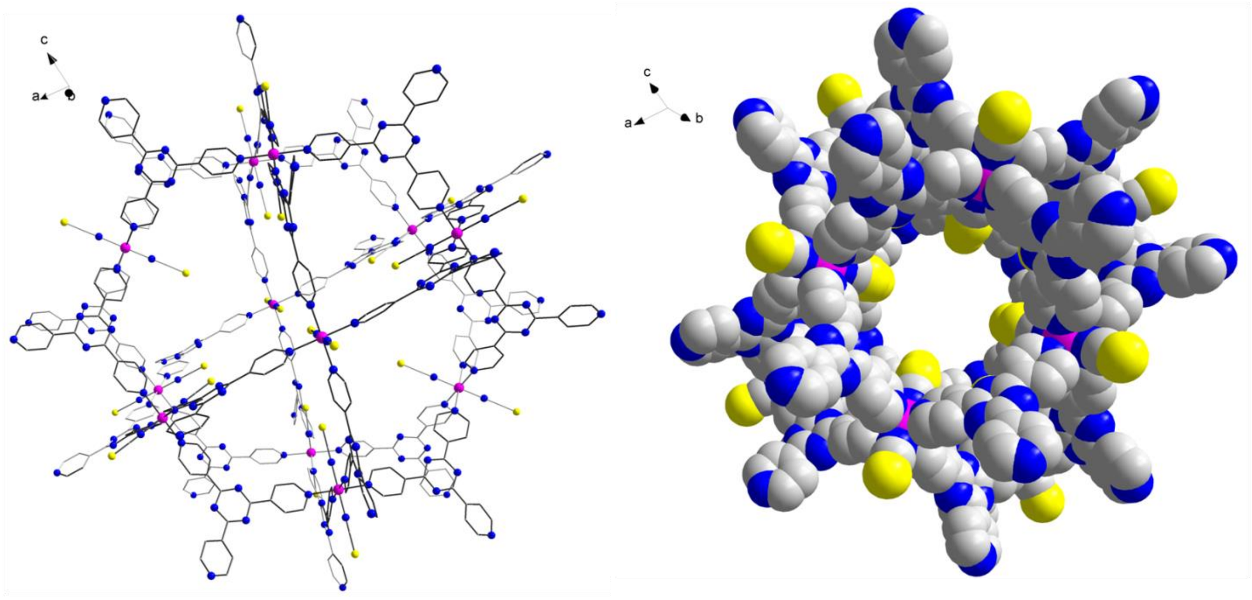

Figure 13: Stick and space-filling model of the $[Co_{12}(NCS)_{24}(TPT)_{24}]$ octahedral cage found in **1b** ($M_{12}L_{24}$).

When considering **1b** as a molecular sponge, which involves the exchange of guest molecules found within the empty space of the MOF, it is critical to have an understanding on the solvents and molecules initially found in the as-synthesized form of the MOF. This will provide valuable insights into the type of interactions between the guest and the host, and whether activation of the MOF is required. Activation refers to the process of evacuating the guest solvent molecules from the pores of the MOF without losing porosity. In our efforts to identify the solvent molecules contained within the pores of **1b**, we were surprised to repeatedly observe the absence of well-defined *o*-dichlorobenzene molecules by SCXRD, as was reported in the structure of **1a** by Fujita and co-workers.[11] After completing a chemically reasonable and computationally stable model for the core of the structure, Fourier maps difference revealed several well defined residual electron density peaks scattered in the void space of the structure. Eight peaks demonstrated intensities over one electron, with the strongest peak displaying an intensity of 1.67 electrons. The average intensity of these 8 strongest peaks was calculated to be 1.27 electrons. The positions of the peaks suggested the presence of partially occupied and possibly disordered solvent molecules. Of all the possible solvent species involved in the synthesis, the most interesting possibility was to confirm the presence of *o*-dichlorobenzene in the cavities of the MOF. In order to evaluate this hypothesis, the strength of the most prominent residual electron density peaks should be evaluated. An intensity of 1.67 electrons for the strongest of the peaks would correspond to the heaviest atom in the solvent molecule, i.e. chlorine. However, even the most intense peak cannot account for the full occupancy of the chlorine atom, making for a maximum possible presence of only 1/10th of the chlorine atom. If 1/10th occupancy for the *o*-dichlorobenzene molecule is assumed, the resulting electron peak intensities for carbon atoms of such a molecule would fall in the range of 0.6 electrons, which is significantly short of the expected value. Considering the quality of the data set, it would be highly speculative to draw conclusions from the positions of the peaks, with such a low overall intensity. Nevertheless, an attempt was made to request the refinement routine for 150 of the strongest residual density peaks in the hope of distinguishing the very characteristic shapes of aromatic rings in close proximity to the strongest electron density areas. It should be noted that no such shapes were found in the voids of the MOF.

On the other hand, it is easy to envision that several strongest residual density maxima with intensities of 1.67 electrons and below can be attributed to the presence of partially occupied molecules of water. In such a case, the intensities would account for water molecules displaying occupancies of 50% or less. It is critical to understand that a definitive conclusion about unit cell formulation cannot be drawn from the results of X-ray analysis alone, and would require additional experimental evidence. Complementary analytical experiments with the bulk of the compound are discussed in the infrared and thermogravimetric analysis sections.

In contrast to the three-dimensional structure of **1b**, the molecular structure of compound **3**, refined in the trigonal space group *R*–3, exhibits tightly packed two-dimensional sheets that are rotated 60° relative to each other. The interlayer distance between two adjacent sheets is approxmiately 3.25 Å. It was found that this interlayer region is partly filled with lattice water molecules and further stabilized by π-π-stacking between the triazine rings of the TPT ligand that are aligned in a parallel fashion, as well as weak interactions between the remaining coordinate ligands. These 2D sheets are constructed from $[Co(NCS)_2(H_2O)_{0.65}(MeOH)_{0.35}]$ fragments linked by the rigid TPT ligands (Figure 14).

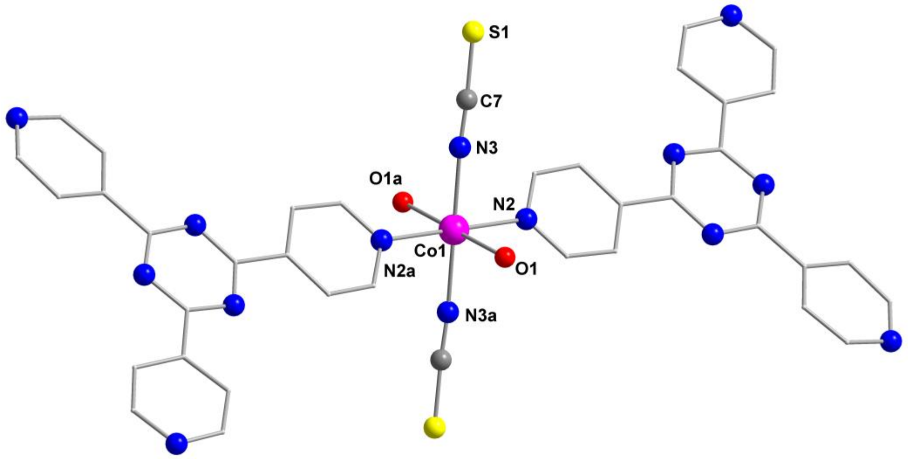

Figure 14: Partially labeled molecular structure of the $[Co(NCS)_2(TPT)_2(H_2O)_2]$ fragment in **3**. Color code: purple (Co), blue (N), gray (C), yellow (S), red (O). Hydrogen atoms, MeOH and lattice H_2O molecules were omitted for clarity.

All Co^{II} atoms are six coordinate and adopt a slightly distorted octahedral geometry formed by two nitrogen atoms of the TPT pyridine groups (N2, N2a), two nitrogen atoms of the NCS^- anions (N3, N3a) and two oxygen atoms of the water and/or methanol molecules (O1, O1a) (Figure 15). The latter solvent molecules exhibit partial occupancies of 65 and 35%, respectively. The primary structural difference between the cobalt centers seen in **1b** and **3** lie in fact that now two TPT nitrogen atoms are replaced by coordinating water and/or methanol solvent molecules. This change in coordination environment is expected to alter the ligand field (*vide infra*).

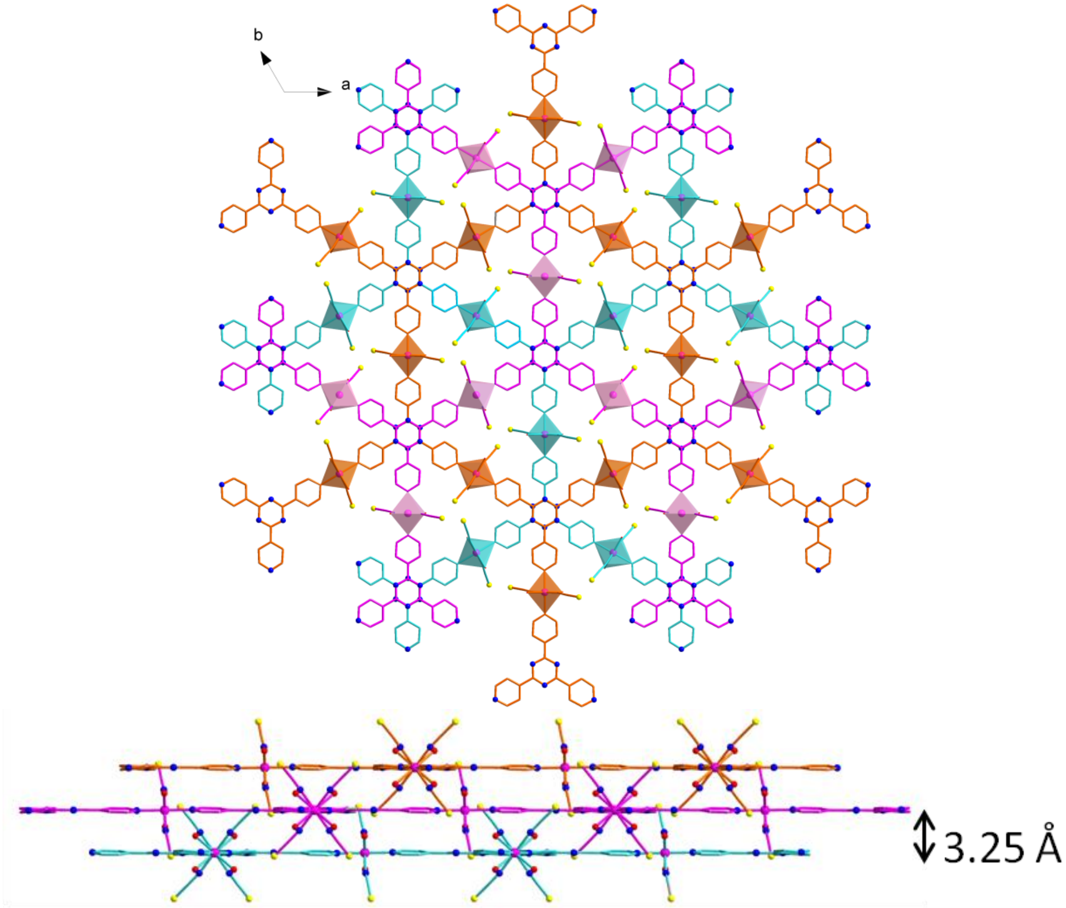

Figure 15: Top: Crystal packing of **3** along the *c*-axis, with the different colors (pink, cyan and orange) corresponding to a different layer. The coordination polyhedra display the location of the cobalt metal centers with respect to their sheet. Bottom: Crystal packing of **3** along the *b*-axis displaying the sheet-like arrangement. Hydrogen atoms, MeOH and lattice H_2O molecules were omitted for clarity.

The NCS^- anions were found to be N-bound to Co^{II} in a slightly bent fashion with the (Co)N–C–S and Co–N–C(S) bond angles being about 178 and 172°, respectively, while the Co–N(Py) and Co–N(thiocyanate) bond lengths have been determined to be 2.15 Å and 2.08 Å, respectively (Table 3). Moreover, the shortest intralayer Co···Co distance is 13.35 Å (occurring through the TPT ligand), while the shortest Co···Co distance occurs between adjacent layers with a distance of 8.37 Å. The potential volume of the void space in **3**, estimated by removing the lattice water molecules, was calculated to be 1792.4 Å^3, which is about 29.6% of the total unit cell volume.

Table 3. Selected bond distances (Å) and angles (°) for **3**.

Bond distances (Å)					
Co(1)–N(2)	2.15	Co(1)–O(1)	2.20	N(3)–C(7)	1.16
Co(1)–N(3)	2.08	Co(1)–O(1')	2.04	S(1)–C(7)	1.66
Bond angles (°)					
O(1)–Co(1)–N(2)	88.4	N(2)–Co(1)–O(1')	92.1	Co(1)–N(3)–C(7)	172.0
O(1)–Co(1)–N(3)	94.6	N(3)–Co(1)–O(1')	93.7	S(1)–C(7)–N(3)	178.4
N(2)–Co(1)–N(3)	88.8				

Close comparison of the crystal structures of **1b** and **3**, reveals Co^{II} atom that are coordinated by either four (for **1b**) or two (for **3**) TPT ligands, indicating an increase of the metal to TPT ratio from **1b** to **3**. Therefore, an increase of the $Co(NCS)_2$ concentration during the reaction with TPT would promote a change in the structural organization of the 3D coordination network towards a tightly packed 2D coordination network. Moreover, the observed void volume is nearly three-fold smaller than the one observed in **1b** making complex **3** a less favorable host for guest molecules. In order to further study and provide insight into these three materials, we have performed a series of spectroscopic analyses. Specifically, these studies will prove essential in elucidating the solid-state transformation from **1b** to **2** due to its amorphous nature.

2.3.3 IR spectroscopy analysis

The FTIR spectra of **1b**, **2** and **3** each contain a band, characteristic for the CN stretch of the NCS^- anions, at 2050, 2085 and 2055 cm^{-1}, respectively (Figure 16). In all three cases, these values confirm the coordination of the NCS^- anions through the nitrogen atoms having values lower than 2100 cm^{-1}. The spectrum of **3** exhibits a broad band, centered at about 3350 cm^{-1}, for the symmetric and antisymmetric OH stretching of the H_2O and MeOH molecules,[21] while the spectrum of **2** shows a similar band with two maxima at 3285 and 3400 cm^{-1}. The latter finding testifies to the presence of H_2O molecules in the structure of **2**. However, the same band in the FTIR spectrum of **1b** is absent due to a significant broadening. Furthermore, water molecules could also be identified in the FTIR spectra of **1b**, **2** and **3** through their characteristic weak bands for HOH bending at 1615, 1610 and 1655 cm^{-1}.[21] The low-frequency region of the FTIR spectra of **1b**, **2** and **3** also exhibits a band characteristic for the librational modes of H_2O molecules,[21] centered at approximately 745 cm^{-1}. This band is due to the rotational oscillations of water molecules, restricted by interactions with neighboring atoms.

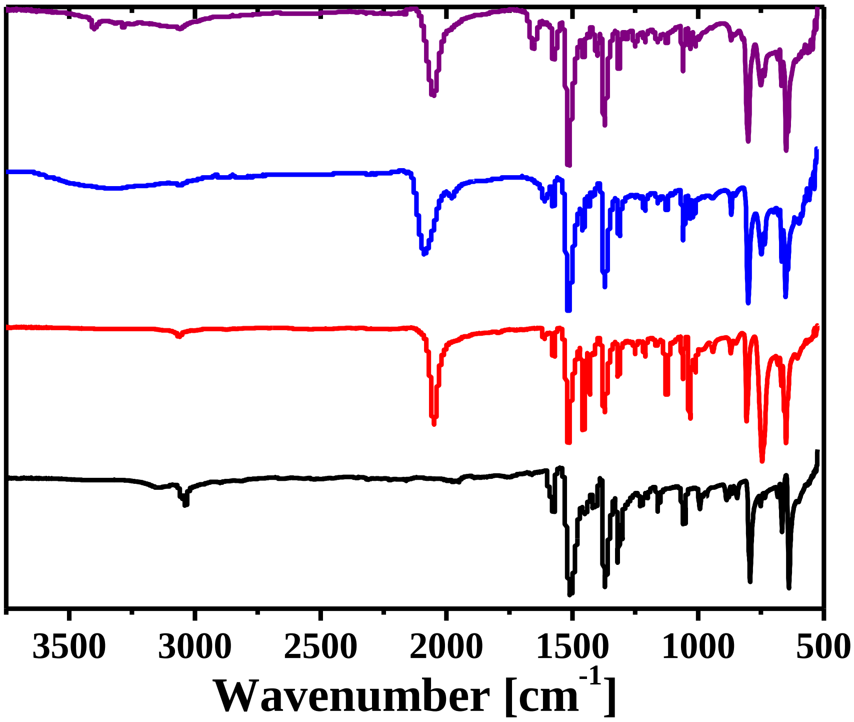

Figure 16: FTIR spectra of TPT (black), **1b** (red), **2** (purple) and **3** (blue) at 298 K.

Moreover, the spectrum of **1b** displays a set of pronounced bands, characteristic for the MeOH molecules, at 1035, 1435 and 1455 cm^{-1}. These bands are significantly less intense in the spectrum of **3**, which is due to a lesser amount of MeOH molecules in the structure of **3** compared to that of **1b**. These bands were not found in the spectrum of **2**, testifying to the absence of MeOH in this compound. Thus, the remarkable solid-state to solid-state transformation of **1b** to **2** can be explained by the spontaneous evaporation of the MeOH molecules, trapped in the cages of the former complex. This might also be supported by the fact that this transformation can occur in both aerobic and inert atmospheres, and hence, cannot be due to oxidation processes. Therefore, the cobalt ions retain their oxidation state, as confirmed by magnetic studies (*vide infra*). Additionally, the FTIR spectra of **1b**, **2** and **3** contain all the characteristic bands for the parent TPT ligand (Figure 16).

2.3.4 Thermogravimetric analysis

In order to determine the amount of solvent contained in the semi-amorphous material **2**, TGA experiments were carried out in comparison to that of the parent porous MOF, **1b**. The TGA analysis data of **1b** and **2** indicates that the latter complex resembles the composition of the former one, but exhibits a significantly lesser amount of solvent (Figure 17), following the solid-state to solid-state transformation. It should be noted that the TGA curves of **1b** and **2** in a dynamic air atmosphere are the same as those in a dynamic nitrogen atmosphere. Consequently, both complexes are completely burned with the formation of a stable residue regardless of the atmosphere, which can be explained by either the presence of oxygen, trapped in the porous structures, or the catalytic release of oxygen from solvents (H_2O and/or MeOH) during the thermal decomposition.

It was found that the molecule of **1b** is unstable even at room temperature and starts to decompose due to an extensive loss of solvent, which is shown in three steps, and corresponds to about 70% mass loss. The remaining two decomposition steps correspond to the burning of the

TPT and NCS⁻ ligands. Compound **2** is stable up to about 35 °C and decomposes in a very similar fashion as **1b**, however, the mass loss due to solvent evaporation in **2** is significantly less than in **1b** and constitutes approximately 35% of the total mass. In contrast to the TGA curves observed in **1b** and **2**, the thermal decomposition of **3** shows only a slight loss of mass up to 200 °C (approximately 10%), owing to the smaller amount of solvent molecules contained in the tightly packed 2D sheets (Figure 17).

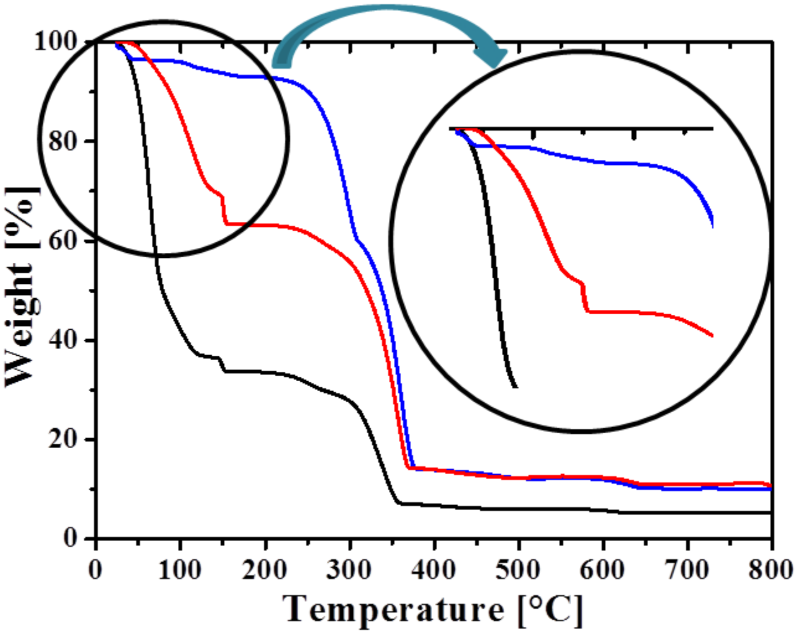

Figure 17: The thermogravimetric analyses (TGA) were carried out between 25–800 °C for **1b** (black), **2** (red) and **3** (blue). Measurements were performed under nitrogen atmosphere (25 mL/min) with a heating rate of 5 °C/min.

2.3.5 Diffuse reflectance spectroscopy analysis

In order to evaluate the solid-state to solid-state transformation of **1b** to **2**, which is accompanied by a color change, diffuse reflectance spectroscopy of both TPT and **1b** were analyzed. The diffuse reflectance spectrum of TPT contains a band with a shoulder exclusively in the UV region, which is attributed to intraligand *n*–*π** and *π*–*π** transitions (Figure 18). The diffuse reflectance spectra of **1b**, measured over time, each contain intense bands in the UV region arising from the same intraligand transitions for the organic ligand (Figure 19, A). These bands are accompanied with low-intense gradual shoulders up to about 540 nm, which correspond to the ligand-to-metal and metal-to-ligand charge transfers. The spectrum of **1b** at 0 h contains a broad band in the visible region, centered at 760 nm, corresponding to a d–d transition. In an octahedral field, the three spin-allowed electronic transitions from the ground state are $^4T_{1g}(F) \rightarrow {}^4T_{1g}(P)$, $^4T_{1g}(F) \rightarrow {}^4T_{2g}$ and $^4T_{1g}(F) \rightarrow {}^4A_{2g}$ (Appendix A). It is frequently reported that the $^4T_{1g}(F) \rightarrow {}^4A_{2g}$ transition is usually obscured due to its low intensity,[22] as the transition corresponds to a two-electron transfer between the $t^5_{2g}e^2_g$ (ground) to the $t^3_{2g}e^4_g$ (excited) configurations. Thus, the band at 760 nm corresponds to the $^4T_{1g}(F) \rightarrow {}^4T_{1g}(P)$ transition which is the main transition observed for octahedral high spin Co^{II} ions.[22] The $^4T_{1g}(F) \rightarrow {}^4T_{2g}$ transition would theoretically be observed at higher wavelengths since the energy level difference between the ground and excited states is smaller than the $^4T_{1g}(F) \rightarrow {}^4T_{1g}(P)$ transition.

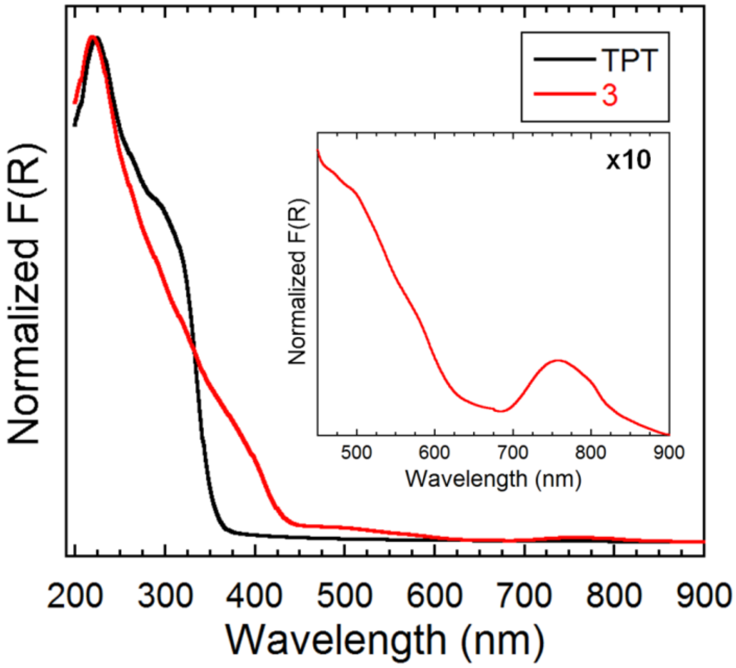

Figure 18: Normalized Kubelka-Munk spectra for TPT and **3**.

This adsorption band at 760 nm in the spectrum of **1b** at 0 h gradually decreases and exhibits a red-shift (~18 nm) over longer intervals of time (Figure 19, B). This process is accompanied by the gradual appearance of a new broad band with three maxima at approximately 560, 600 and 635 nm (Figure 18, C). This data strongly suggests a change in coordination of the Co^{II} ions from octahedral to tetrahedral.

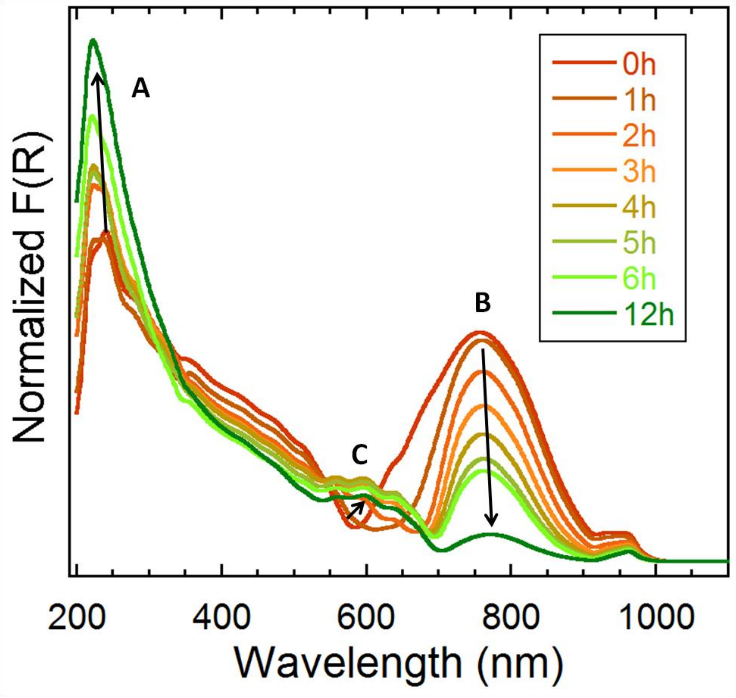

Figure 19: Normalized Kubelka-Munk spectra depicting the color change from orange (**1b**) to green (**2**) over time, with the black arrows displaying the significant changes in adsorption behavior.

Indeed, in a tetrahedral complex, the ligand field splitting is lower than in octahedral complexes, and therefore the transitions are observed in lower a frequency region. This was our first indication of a change in a coordination environment. Furthermore, is it common in the spectra of tetrahedral compounds to exhibit a fine structure due to transitions to doublet states in the same region.[23] Two bands are generally observed, corresponding to the $^4A_2 \rightarrow ^4T_1(P)$ and $^4A_2 \rightarrow ^4T_1(F)$ transitions. The former is attributed to the high-energy band which likely causes an additional band due to spin-orbital interactions. On the other hand, the latter is assigned to the low-energy band, thus supporting a tetrahedral environment of the Co^{II} cations in **2**. Recently, similar octahedral-tetrahedral transformations were reported by Dincă and Bloch in MOF systems.[10c,24] To unequivocally confirm these results, EXAFS (Extended X-ray Absorption Fine Structure) measurements are presently being investigated at the ESRF on compound **2**.

Compound **3** was also analyzed by diffuse reflectance spectroscopy in the solid-state (Figure 18). The spectrum exhibits an intense band, accompanied by a shoulder, in the UV region with maxima at 220 and 350 nm, respectively. These bands were attributed to intraligand n–π^* and π–π^* transitions. The ligand-to-metal and metal-to-ligand charge transfers were shown as low intense bands from about 450 to 640 nm, while the characteristic band centered at about 760 nm was assigned to the d-d transition, testifying to an octahedral coordination environment around the metal centers in **3**.

2.3.6 Magnetic properties

While the general molecular structure of **1b** is known, its potential as a magnetic MOF has not been previously investigated. Therefore, we set out to determine the magnetic properties of the parent compound **1b** in order to further elucidate the effects of structural reorganization, as observed in **3**, and of the structural collapse due to solvent loss for compound **2**. It must be noted that the magnetic measurements of compound **1b** were measured in paraffin oil in order to maintain its structural integrity and prevent solvent evaporation. Variable temperature dc susceptibility measurements were performed using a SQUID magnetometer at 1000 Oe in the temperature range of 1.8–300 K (Figure 20).

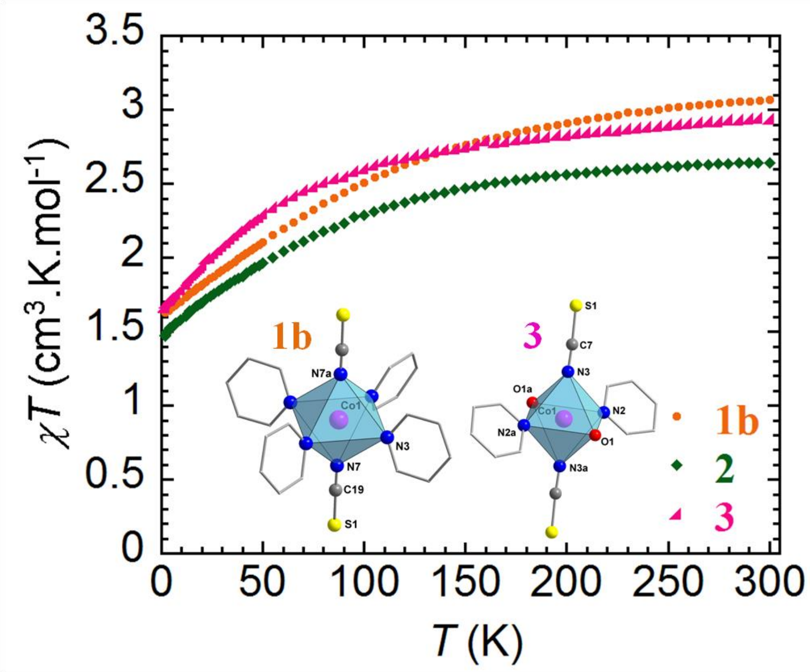

Figure 20: Temperature dependence of the magnetic susceptibility for complexes **1b–3** in a χT vs. T plot at 1000 Oe.

The room temperature χT products are 3.06 cm^3·K·mol^{-1}, 2.64 cm^3·K·mol^{-1} and 2.94 cm^3·K·mol^{-1}, for compounds **1b**, **2** and **3**, respectively. These values, while higher than the anticipated spin-only value of 1.88 cm^3·K·mol^{-1} for an S = 3/2 system, still fall in an acceptable range when compared to other experimentally observed high-spin Co^{II} ions with significant magnetic anisotropy.[25]

The χT values remain fairly constant down to 200 K for all compounds investigated, before gradually decreasing upon further cooling. In all cases, the decrease of the χT product is most likely a consequence of magnetic anisotropy and/or thermal depopulation of the excited states rather than antiferromagnetic interactions due to the large distance separating the Co^{II} ions.[26] This is especially valid for **1b** and **3**, where the shortest Co^{II}–Co^{II} distance is 13.39 Å and 8.37 Å, respectively. For **2**, due to structural rearrangements, it is not possible to definitively rule out intermolecular interactions, however, based on the fact that **2** contains tetrahedral Co^{II} ions, non-negligible anisotropy can be expected.[25d] To confirm the presence of magnetic anisotropy in

1b, **2** and **3**, field dependent magnetization measurements (*M* vs. *H*) and reduced magnetization studies were performed (Figure 21). In all cases, the magnetization curves reveal a rapid and steady increase of the magnetization at 1.8 K, without clear saturation at 7 T. The non-saturation, as well as the non-superimposition of the data at different temperatures in the *M* vs. *H/T* plots, confirms the presence of magnetoanisotropy.

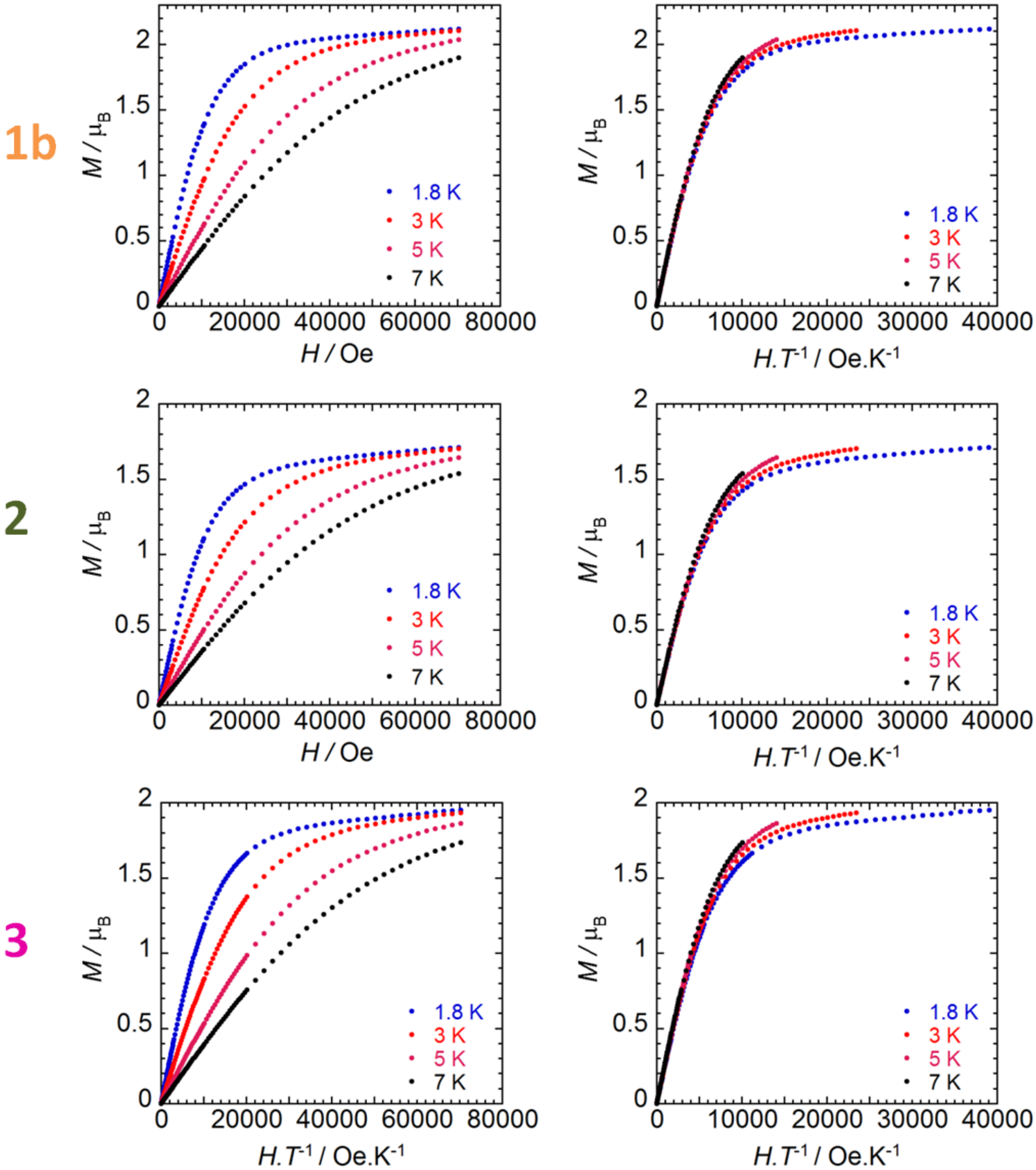

Figure 21: Magnetization versus field measurements at 1.8, 3, 5 and 7 K for **1b**, **2** and **3**, plotted as *M* vs *H* (left) and *M* vs *H/T* (right).

In recent years, mononuclear cobalt complexes with significant anisotropy were found to exhibit magnet-like behavior of slow relaxation of the magnetization.[26] This behavior is primarily arising from the inherent magnetic anisotropy of the metal center, which is strongly influenced by the ligand field and coordination geometry/environment. To investigate potential slow relaxation of the magnetization, temperature dependent ac susceptibilities were measured under applied dc fields of 0 and 1000 Oe for compounds **1b**, **2** and **3**. For all compounds, an ac signal was only present under applied dc fields of 1000 Oe (Appendix B). This is generally indicative of the presence of significant quantum tunneling of the magnetization which can be suppressed by applying an external magnetic field, through removal of the degeneration of the spin states. In the case of **1b**, the emergence of a clear peak rather than merely tails of peaks, as in the case of **2** and **3**, encouraged us to further examine the magnetic properties arising from this compound.

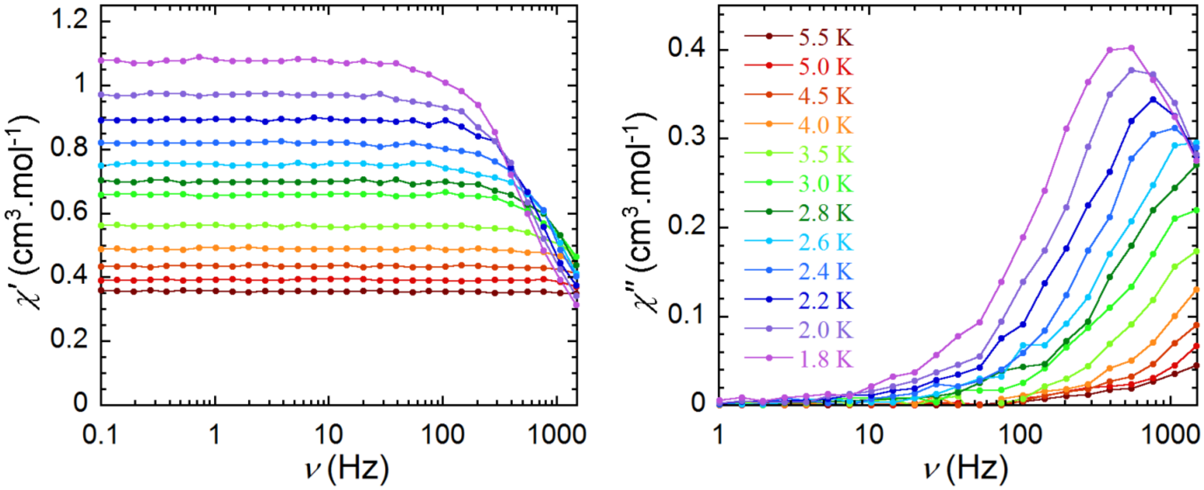

Figure 22: Frequency dependence of the in-phase χ' (top) and out-of-phase χ'' (bottom) magnetic susceptibilities for **1b** under an applied optimum dc field of H_{dc} = 600 Oe.

The optimum applied dc field for **1b**, where the minimum of the characteristic frequency was observed, was determined to be H_{dc} = 600 Oe. In the ac susceptibility data, the shifting of the peaks towards lower frequencies with decreasing temperatures is indicative of superparamagnet-like slow magnetization relaxation of a field-induced Single-Molecule Magnet (SMM) (Figure 22).

The thermally activated relaxation displays an Arrhenius-like behavior ($\tau = \tau_0 \exp(U_{\mathrm{eff}}/k\mathrm{T})$), where the anisotropic barrier obtained from the fitting is $U_{\mathrm{eff}} = 7.0$ K ($\tau_0 = 8.68 \times 10^{-6}$ s). This observed barrier is rather small yet comparable to other mononuclear Co$^{\mathrm{II}}$ SMMs.[27a, 28] The observable difference in the generation of slow magnetic relaxation between **1b** and **2** can be attributed to the change in coordination geometry (octahedral to tetrahedral) and environment, as clearly evidenced by diffuse reflectance spectroscopy. In theory, first-order orbital angular momentum, the principal contributor of magnetic anisotropy, is absent in a perfect tetrahedral geometry. However, it has been demonstrated that some distorted tetrahedral complexes exhibit non-negligible barriers even at zero applied dc fields.[29] In the present case, due to the amorphous nature of the material it is not possible to identify any distortions in the coordination environment, and consequently, magneto-structural correlations cannot be performed. Nevertheless, through ac susceptibility data we can once more conclude that **2** displays different structural features than the parent material **1b**. When comparing the magnetic behaviors of **1b** and **3**, the weak ac signal observed for **3** can again be explained by a change in coordination environment of the Co$^{\mathrm{II}}$ ion (*vide supra*). In comparison to **1b**, compound **3** sees two TPT nitrogen atoms replaced by two oxygen atoms from coordinated H_2O and/or MeOH molecules. This change induces weak ligand field around the metal center and smaller separation between the t_{2g} and e_g sets. Such a varation in the electronic configuration is known to lead to a change in the local anisotropy of the metal center (i.e. sign and strength)[29] which subsequently leads to weaker spin-orbital coupling. This results in a change of the superparamagnetic properties through a decrease of the energy barrier for magnetization reversal.

2.4 Conclusion

In conclusion, we have reported the well-refined X-ray structure of a well-known molecular sponge that has revolutionized single-crystal X-ray technology in recent years.[11] Our investigations into the stability of the Co^{II}-based molecular sponge have afforded insights on two surprising structural transformations. The instability of the porous MOF results in a gradual and observable solid-state transformation towards a semi-amorphous material, leading to a change in the coordination environment of the cobalt cations from octahedral to tetrahedral. Furthermore, we have revealed that careful monitoring of the reaction vessel for the synthesis of the molecular sponge is required in order to prevent methanol evaporation which could increase the local concentration of $Co(NCS)_2$, resulting in a drastic change of the coordination network, from three-dimensional to two-dimensional sheets (Figure 23).

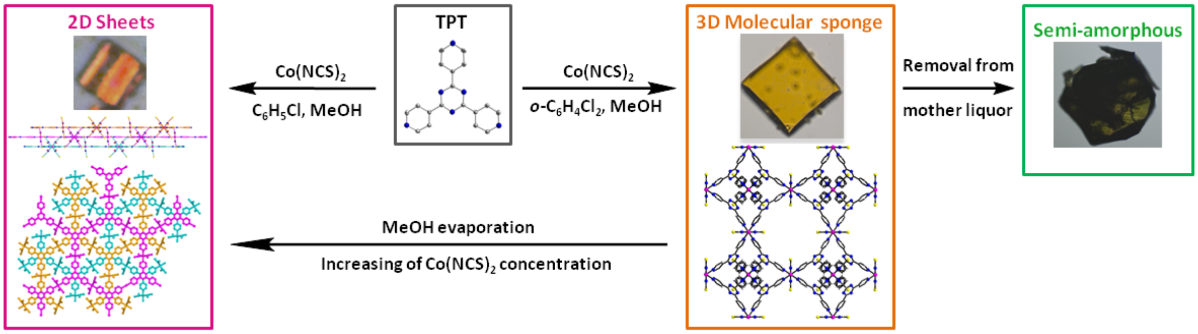

Figure 23: Summary of the structural transformations observed for the molecular sponge **1b**.

These findings are critical to take into account if one wants to utilize this well-known molecular sponge for single-crystal X-ray applications, such as the structural determination of molecules that are difficult to crystallize. In addition, we have also probed the magnetic behavior of the porous host indicating slow relaxation and SMM-like behavior under applied dc fields. Such magnet-like behavior of the host molecule, could provide important avenues towards the organization of paramagnetic guests molecules through applied magnetic fields. We hope that these findings will assist in the encapsulation of guests molecules, through a fundamental understanding of the stability of the highly porous magnetic framework.

2.5 References

[1] (a) Eddaoudi, M.; Kim, J.; Rosi, N.; Vodak, D.; Wachter, J.; O'Keeffe, M.; Yaghi, O. M. *Science* **2002**, *295*, 469. (b) Banerjee, R.; Furukawa, H.; Britt, D.; Knobler, C.; O'Keeffe, M.; Yaghi, O. M. *J. Am. Chem. Soc.* **2009**, *131*, 3875. (c) Farha, O. K.; Malliakas, C. D.; Kanatzidis, M. G.; Hupp, J. T. *J. Am. Chem. Soc.* **2010**, *132*, 950. (d) Kaye, S. S.; Dailly, A.; Yaghi, O. M.; Long, J. R. *J. Am. Chem. Soc.* **2007**, *129*, 14176. (e) Dincă, M.; Dailly, A.; Tsay, C.; Long, J. R. *Inorg. Chem.* **2008**, *47*, 11. (f) Lusby, P. J.; Müller, P.; Pike, S. J.; Slawin, A. M. Z. *J. Am. Chem. Soc.* **2009**, *131*, 16398.

[2] (a) Yaghi, O. M.; Li, H.; Davis, C.; Richardson, D.; Groy, T. L. *Acc. Chem. Res.* **1998**, *31*, 474. (b) Underhill, A. E.; Watkins, D. M. *Chem. Soc. Rev.* **1980**, *9*, 429. (c) Krishnamurty, K. V.; Harris, G. M.; Sastri, V. S. *Chem. Rev.* **1970**, *70*, 171. (d) Hoskins, B. F.; Robson, R. *J. Am. Chem. Soc.* **1989**, *111*, 5962. (e) Iwamoto, T.; Kitazawa, T.; Nishikiori, S.; Yuge, H. *J. Chem. Soc. Dalton* **1997**, 4127. (f) Cheetham, A. K.; Ferey, G.; Loiseau, T. *Angew. Chem. Int. Ed*. **1999**, *38*, 3268. (g) Kondo, M.; Yoshitomi, T.; Seki, K.; Matsuzaka, H.; Kitagawa, S. *Angew. Chem., Int. Ed.* **1997**, *36*, 1725.

[3] (a) Yaghi, O. M.; Li, G.; Li, H. *Nature,* **1995**, *378*, 703. (b) Kondo, M.; Yoshitomi, T.; Seki, K.; Matsuzaka, H.; Kitagawa, S. *Angew. Chem. Int. Ed. Engl.* **1997**, *36*, 1725.

[4] (a) Eddaoudi, M.; Moler, D. B.; Li, H.; Chen, B.; Reineke, T. M.; O'Keeffe, M.; Yaghi, O. M. *Acc. Chem. Res.* **2001**, *34*, 319. (b) Yaghi, O. M.; O'Keeffe, M.; Ockwig, N. W.; Chae, H. K.; Eddaoudi, M.; Kim, J. *Nature* **2003**, *423*, 705. (c) Kitagawa, S.; Kitaura, R.; Noro. S. *Angew. Chem. Int. Ed.* **2004**, *43*, 2334. (d) Banerjee, R.; Phan, A.; Wang, B.; Knobler, C.; Furukawa, H.; O'Keeffe, M.; Yaghi, O. M. *Science* **2008**, *319*, 939. (e) Tranchemontagne, D. J.; Mendoza-Cortés, J. L.; O'Keeffe, M.; Yaghi, O. M. *Chem. Soc. Rev.* **2009**, *38*, 1257. (f) O'Keeffe, M.; Yaghi, O. M. *Chem. Rev.* **2012**, *112*, 675. (g) Sato, H.; Kosaka, W.; Matsuda, R.; Hori, A.; Hijikata, Y.; Belosludov, R. V.; Sakaki, S.; Takata, M.; Kitagawa, S. *Science* **2014**, *343*, 167. (h) McKellar, S. C.; Graham, A. J.; Allan, D. R.; Mohideen, M. I. H.; Morris, R. E.; Moggach, S. A. *Nanoscale* **2014**, *6*, 4163. (i) Anserson, J. S.; Gallagher, A. T.; Mason, J. A.; Harris, T. D. *J. Am Chem. Soc.* **2014**, *136*, 16489.

[5] (a) Rosi, N. L.; Eckert, J.; Eddaoudi, M.; Vodak, D. T.; Kim, J.; O'Keeffe, M.; Yaghi, O. M. *Science* **2003**, *300*, 1127. (b) Murray, L. J.; Dincă, M.; Long, J. R. *Chem. Soc. Rev.* **2009**, *38*, 1294. (c) Lim, D.-W.; Chyun, S. A.; Suh, M. P. *Angew. Chem. Int. Ed.* **2014**, *54*, 7819. (d) Suh,

M. P.; Park, H. J.; Prasad, T. K.; Lim, D.-W. *Chem. Rev.* **2012**, *112*, 782. (e) Hu, Y. H.; Zhang, L. *Adv. Mater.* **2010**, *22*, E117. (f) Filinchuk, Y.; Richter, B.; Jensen, T. R.; Dmitriev, V.; Chernyshov, D.; Hagemann, H. *Angew. Chem. Int. Ed.* **2011**, *50*, 11162. (g) Ley, M. B.; Ravnsbæk, Filinchuk, Y.; Lee, Y.-S.; Janot, R.; Cho, Y. W.; Skibsted, J.; Jensen, T. R. *Chem. Mater.* **2012**, *24*, 1654. (h) Getman, R. B.; Bae, Y.-S.; Wilmer, C. E.; Snurr, R. Q. *Chem. Rev.*, **2012**, *112*, 703. (i) Sumida, K.; Rogow, D. L.; Mason, J. A.; McDonald, T. M.; Bloch, E. D.; Herm, Z. R.; Bae, T.-H.; Long, J. R. *Chem. Rev.*, **2012**, *112*, 724. (j) Suh, M. P.; Park, H. J.; Prasad, T. K.; Lim, D.-W. *Chem. Rev.*, **2012**, *112*,782.

[6] (a) Halder, G. J.; Neville, S. M.; Kepert, C. J. *CrystEngComm* **2005**, *7*, 266. (b) Gamez, P.; Reedijk, J. *Eur. J. Inorg. Chem.* **2006**, 29. (c) Arcís-Castillo, Z.; Muñoz, M. C.; Molár, G.; Bousseksou, A.; Real, J. A. *Chem. Eur. J.* **2013**, *19*, 6851. (d) Fu, Z.; Chen, Y.; Zhang, J.; Liao, *J. Mater. Chem.* **2011**, *21*, 7895. (e) Chang, Z; Zhang, D.-S.; Hu, T.-L.; Bu, X.-H. *Inorg. Chem. Commun.* **2011**, *14*, 1082. (f) Batten, S. R.; Hoskins, B. F.; Robson, R. *J. Am. Chem. Soc.* **1995**, *117*, 5385.

[7] Lehn, J.-M. Supramolecular Chemistry, Wiley-VCH, Weinheim, **1995**.

[8] (a) Kawano, M.; Fujita, M. *Coord. Chem. Rev.* **2007**, *251*, 2592. (b) Yoshizawa, M.: Klosterman, J. K.; Fujita, M. *Angew. Chem. Int. Ed.* **2009**, *48*, 3418.

[9] Inokuma, Y.; Yoshioka, S.; Ariyoshi, J.; Arai, T.; Hitora, Y.; Takada, K.; Matsunaga, S.; Rissanen, K.; Fujita, M. *Nature* **2013**, *495*, 461.

[10] (a) Vinogradova, E. V.; Müller, P.; Buchwald, S. L.; *Angew. Chem.* **2014**, *126*, 3189. (b) Mori, K.; Akasaka, K.; Matsunaga, S. *Tetrahedron* **2014**, *70*, 392. (c) Bloch, W. M.; Burgun, A.; Coghlan, C. J.; Lee, R.; Coote, M. L.; Doonan, C. J.; Sumby, C. J. *Nature Chem.* **2014**, *6*, 906.

[11] Inokuma, Y.; Arai, T.; Fujita, M. *Nature Chem.* **2010**, *2*, 780.

[12] (a) Habib, F.; Luca, O. R.; Vieru, V.; Shiddiq, M.; Korobkov, I.; Gorelsky, S; I.; Takase, M. K.; Chibotaru, L. F.; Hill, S.; Crabtree, R. H.; Murugesu, M. *Angew. Chem. Int. Ed.* **2013**, *52*, 11290. (b) Jurca, T.; Farghal, A.; Lin, P.-H.; Korobkov, I.; Murugesu, M.; Richeson, D. S. *J. Am. Chem. Soc.* **2011**, *133*, 15814. (c) Habib, F.; Brunet, G.; Vieru, V.; Korobkov, I.; Chibotaru, L. F.; Murugesu, M. *J. Am. Chem. Soc.* **2013**, *135*, 13242.

[13] Aulakh D.; Pyser, J. B.; Zhang, X.; Yakovenko, A. A.; Dunbar, K. R.; Wriedt, M. *J. Am. Chem. Soc.* **2015**, *137*, 9254.

[14] (13) (a) Xiang, S.; Wu, X.; Zhang, J.; Fu, R.; Hu, S.; Zhang, X. *J. Am. Chem. Soc.* **2005**, *127*, 16352. (b) Sibille, R.; Mazet, T.; Malaman, B.; Gaudisson, T.; François, M. *Inorg. Chem.*

2012, *51*, 2885. (c) Huang, Z.-L.; Drillon, M.; Masciocchi, N.; Sironi, A.; Zhao, J.-T.; Rabu, P.; Panissod, P. *Chem. Mater.* **2000**, *12*, 2805. (d) Kurmoo, M. *Chem. Soc. Rev.* **2009**, *38*, 1353. (e) Aharen, T.; Habib, F.; Korobkov, I.; Burchell, T. J.; Guillet-Nicolas, R.; Kleiz, F.; Murugesu, M. *Dalton Trans.* **2013**, *42*, 7795. (f) Rujiwatra, A.; Kepert, C. J.; Claridge, J. B.; Rosseinsky, M. J.; Kumagai, H.; Kurmoo, M. *J. Am. Chem. Soc.* **2001**, *123*, 10584.

[15] Li, M.-X.; Miao, Z.-X.; Shao, M.; Liang, S.-W.; Zhu, S.-R. *Inorg. Chem*. **2008**, *47*, 4481.

[16] *APEX Software Suite v. 2010*, Bruker AXS, Madison, WI, **2005**.

[17] Blessing, R. *Acta Cryst.* **1995**, *A51*, 33.

[18] Spek, A. L. *Acta. Cryst.* **1990**, *A46*, C-34.

[19] Sheldrick, G. M. *Acta Cryst.* **2008**, *A64*, 112.

[20] (a) Li, M.-Y.; Sevov, S. C. *CrystEngComm* **2013**, *15*, 5107. (b)Yi, F.-Y.; Zhang, J.; Zhang, H.-X.; Sun, Z.-M. *Chem. Commun.* **2012**, *48*, 10419. (c) Barrios, L. A.; Ribas, J.; Aromí, G. *Inorg. Chem.* **2007**, *46*, 7154. (d) Neville, S. M.; Halder, G. J.; Murray, K. S.; Moubaraki, B.; Kepert, C. J. *Aust. J. Chem.* **2013**, *66*, 452. (e) Dybtsev, D. N.; Chun, H.; Kim, K. *Chem. Commun.* **2004**, 1594. (f) Abrahams, B. F.; Batten, S. R.; Hamit, H.; Hoskins, B. F.; Robson, R. *Chem. Commun.* **1996**, 1313. (g) Kilbas, B.; Mirtschin, S.; Riis-Johannessen, T.; Scopelliti, R.; Severin, K. *Inorg. Chem.* **2012**, *51*, 5795.

[21] Nakamoto, K. *Infrared and Raman Spectra of Inorganic and Coordination Compounds*, Part B, 5th Edition, Wiley, N. Y., **1997**, pp. 116.

[22] Askalani, P. *Transition Met. Chem.* **1986**, *11*, 469.

[23] Nishat, N.; Parveen, S.; Dhyani, S.; *J. Coord. Chem.* **2009**, *62*, 1091.

[24] Brozek, C. K.; Dincă, M. *Chem. Soc. Rev*. **2014**, *43*, 5456.

[25] (a) Liu, T.-F.; Fu, D.; Gao, S.; Zhang, Y.-Z.; Sun, H. L.; Su, G.; Liu, Y.-J. *J. Am. Chem. Soc.* **2003**, *125*, 13976. (b) Habib, F.; Cook, C.; Korobkov, I.; Murugesu, M. *Inorg. Chim. Acta.* **2012**, *380*, 378. (c) Mabbs, F. E.; Machin, D. J.; *Magnetism and Transition Metal Complexes*, Dover, Mineola, N. Y., **2008**. (d) Zadrozny, J. M.; Long, J. R. *J. Am. Chem. Soc.* **2011**, *133*, 20732. (e)

[26] (a) Vallejo, J.; Castro, I.; Ruiz-García, R.; Cano, J.; Julve, M.; Lloret, F.; De Munno, G.; Wernsdorfer, W.; Pardo, E. *J. Am Chem. Soc.* **2012**, *134*, 15704. (b) Huang, W.; Liu, T.; Wu, D.; Cheng, J.; Ouyang, Z. W.; Duan, C. *Dalton Trans.* **2013**, *42*, 15326.

[27] (a) Gomez-Coca, S.; Cremades, E.; Aliaga-Alcalde, N.; Ruiz, E. *J. Am. Chem. Soc.* **2013**, *135*, 7010. (b) Zhu, Y.-Y.; Cui, C.; Zhang, Y.-Q.; Jia, J.-H.; Guo, X.; Gao, C.; Qian, K.; Jiang, S.-D.; Wang, B.-W.; Wang, Z.-M.; Gao, S. *Chem. Sci.* **2013**, *4*, 1802. (c) Cao, D.-K.; Feng, J.-

Q.; Ren, M.; Gu, Y.-W.; Song, Y.; Ward, M. D. *Chem. Commun.* **2013**, *49*, 8863. (d) Caneschi, A.; Gatteschi, D.; Lalioti, N.; Sessoli, R,; Sorace, L.; Tangoulis, V.; Vindigni, A. *Chem. Eur. J.* **2002**, *8*, 286. (e) Kanegawa, S.; Karasawa, S.; Maeyama, M.; Nakano, M.; Koga, N. *J. Am. Chem. Soc.* **2008**, *130*, 3079.

[28] (a) Zadrozny, J. M.; Liu, J.; Piro, N. A.; Chang, C. J.; Hill, S.; Long, J. R. *Chem. Commun.* **2012**, *48*, 3928. (b) Rajnák, C.; Titiš, J.; Fuhr, O.; Ruben, M.; Boča, R. *Inorg. Chem.* **2014**, *53*, 8200.

[29] (a) Vaidya, S.; Upadhyay, A.; Singh, S. K.; Gupta, T.; Tewary, S.; Langley, S. K.; Walsh, J. P. S.; Murray, K. S.; Rajaraman, G.; Shanmugam, M. *Chem. Commun.* **2015** DOI: 10.1039/C4CC08305A. (b) Zadrozny, J. M.; Telser, J.; Long, J. R. *Polyhedron* **2013**, *64*, 209. (c) Saber, M. R.; Dunbar, K. R. *Chem. Commun.* **2014**, *50*, 12266.

Chapter 3

Exceptionally High Iodine Uptake in a Metal-Organic Framework Visualized Through Stepwise Crystallographic Transformations

Abstract

The observation of gas adsorption dynamics at the atomic level remains a significant challenge today due to the difficulties associated with structural characterization of porous materials following the encapsulation of gaseous guests. The present study provides structural insights into the incorporation of molecular iodine (I_2) inside the pores of a metal-organic framework (MOF). The flexible nature of the MOF was quintessential in retaining adequate crystallinity after confinement of I_2. Our methodology provides the stepwise visualization of the capture of I_2, through single-crystal X-ray crystallography, demonstrating the sequential exchange of solvent molecules for the I_2 guests. These results illustrate that the I_2 guests participate in two processes of adsorption; physisorption and chemisorption, thus leading to a variety of polyiodide species. Herein, we identify the locations of the preferred adsorption sites and the respective occupancies of the encroaching I_2 guests, as well as investigate the impact of adsorption on the host framework, which are requisites in the improvement of high-capacity iodine capture materials.

3.1 Introduction

Due to the numerous instabilities of the Co-based MOF, **1b**, outlined in chapter 2, we then focused our attention towards another porous MOF capable of displaying similar guest encapsulation properties. Hence, a Zn-based MOF was carefully selected to further investigate the crystalline sponge method introduced by Fujita and co-workers.[1] This MOF was first reported in 2002, and describes the fascinating swelling behavior of a three-dimensional network.[2] More specifically, the framework contracts following the removal of guest molecules, and more importantly, is able to reversibly expand after a guest is readsorbed (Figure 24). This behavior is highly attractive for the purpose encapsulating guest molecules, since it demonstrates an adaptability of the framework for various guests. Conventional porous media are rigid and would not promote the same level of favorable guest-host interactions.

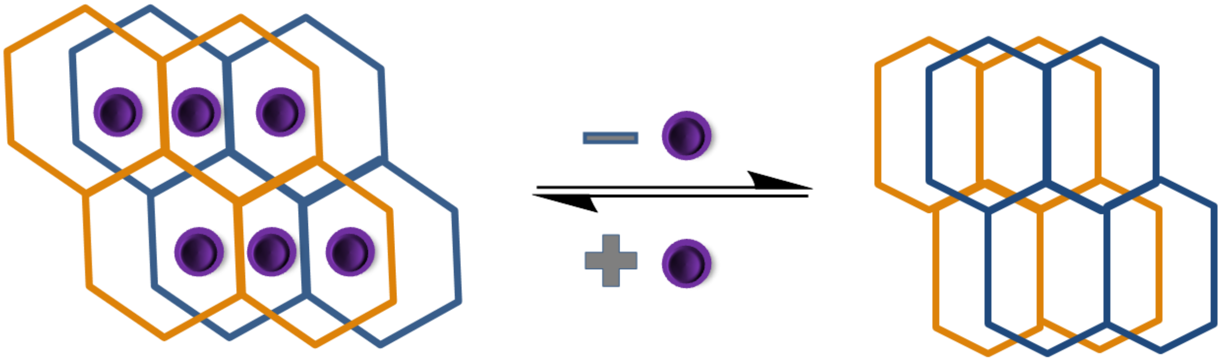

Figure 24: Schematic representation of the contraction and expansion of the Zn-based MOF upon the removal or addition of guest substrates. This figure is inspired by Fujita *et al.* (2002).[2]

As a reminder, a crystalline sponge refers to the regular ordering of guest molecules within single-crystals of porous MOFs, which can then be analyzed by X-ray techniques. The Zn-based crystalline sponge has demonstrated clear potential in absorbing and orienting guest molecules for X-ray crystallography. Namely, it has been used to identify guaiazulene, a natural hydrocarbon, when using only nanograms of the guest compound.[1] In order to familiarize ourselves with the crystalline sponge method, we were first interested in testing the incorporation of small molecules. In particular, the capture and sequestration of highly mobile volatile radionuclides such as ^{129}I, ^{131}I, ^{3}H and ^{85}Kr was of interest due to their relevance in waste products generated from the nuclear fission of uranium. Over 10% of the world's energy is supplied by nuclear power plants,[3] and this number will continue to experience a significant amount of growth in the near future.[4] Although this sector of energy does provide the benefit of emitting negligible amounts of greenhouse gases, it requires particular attention in the area of nuclear waste management; in terms of safely handling and managing the rising amounts of radioactive waste. One radionuclide that must be addressed is radiological iodine, since it can be incorporated in the human metabolic system (accumulates in the thyroid gland) and has a very long half-life of 1.57 x 10^7 years.[5] Hence, the capture of radioactive iodine is becoming an extensive area of research in the field of capture materials. Solid state porous materials are becoming an increasingly viable technology for the capture of gaseous products due to their large permanent surface areas, suitable pore size distributions and favorable enthalpies of adsorption.

The prevalent method for the capture of radioactive iodine is utilizing metal-exchanged zeolites, more specifically a silver-exchanged mordenite. In these systems, the ionic silver particles react with molecular iodine (I_2) to form silver iodide nanocrystals.[6] While these materials exhibit high thermal and chemical stabilities, their limited adsorption capacities lead to low iodine uptake values. Therefore, a number of research groups are investigating alternative porous materials for the capture of iodine that have higher loading capacities and potentially lower costs. Recently, the elegant work of T. M. Nenoff and co-workers has demonstrated the use of MOFs as high-capacity iodine adsorbents.[7] In pursuit of improving solid state storage using porous materials, MOFs provide a new and exciting avenue to explore due to their facile functionalization, high surface area, and flexible nature upon guest uptake. With this in mind, the selected MOF offers framework flexibility to accommodate a variety of guest species.

Furthermore, the ability to regularly order guest compounds within single-crystals of the MOF was particularly attractive since it promises to offer the direct structural visualization of gaseous encapsulation. Similar approaches have been carried out to demonstrate the stepwise visualization of guest-host interactions between a MOF and a gaseous substrate; however such studies remain extremely rare due to the difficulty in retaining high crystallinity.[8] This work represents the first study of its kind for I_2 inclusion, and provides unique insights into the mechanistic aspects of gaseous guest encapsulation. The stepwise methodology allows for a more in-depth understanding of the type of iodine species formed and their preferred locations of adsorption, which are essential components in the rational design of iodine capture materials.

The crystalline sponge in question is built from metal nodes of ZnI_2 linked by the same 2,4,6-tris-(4-pyridyl)-1,3,5-triazine (TPT) ligand that was employed for **1b**. The combination of these building blocks lead to the formation of stable single crystals of $\{[(ZnI_2)_3(TPT)_2]\cdot 5.5(C_6H_5NO_2)\}_n$ (**4**).[2] The specific use of this host for I_2 uptake also offers the fascinating potential of exhibiting both processes of adsorption; that of physisorption and chemisorptions. Physical adsorption, or physisorption, refers to an adsorption where the forces between the guest and the host are minimal, and hence are based on weak van der Waals forces. This type of adsorption does not significantly alter the electronic structure of the guest species involved, and is generally a reversible process. Chemical adsorption, or chemisorptions, involves forces stronger than van der Waals interactions, and involves the formation of covalent or ionic bonds. In turn, this signifies a certain level of chemical specificity of the host for the guest compound. Generally, chemisorption requires harsher conditions to remove the chemisorbed species due to the stronger interactions. Accordingly, the terminal iodide ions which are part of the framework of **4**, may participate in chemisorption. Indeed, iodine exhibits fascinating chemistry, both chemically and structurally. In particular, its oxidative ability has resulted in the development of a number of important synthetic and catalytic processes.[9] Furthermore, the rich variety of iodine species, ranging from simple I^- and IO_3^- anions, to polyiodides such as I_3^- and I_4^{2-}, allow for intruiging physicochemical properties, including physisorption and chemisorption.

The combination of large pores (maximum cross section of 8 x 5 Å^2) with the prospect of chemisorption, leading to stronger bonding of the I_2 units, make this MOF an attractive candidate for the capture and storage of radioactive iodine. Indeed, Kawano *et al.* previously demonstrated the potential of I_2 inclusion in non-interpenetrated structures of **4** obtained through phase-transitions,[10] however no reports have been made on the as-synthesized doubly interpenetrated structure. It is also important to note that these studies confirmed the incorporation of I_2 through synchrotron X-ray powder diffraction data, while the work presented herein employed single-crystal to single-crystal transformations to elucidate highly accurate and precise molecular structures using SCXRD.

3.2 Experimental section

3.2.1 General considerations

Starting materials and solvents were purchased and used without further purification from commercial suppliers (Strem Chemicals, Sigma-Alrich and Fisher Scientific). All manipulations, unless otherwise stated, were performed under aerobic/ambient conditions.

3.2.2 Synthesis

The 2,4,6-tris(4-pyridyl)-1,3,5-triazine (TPT) ligand and compound **4**, $\{[(ZnI_2)_3(TPT)_2]\cdot 5.5(C_6H_5NO_2)\}_n$, were synthesized according to previously reported methods.[2,11] The synthetic protocol of the TPT ligand is also described in the experimental section of Chapter 2. Single-crystals of **4** were obtained by layering a methanol solution of ZnI_2 (9.6 mg in 1 mL) onto a nitrobenzene solution of TPT (6.3 mg in 4 mL) in a test-tube with a length of 25 cm and a width of 1 cm. In order to dissolve the TPT ligand in nitrobenzene, the solution was sonicated for 5 min, or until all visible residues were dissolved. Furthermore, careful layering of the zinc iodide solution is crucial towards preparing high quality single-crystals and is achieved by slowly adding this solution on the walls of the test-tube using a 1 mL syringe in a manner to prevent disturbing the denser nitrobenzene solution. The test-tube is then capped using Parafilm. After approximately 5-7 days, colorless single-crystals of **4** were isolated in 71% yield. NMR ^{1}H (DMSO, 400 MHz): δ 7.64, (t, 2H, nitrobenzene), 7.82 (t, 1H, nitrobenzene), 7.82 (d, 2H, nitrobenzene), 8.62 (d, 6H, TPT), 8.93 (d, 6H, TPT). Selected IR (cm^{-1}): 3066 (w), 1618 (w), 1575 (w), 1514 (s), 1477 (m), 1422 (w), 1374 (m), 1343 (s), 1315 (m), 1213 (w), 1160 (w), 1106 (w), 1058 (m), 1025 (m), 934 (w), 868 (w), 850 (m), 804 (s), 792 (m), 732 (w), 702 (s), 668 (m), 655 (s).

High-quality single-crystals of **4** were carefully selected under optical microscope and inserted in a 5 mL glass vial. This vial was subsequently placed in a 40 mL vial containing ~100 mg of crushed iodine pellets and was then capped and sealed using Parafilm. Following 3, 6 and 15 hours of exposure time to the iodine vapors, the darkened crystals were then immediately mounted on a common laboratory diffractometer yielding compounds **5**, **6** and **7**, respectively. It is important to note that iodine (I_2) is inactive in IR because the symmetrical nature of the diatomic molecule produces no change in the dipole moment. Furthermore, ^{127}I NQR (nuclear quadrupole resonance) has been extensively attempted, however no signal could be observed. Thus, bulk characterization for iodine loaded samples is based off thermogravimetric analysis and diffuse reflectance spectroscopy, which are discussed herein.

3.2.3 Physical measurements

Infrared spectra were recorded with a Varian 640 FTIR spectrometer equipped with an ATR in the 500–4000 cm^{-1} range.

Reflectance spectra were measured with a Varian Cary-100 spectrophotometer using polytetrafluoroethylene (PTFE) as a reference. Kubelka-Munk spectra were normalized to allow meaningful comparisons.

Thermogravimetric analysis (TGA) data were recorded using a Q5000 IR TGA instrument at a heating rate of 10 °C/min between room temperature and 1000 °C , under a constant flow of nitrogen (25 mL/min).

3.2.4 Single Crystal X-ray Diffraction Studies

The single-crystal samples were mounted on thin glass fibers using paraffin oil. Prior to data collection, the crystals were cooled to 200 K. Data were collected on a Bruker AXS KAPPA single-crystal diffractometer equipped with a sealed Mo tube source (wavelength 0.71073 Å) APEX II CCD detector. Raw data collection and processing were performed with APEX II software package from BRUKER AXS. Diffraction data for all three samples were collected with a sequence of 0.3° ω scans at 0, 90, 180 and 270° in φ. Initial unit cell parameters were determined from 80 data frames with 0.3° ω scan each, collected at the different sections of the Ewald sphere. Semi-empirical absorption corrections based on equivalent reflections were applied. Systematic absences in the diffraction data-set and unit-cell parameters were consistent with the monoclinic $P2_1/c$ (№14) space group for compounds **5** and **6**. Unit cell symmetry for the crystal of **7** was assigned as monoclinic $P2/n$ (№13, non-standard settings) based on the same information. Solutions in centrosymmetric space groups for all three samples yielded chemically reasonable and computationally stable results of refinement. The structures were solved by direct methods, completed with difference Fourier synthesis, and refined with full-matrix least-squares procedures based on F^2.

Table 4: Summary of the crystal structure data and refinement for compounds **4–7**.

Complex	**4**[2]	**5**	**6**	**7**
Formula	$C_{69}H_{51.5}I_6N_{17.5}O_{11}Zn_3$	$C_{102}H_{73}I_{14}N_{29}O_{10}Zn_6$	$C_{90}H_{63}I_{15.38}N_{27}O_6Zn_6$	$C_{72}H_{48}I_{21.3}N_{24}Zn_6$
FW, g mol^{-1}	2259.29	4033.71	3962.61	4344.53
Crystal system	monoclinic	monoclinic	monoclinic	monoclinic
Space group	$C2/c$	$P2_1/c$	$P2_1/c$	$P2/n$
T, K	193(2)	200(2)	200(2)	200(2)
a, Å	36.079(10)	35.143(5)	35.047(15)	30.839(4)
b, Å	14.978(4)	15.039(2)	15.0048(8)	14.9128(18)
c, Å	30.734(9)	30.680(4)	30.5654(15)	34.344(4)
α, °	90	90	90	90
β, °	102.470(5)	101.549(4)	101.464(2)	99.929(7)
γ, °	90	90	90	90
V, Å^3	16 217(8)	15 887(4)	15 752.9(15)	15 558(3)
Z	8	4	4	4
ρ_{calcd}, g cm^{-3}	1.851	1.686	1.671	1.855
μ (Mo, Kα), mm^{-1}	3.231	3.663	3.957	5.171
reflns collected	14 243	22 219	38 776	19 152
$R1$, $wR2$ ($I > 2\sigma(I)$)[a]	0.0794, 0.2316	0.1839, 0.4540	0.2037, 0.4898	0.2911, 0.6451
$R1$, $wR2$ (all data)	0.1278, 0.2697	0.1997, 0.4636	0.2280, 0.5031	0.3289, 0.6736

[a] $R = R1 = | |F_o| - |F_c|/|F_o|$; $wR2 = \{[w(F_o - F_c^2)^2] / [w(F_o^2)^2]\}^{1/2}$; $w = 1/[\sigma_2(F_o^2) + (ap)^2 + bp]$, where $p = [\max(F_o^2, 0) + 2 F_c^2]/3$; and $Rw = [w(|F_o| - | F_c|)^2 / w|F_o|^2]^{1/2}$, where $w = 1 / \sigma^2(|F_o|)$.

3.2.5 Computational studies

All electronic and structural calculations were performed using periodic density functional theory (DFT) calculations, carried out in the Vienna ab initio simulation package (VASP). The PBE exchange-correlation functional and PAW potentials were used with a plane wave cut-off of 520 eV with a convergence set to a change of 2×10^{-5} eV/Å. The semi-empirical dispersion potential correction of Grimme was used for the energy and force calculations with the default parameters for the PBE functional. Gamma-point was used to sample the Brillouin zone. NBO analysis was employed on two cluster models of **5** and **6** using NBO6.0 software. These cluster models were built from the structures obtained by DFT calculations. The NBO calculations were performed at M06-2x level of theory. The aug-cc-pVDZ-PP basis set was used on the iodide atoms, the LANL2DZ basis set was used on the Zn atoms, and the 6-31g* basis set was used on all remaining atoms in both clusters.

3.3 Results and discussion

3.3.1 Synthesis

The host MOF is synthesized by the slow diffusion of a solution of zinc iodide in methanol into a nitrobenzene/methanol solution of TPT, yielding colorless single-crystals that initially contain nitrobenzene as guest molecules. Upon exposure of **4** to I_2 vapors in a closed vessel at room temperature, a pronounced and rapid color change from colorless to black could be observed (Figure 25). We successfully obtained three new crystal structures by varying the time of exposure of **1** to the I_2 vapors from 3 to 15 h, providing us with vital information on the mechanism by which I_2 becomes incorporated in the MOF. It is noteworthy that a further increase in the time of exposure of **4** to I_2 results in weaker diffraction and eventual loss of crystallinity, thus rendering structural analyses more challenging. Nevertheless, the host framework continues the uptake of I_2 up to approximately 72 h, after which the MOF becomes saturated (*vide infra*). The degree of I_2 encapsulation will likely depend on the size of the crystals,[10a] and therefore, efforts were made to select single-crystals of approximately equal size for the SCXRD experiments.

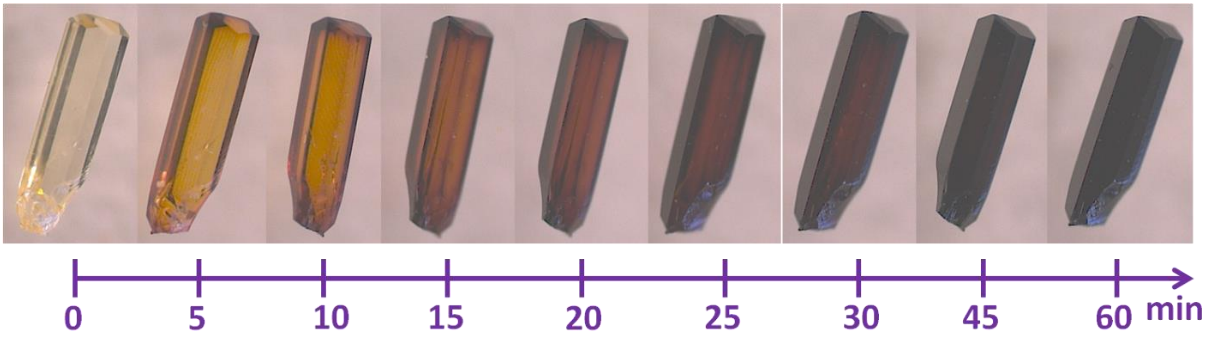

Figure 25: Photographs demonstrating the color change associated with the exposure of single-crystals of **4** to I_2 vapors, as viewed under optical microscope.

Due to the difficulty in applying the crystalline sponge method and the scarcity of reported compounds analyzed by this technique, Fujita and co-workers recently published a protocol to enhance the success rate of crystal-free crystallography.[12] As previously mentioned, the pores of crystals of **4** are initially filled with nitrobenzene, which can bind to the host through strong π–π interactions with the TPT ligand. Consequently, it is suggested that nitrobenzene must first be replaced by another solvent, in order to facilitate the inclusion of guest compounds. Cyclohexane was selected as an inert solvent since it readily replaces nitrobenzene, when single-crystals of **4** are immersed in cyclohexane for 5 days and is weakly trapped in the pores. With respect to I_2 inclusion, it was found that this nitrobenzene-cyclohexane solvent exchange was not necessary; the interactions formed by I_2 guests were found to be more favorable than the ones with nitrobenzene (*vide infra*). Additionally, by foregoing this process we prevent the single-crystals from cracking and losing transparency, ensuring high-quality single-crystals for guest-included crystalline sponges.

3.3.2 First structural intermediate

The first structure, obtained after 3 h of **4** being exposed to vapors of I_2, revealed large peaks of electron density within the pores, which were identified as an I_2 molecule. The topology of the framework remains unchanged upon I_2 inclusion, however we can observe the incorporation of a new guest, giving the first intermediate $\{[(ZnI_2)_6(TPT)_4]\cdot(I_2)\cdot 5(C_6H_5NO_2)\}_n$ (**5**). It is important to note that the crystal system remains in the monoclinic family, however the space group changes from $C2/c$ to $P2_1/c$ when going from **4** to **5**. Moreover, careful analysis of the crystal structure reveals that there are approximately four I_2 molecules per unit cell, resulting in an iodine content of roughly 6.3 % through exclusion of the iodine that belongs to the framework. With an increase in the iodine content, we conversely observe a drastic decrease in the amount of nitrobenzene molecules from 44 to 20 per unit cell, going from **4** to **5**.

Consequently, the available space in the voids increases from 1.1% to approximately 22.4% clearly representing **5** as an intermediate structure, where full guest exchange between nitrobenzene and I_2 has not yet been completed. This exchange process, where the nitrobenzene molecules are readily replaced by the encroaching I_2, provides evidence that the interactions formed by the I_2 species are more favorable than the π–π stacking interactions of the nitrobenzene guests. Careful analysis of the crystal structure of **5** reveals that the I_2 molecule (I13 and I14) is intercalated between two iodide atoms (I8 and I12) originating from the ZnI_2 fragments of the host structure. In order to provide molecular insights into the nature of the I_2 binding properties in **5**, we employed dispersion corrected periodic DFT calculations. All attempts to locate a minimum energy structure for **5** resulted in the alignment of the I_2 guests towards the terminal I^- ions, effectively forming an $[I_4]^{2-}$ unit in an almost identical fashion to the crystallographic data (Figure 26).

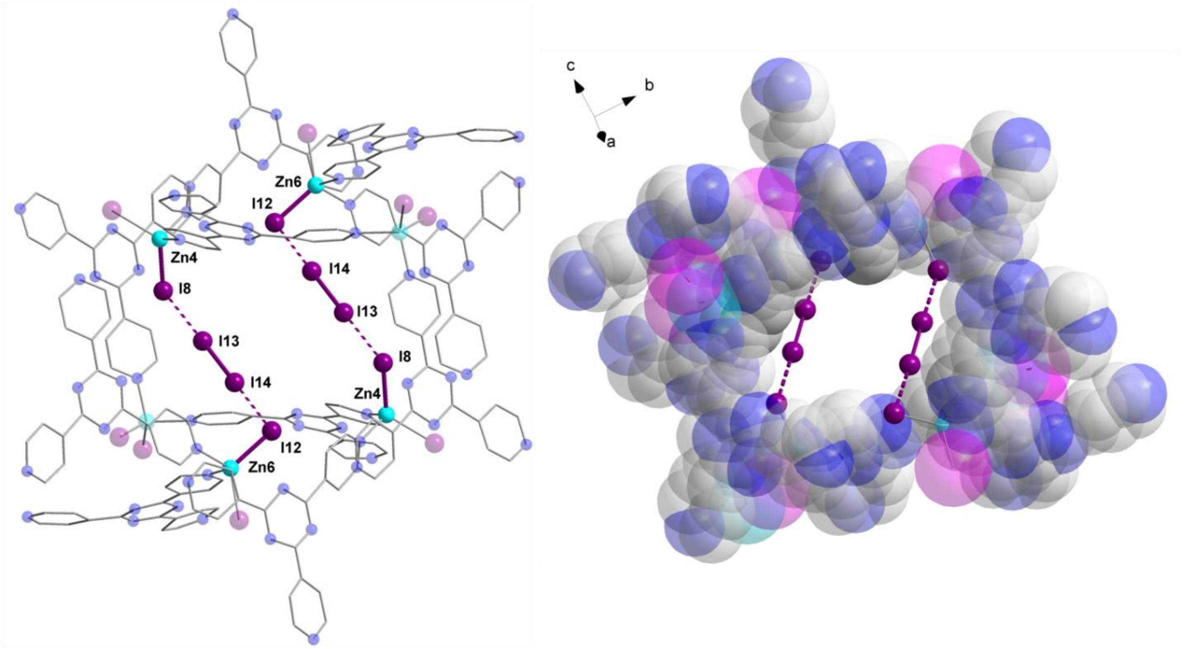

Figure 26: Stick and space-filling model of a partially labeled molecular fragment of **5** emphasizing the I_2 guest which forms strong halogen-halogen interactions with the iodide ions of the framework, effectively forming an $[I_4]^{2-}$ unit. Color code: purple (I), cyan (Zn), gray (C), blue (N). Hydrogen atoms are omitted for clarity.

In fact, the purposeful alignment of the I_2 guests perpendicularly to the iodide moieties resulted in their reorientation towards the I^- groups, even when the latter were allowed to fully relax. The DFT-derived I_2 binding energy was calculated to be 26.2 kcal/mol per I_2 guest. Moreover, the covalency of the $I^- \cdots I_2$ interactions were investigated by calculation of the Wiberg bond orders (Appendix C). The dual end-on bridging interaction of the I_2 guests with the terminal iodides of the framework gave bond orders of 0.22 and 0.26, for I12–I14 and I8–I13, respectively. For comparison, I13–I14 has a bond order of 0.79. These results, combined with DFT-derived bonding energies, indicate strong halogen-halogen interactions between the I_2 guest and I8 and I12. This type of M–I–I–I–I–M linkage has been previously reported in a handful of discrete compounds and polymeric chains,[13] however it represents the first MOF structure containing this type of unusual bridging unit. The $[I_4]^{2-}$ fragment is approximately linear with the largest deviation coming from the I12–I14–I13 angle (~172.8°). Furthermore, the central iodine distance of 2.76 Å between I13 and I14 is significantly shorter than the $I^- \cdots I_2$ distances of 3.47 and 3.51 Å for I8–I13 and I12–I14, respectively, as is commonly observed for $[I_4]^{2-}$ bridges (Table 5).[13]

Table 5: Assignment, occupancy and bond distances of iodine guests in compound **5**.

Iodine guest	**Occupancy**	**Assignment**	**Bond distances**
I13–I14	1	I_2 (I8···I13–I14···I12) Strongly halogen bonded	I8–I13: 3.47 Å I13–I14: 2.76 Å I14–I12: 3.51 Å

To further investigate the exchange of nitrobenzene for I_2 guests, DFT calculations were performed to support the crystallographic evidence. These results revealed that the formation of the $[I_4]^{2-}$ unit is more energetically favorable than an equivalent structure containing nitrobenzene, with binding energies of 26.2 kcal/mol per I_2 guest for **5**, compared to an energy of 9.2 kcal/mol per nitrobenzene for the as-synthesized MOF, **4**.

The capture of I_2 in the host framework, **4**, makes for a particularly intriguing study due to the possibility of two competing adsorption processes; that of physisorption and chemisorption. By systematically observing the single-crystal to single-crystal transformations over a short period of time, it is possible to visualize both the stepwise changes in the structure of the host framework and the manner by which iodine is incorporated. An important feature of the coordination network, **4**, is the orientation of the terminal iodide ions towards the microporous channels, thereby encouraging favorable interactions with the iodine guests. Interestingly, the I_2 guest molecule in **5** exhibits full occupancy in the host framework and is a clear indicator that the preferential arrangement of initial I_2 molecules is between two terminal and exposed μ_1–I ions (Figure 27).

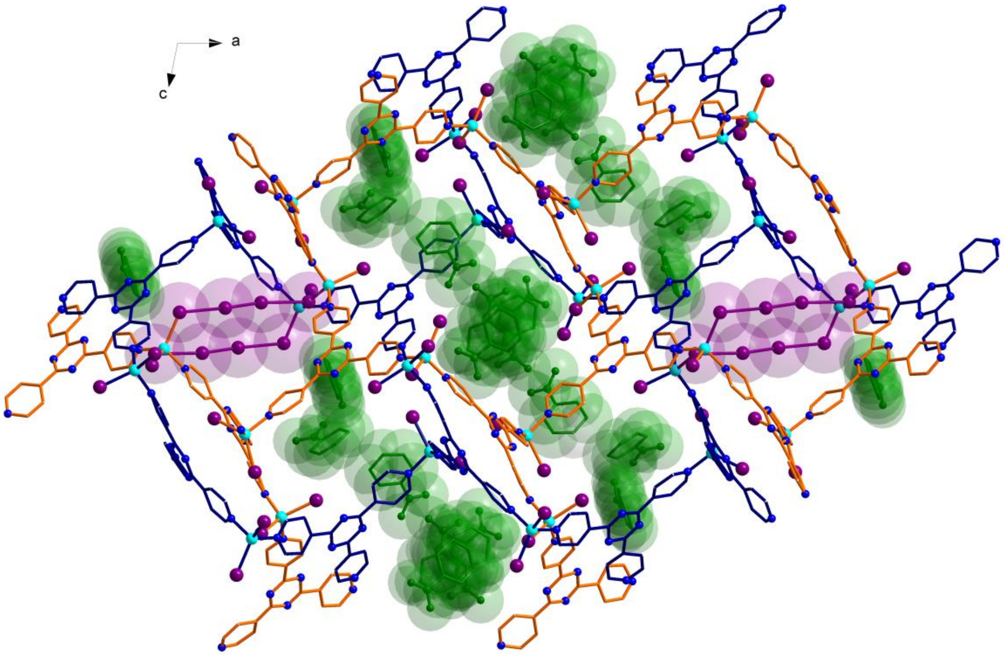

Figure 27: Packing arrangement of **5** along the *b*-axis. The two interpenetrated networks are shown in blue and orange, while the nitrobenzene and iodine guest molecules are shown in green and purple, respectively. Hydrogen atoms are omitted for clarity.

This behavior follows the general tendencies of adsorption where the formation of strong interactions or bonds makes chemisorption more energetically favorable than physisorption, even if structural distortions of the host framework are induced. In fact, the formation of the $[I_4]^{2-}$ unit results in a slight reduction of the unit cell volume (Table 4). We can therefore speculate that this new bridging unit effectively brings the doubly-interpenetrated networks closer together and partitions the pore space, as permitted by the flexibility of the framework.

3.3.3 Second structural intermediate

The same iodine vapor diffusion strategy was employed to obtain the second intermediate structure $\{[(ZnI_2)_6(TPT)_4]\cdot 1.69(I_2)\cdot 3(C_6H_5NO_2)\}_n$ (**6**), after 6 h of exposure time to the I_2 vapors. The dark brown crystals retained crystallinity and yielded more electron density within the channels of the MOF. X-ray crystallography reveals that **6** also crystallizes in the lower symmetry $P2_1/c$ space group, due to the incorporation of I_2 guests (Table 4). The host framework maintains the structural architecture of **4**, however, we can observe a further decrease in the unit cell volume going from **5** to **6**. As previously mentioned, this behavior may be explained by the flexible nature of the framework, where the incorporation of I_2 molecules would induce small structural rearrangements to accommodate the new guests. In turn, this will reduce the overall energy of the system and promote favorable guest-host interactions.

The encapsulation of additional I_2 guests when going from **5** to **6** is accompanied by a further reduction in nitrobenzene solvent molecules, down from 20 to 12 molecules per unit cell following 6 h of exposure time to I_2 vapors. Accordingly, the iodine guest content increased from 6.3% to 10.8%, having approximately 6.8 I_2 molecules per unit cell. This drastic increase in merely 3 h of additional exposure time emphasizes the potential of this framework for the rapid capture and sequestration of I_2. Close inspection of the crystal structure of **6** reveals the presence of the same $[I_4]^{2-}$ unit that was observed in **5**, unequivocally confirming the strength of the $I^- \cdots I_2$ halogen bonds. In the present case, the $I^- \cdots I_2$ distances are 3.43 and 3.44 Å for I8–I19 and I10–I20, respectively, while the central iodine distance is 2.75 Å (Table 6), which are well within the previously observed ranges for an $[I_4]^{2-}$ unit.[13]

Table 6: Assignment, occupancy and bond distances of iodine guests in compound **6**.

Iodine guest	**Occupancy**	**Assignment**	**Bond distances**
I13–I14	0.11	I_3^- (I1–I13–I14)	I1–I13: 3.26 Å I13–I14: 2.71 Å
I15–I16	0.11	I_3^- (I4–I15–I16)	I4–I15: 3.05 Å I15–I16: 2.72 Å
I17–I18	0.18	I_3^- (I7–I17–I18)	I7–I17: 2.96 Å I17-I18: 2.71 Å
I19–I20	0.88	I_2 (I8···I19–I20···I10) Strongly halogen bonded	I8–I19: 3.43 Å I19–I20: 2.75 Å I20–I10: 3.44 Å
I21–I22	0.12	I_3^- (I8–I21–I22)	I8–I21: 2.52 Å I21–I22: 2.77 Å
I23	0.12	I_2 (I10···I23–I23···I10) Weakly halogen bonded	I23–I23: 2.54 Å I10–I23: 4.02 Å
I24–I25	0.10	I_2 (I24–I25)	I24–I25: 2.73 Å
I26–I27	0.13	I_2 (I26–I27)	I26–I27: 2.71 Å

The longer exposure time to I_2 vapors is accompanied by a significant increase in electron density assigned to partially occupied iodine species. More precisely, there are four individually refined I_2 molecules that have been chemisorbed within the framework, leading to the formation of I_3^- groups. Two such groups are locating within the same pore (I17–I18 and I21–I22 of Figure 28), on which DFT-derived binding energies were calculated to confirm the chemisorptive process. The $I^- \cdots I_2$ interaction has a binding energy of approximately 20 kcal/mol, testifying to the covalent nature of these adsorption sites (Appendix D). Additionally, we investigated the bond orders of the same $I^{-}\cdots I_2$ interactions. This analysis yielded values ranging from 0.45 to 0.48, corroborating the previous assessment of chemisorption. It is noteworthy that these values are nearly double that of the values obtained for the $[I_4]^{2-}$ unit and attest to the more covalent nature of the interactions. (Appendix D).

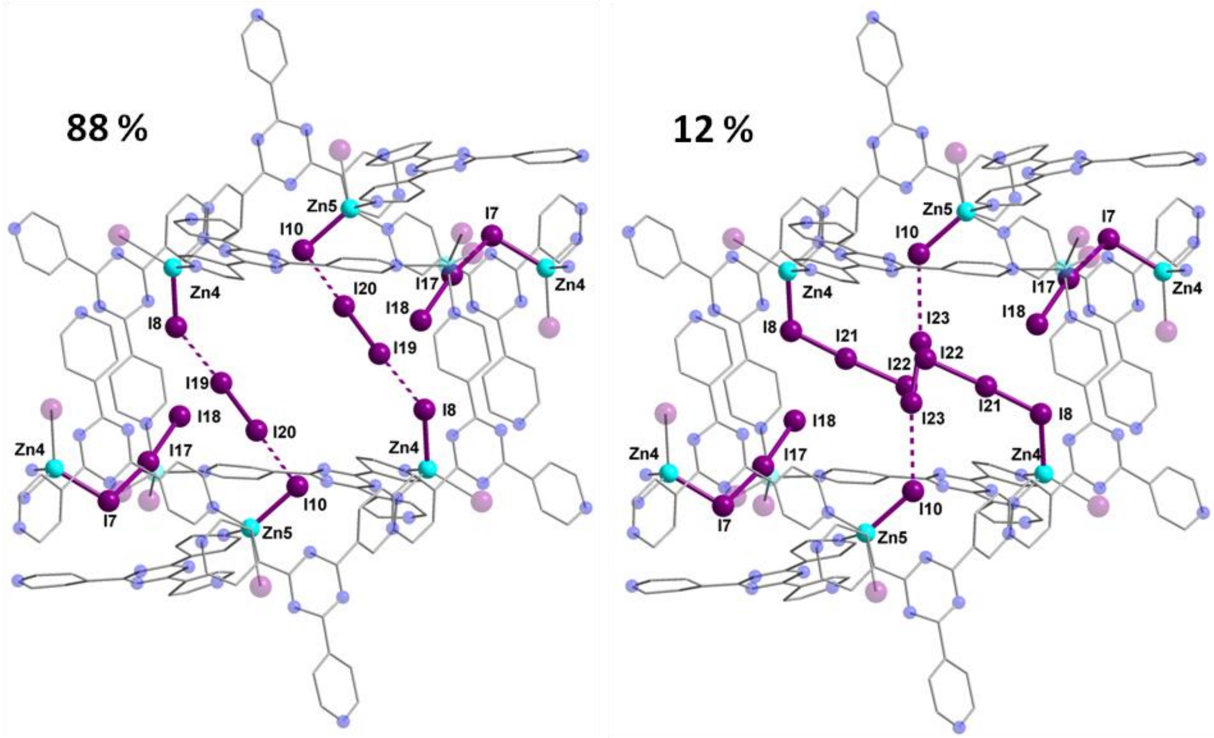

Figure 28: Molecular structure of a single pore of **6**, illustrating the disordered and partially occupied I_2 guests. In the 88% occupancy case, there is the same $[I_4]^{2-}$ unit as in **5** (left), while in the 12% occupancy instance there is a chemisorbed I_3^{-} group along with an I_2 molecule participating in weak halogen bonding (right).

The occupancy of the I_3^{-} groups range from 0.11 to 0.18, depicting **6** as an intermediate structure, where the maximal iodine uptake capacity of the MOF has not yet been attained. It is worth noting that the I_2 molecule forming the $[I_4]^{2-}$ unit (I19–I20) exhibits the highest occupancy of all encapsulated I_2 guests for **6**, with a value of 0.88 (Table 6). This I_2 unit is disordered over two positions, resulting in an especially strong covalent bond with I8 to form an I_3^{-} group. This second position can be identified as I21–I22, where the $I^{-}\cdots I_2$ distance is 2.52 Å, the shortest reported for an end-on bonded I_2 unit. This is likely due to the fact that the $[I_4]^{2-}$ bridge is reoriented in order to provide additional spacing for I_2 molecules, in the form of I_3^- (I21–I22) and I_2 (I23–I23) (Figure 28). It is interesting to note that the latter I_2 molecule is stabilized by two terminal iodide ions (I10) and forms an $[I_4]^{2-}$ unit through an elongated I10–I23 distance of 4.02 Å, giving weak halogen-halogen interactions. Further insights into the mechanism of iodine uptake can be obtained by calculating the difference in binding energy of the 12% configuration from the 88% configuration. (Figure 28).

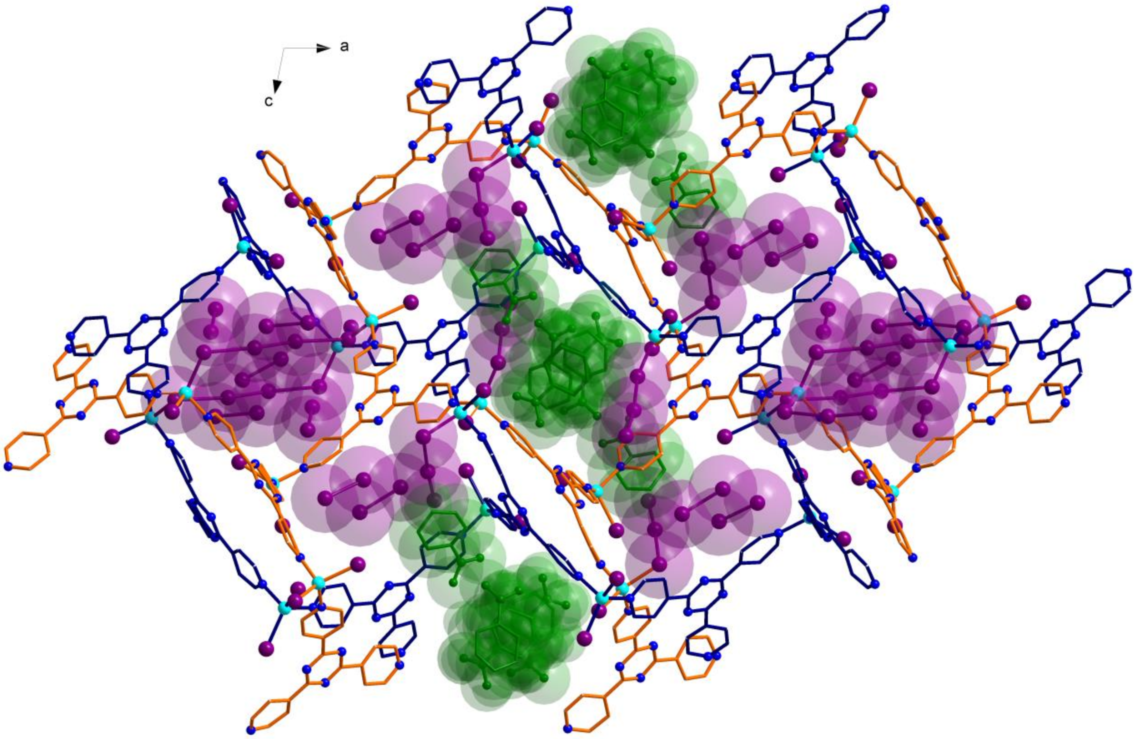

Figure 29: Packing arrangement of **6** along the *b*-axis. The two interpenetrated networks are shown in blue and orange, while the nitrobenzene and iodine guest molecules are shown in green and purple, respectively. Hydrogen atoms are omitted for clarity.

Due to an uneven number of I_2 guests between the two configurations, the energy of one additional I_2 molecule was added to the 88% configuration to permit reasonable quantitative comparisons. The resulting reaction energy, obtained by DFT, was calculated to be –9 kcal/mol. This value suggest that larger uptakes in I_2 are energetically favorable and that the $[I_4]^{2-}$ unit, which participates in strong halogen-halogen interactions, is relocated to accommodate an increasing number of I_2 molecules. These findings display the advantages of combining crystallographic evidence with computational methods for visualizing the motion of gaseous substrates in porous crystals. The other I_3^- ions give reasonable geometrical parameters with $I^-\cdots I_2$ distances ranging from 2.96 to 3.26 Å, and I–I–I angles between 169.4 and 176.6°. In addition to chemisorbed I_2, compound **3** contains three partially occupied physisorbed I_2 molecules, providing direct structural evidence that both processes of adsorption occur within the host framework (Figure 29).

The participation of both physisorption and chemisorption in the uptake of gaseous guests is a fascinating feature of the MOF, since chemisorption is generally associated with frameworks exhibiting open metal sites that can bind gas molecules.[14] Interestingly, the iodine guests are preferentially bonded to terminal I^- ions rather than the coordinatively unsaturated tetrahedral Zn atoms. This illustrates the optimization potential of MOFs, where chemisorption can be obtained without open metal sites, leading to higher chemical stabilities. The role of the terminal halide ion on the chemisorption of I_2 is currently under investigation.

3.3.4 Third structural intermediate

Following multiple attempts to measure the SCXRD data of **4** saturated with I_2 it was determined that 15 h of exposure time to I_2 vapors was the limit for retaining adequate crystallinity. Hence, we present the single crystal structure of **7**, $\{[(ZnI_2)_6(TPT)_4]\cdot 4.65(I_2)\}_n$, with the best of our refinement methods, where any further I_2 uptake would disallow the use of conventional crystallographic techniques. Intermediate **7** was refined in the monoclinic $P2/n$ space group and further continues the trend of decreasing unit cell volumes with I_2 uptake, reflecting the flexible nature of the MOF. It is important to note that while the agreement factors of the refinement are high, the crystal structure of **7** provides invaluable structural insights regarding the encapsulation of I_2. Moreover, there are no unassigned residual electron density peaks, testifying to the completeness of the guest assignment. Notably, we can observe the absence of nitrobenzene solvent molecules and their exclusive replacement by I_2. The unit cell now comprises approximately 18.6 I_2 guest molecules, a radical increase of roughly 274% going from **6** to **7**. Thus, the iodine guest content is ~37.3 %, and correspondingly, 1 g of the empty framework, **1** can uptake around 0.59 g of I_2 after 15 h which is similar in value to other porous MOFs.[15] These results are in good agreement with the TGA measurements performed on single crystals of **7** giving an iodine guest content of 39.8 % and an uptake of I_2 of 0.66 g/g (Figure 30).

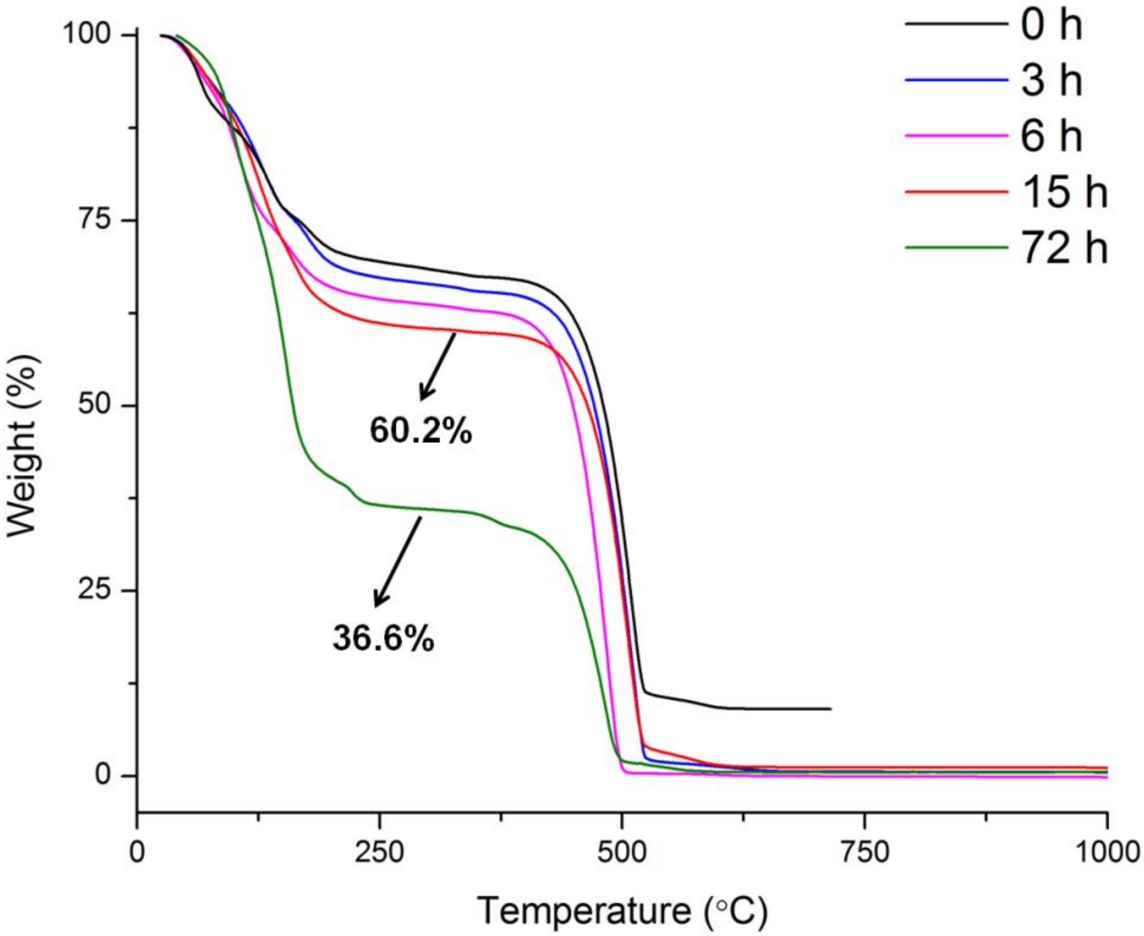

Figure 30: The thermogravimetric analyses (TGA) were carried out between 25–715 °C for **4** and between 25–1000 °C for **5–7** and for single crystals of **4** after 72 h of exposure to I_2. Measurements were performed under nitrogen atmosphere (25 mL/min).

This drastic increase in I_2 inclusion from merely a few additional hours of I_2 vapor exposure results in a significant distortion of the MOF framework (Figure 31). We can surmise that these distortions, which allow for a greater intake of I_2, are a contributing factor in the loss of crystallinity of the single crystals. The connectivity of the framework remains the same, however the pyridine moieties, as well as the central triazines of the TPT ligand, are less planar and adopt a more twisted conformation as evidenced by the large thermal parameters. We can hypothesize that these groups exhibit some freedom of rotation, therefore permitting the entry and accommodation of a larger number of I_2 guests within the same pore or channel.

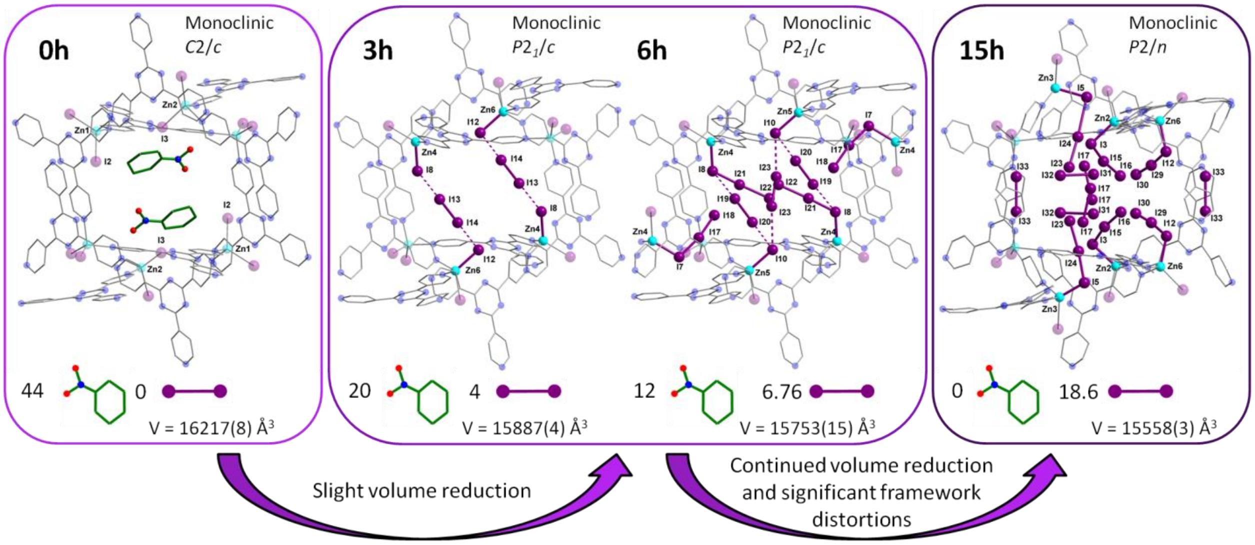

Figure 31: X-ray crystal structure of a single pore of **4** viewed along its channel direction. Evolution of the guests, where nitrobenzene solvent molecules are sequentially exchanged for iodide species, are illustrated for the same pore following 3, 6 and 15 h of exposure time to I_2 vapors. The amount of guest molecules contained per unit cell are listed, along with changes in the space group and unit cell volumes for compounds **4–7**.

The structural analysis of **7** reveals that the $[I_4]^{2-}$ unit found in **5** and **6** has been replaced with several partially occupied physisorbed and chemisorbed I_2 molecules, also supporting the previous assessment of reorienting the $[I_4]^{2-}$ unit to accommodate a larger number of I_2 guests.

While **6** displayed a significant increase in electron density assigned to I_2, their occupancies remained relatively low, whereas **7** sees the incorporation of an even larger amount of I_2 combined with higher occupancies (Table 7).

Table 7: Assignment, occupancy and bond distances of iodine guests in compound **7**.

Iodine guest	**Occupancy**	**Assignment**	**Bond distances**
I13–I14	0.8	I_3^- (I9–I14–I13)	I9–I14: 3.47 Å I14–I13: 2.76 Å
I15–I16	0.5	I_3^- (I3–I15–I16)	I3–I15: 3.17 Å I15–I16: 2.71 Å
I17	0.3	I_2 (I17–I17)	I17–I17: 2.75 Å
I18	0.15	I_2 (I18–I18)	I18–I18: 2.85 Å
I19–I20	0.3	I_3^- (I8–I19–I20)	I8–I19: 3.33 Å I8’–I19: 3.21 Å I19–I20: 2.69 Å
I21–I22	0.3	I_3^- (I4–I22–I21)	I4–I22: 3.41 Å I21–I22: 2.72 Å
I23–I24	0.45	I_3^- (I5–I24–I23)	I5–I24: 2.85 Å I24–I23: 2.71 Å
I25–I26	0.55	I_2 (I6···I26–I25···I11) Weakly halogen bonded	I6–I26: 3.73 Å I26–I25: 2.74 Å I25–I11: 3.31 Å
I27–I28	0.5 (I27) 0.25 (I28)	I_3^- (I10–I27–I28) I_3^- (I10–I27–I28’)	I10–I27: 3.26 Å I27–I28: 2.66 Å I27–I28’: 2.92 Å
I29–I30	0.3	I_3^- (I12–I29–I30)	I12–I29: 3.15 Å I29–I30: 2.71 Å
I31–I32	0.35	I_2 (I31–I32)	I31–I32: 2.75 Å
I33–I33	0.75	I_2 (I33–I33)	I33–I33: 2.79 Å

The I_2 guest forming the $[I_4]^{2-}$ unit displays $I^-\cdots I_2$ distances of 3.31 and 3.73 Å, leading to halogen-halogen interactions with the terminal iodide of the framework (Figure 32, pore A). The orientation of the guest along the two terminal I^- ions strongly suggests the formation of the M–I–I–I–I–M linkage, in similar fashion to the $[I_4]^{2-}$ unit described in **5**. Furthermore, the I_2 molecule with the highest occupancy is I13–I14 with a value of 0.8, and forms a chemisorbed I_3^- group. This guest is observed alongside two other I_3^- moieties and one physisorbed I_2 in the same pore (Figure 32, pore B). It is worthwhile to mention that I27–I28 guest which forms an I_3^- group with I10 undergoes a precession movement, leading to a disordered I28 atom. To complete the analysis of the guests, pores C and D demonstrate similar I_2 guest uptake behaviors with an additional 4 chemisorbed and 3 physisorbed I_2 molecules. It is remarkable that even with the inclusion of all these I_2 molecules, **7** still exhibits an appreciable 18.4% void space volume, confirming this structure as an intermediate towards the complete saturation of I_2.

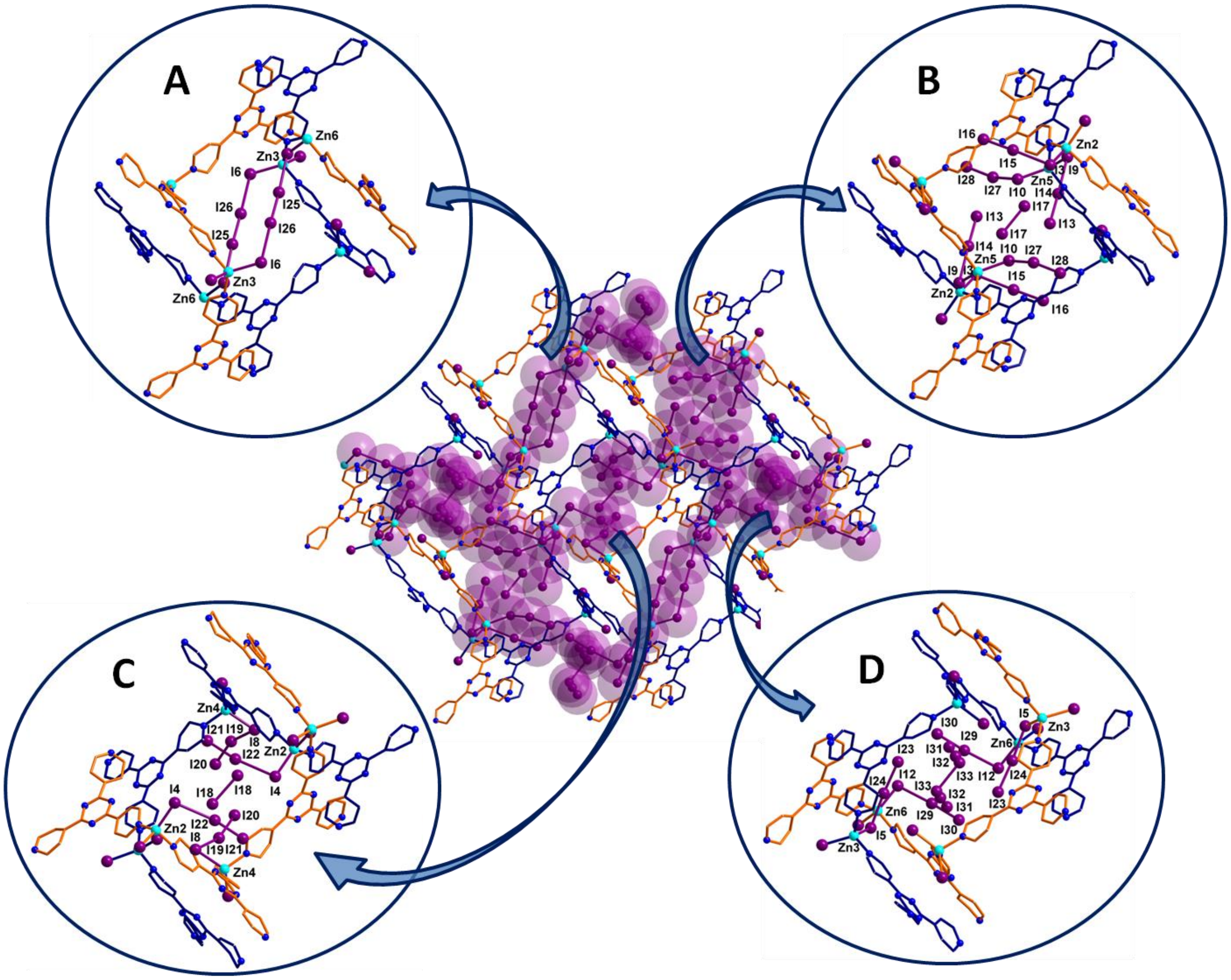

Figure 32: Packing diagram of **7** along the *b*-axis, illustrating the two interpenetrating networks in blue and orange along with the four different pores (listed A to D) and their respective iodine guests shown in purple.

This was further confirmed by the TGA curve of a sample of **4** exposed to I_2 vapors over a period of 72 h, giving a weight loss of ~63.4% (Figure 30). Hence, **4** has the potential of loading an excess of 1.73 g of I_2 per 1 g of MOF, making it an exceptional material for the capture of iodine. In fact, this value represents the second highest I_2 uptake in MOFs, just behind Cu-BTC with exhibits an uptake of 1.75 g/g which was measured at a higher temperature of 350 K compared to the room temperature value of 1.73 g/g for **4**.[16] Overall, it is the seventh highest reported adsorbent capacity for I_2 behind mainly PAFs (porous aromatic frameworks) whose values extend up to 2.76 g/g at 350 K.[17]

The experimental I_2 uptake capacity is in accordance with the calculated value of 1.67 g/g obtained by using available space in the voids and the density of I_2 (Appendix E). This enormous uptake of I_2 can be attributed to a number of factors, including favorable guest–host interactions, framework flexibility, and high porosity (60 %). More specifically, **4** offers strong sites of adsorption for I_2 through the terminal iodide ions of the framework as well as favorable π-halogen interactions with the TPT ligand.

3.3.5 Diffuse reflectance spectroscopy analysis

In order to probe the release kinetics of iodine, we performed time-dependent diffuse reflectance spectroscopy (DRS) measurements on compound **4** once it was completely saturated by I_2. The Kubelka-Munk spectra of TPT, ZnI_2, I_2 and **4** were first collected to examine the origin of the bands (Appendix F). Afterwards, single crystals of **4**, saturated with I_2, were measured through DRS over a period of 120 h at ambient conditions (Figure 33). The time-lapsed Kubelka-Munk spectra reveals that stabilization of the compound occurs after approximately four days. This stabilized compound exhibits similar electronic transitions as **4** saturated with I_2, providing strong evidence that iodine remains a major component of the MOF. In principle, we can envision that the more weakly encapsulated I_2 guests (i.e physisorbed) are more susceptible of being evacuated, while the chemisorbed iodide molecules would remain part of the framework and require harsher conditions for their removal. Detailed examination of the time-dependent DRS measurements shows a decrease in the intensity of the bands in the UV region, combined with an increase in the intensity and a blue-shift of the shoulders in the visible range. This may be explained by the intermolecular interactions of the I_2 molecules.

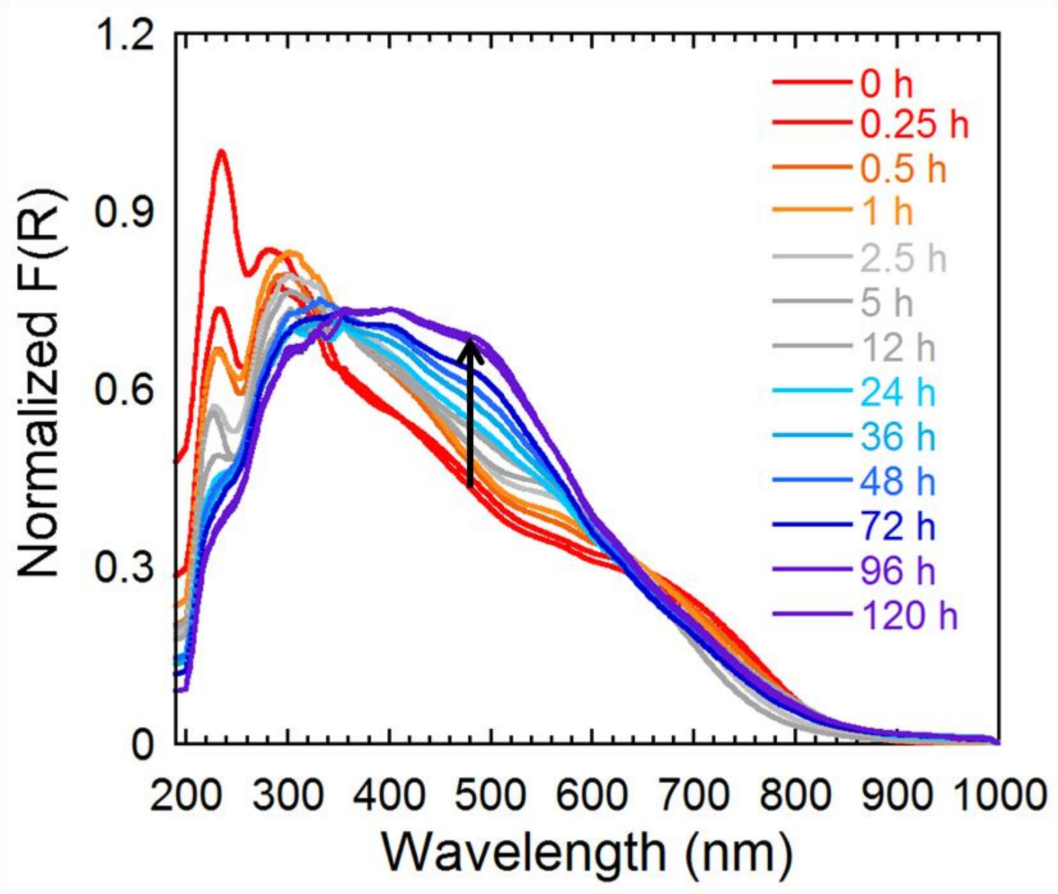

Figure 33: Normalized Kubelka-Munk spectra of **4** saturated with I_2 followed over time at ambient conditions for a period of 120 h.

The stabilized compound (after 96 h), is weakly diffracting, and therefore, cannot be examined by conventional crystallographic methods. Consequently, this compound was investigated by FTIR, revealing intense and broad bands at approximately 670, 1640 and 3350 cm^{-1}, which is characteristic of the vibrations for H_2O (Figure 34). Thus, if **4** is saturated by I_2 and subsequently stored at ambient conditions, we can expect evaporation of the physisorbed I_2 followed by incorporation of water molecules. The DRS results demonstrate the potential of **4** for the irreversible capture of radioactive I_2, through a number of strong chemisorption sites.

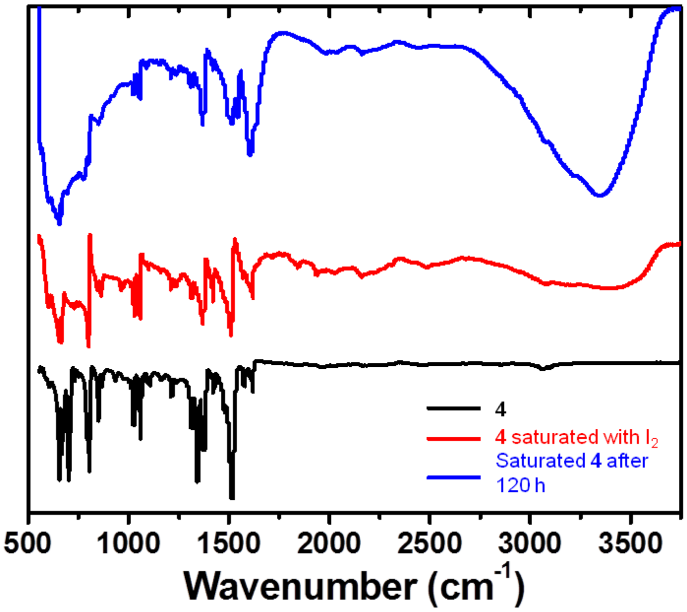

Figure 34: FTIR spectra of **4** (black), **4** completely saturated by I_2 (red) and **4** saturated by I_2 and left at ambient conditions for 120 h (blue).

3.4 Conclusion

In summary, we have demonstrated the stepwise uptake of I_2 within a highly porous MOF, using SCXRD (Figure 35). This methodology allows key insights into the process by which the gaseous guests are systematically incorporated in the cavities of a high performing MOF. Furthermore, the exceptional changes in the framework display the breathability of the MOF in regards to accommodation of guest molecules. This feature is often sought after for the design of novel dynamic materials that are well-suited for adsorption-desorption processes. In this work, the flexible nature of the MOF was a main contributing factor in retaining adequate crystallinity for the single crystal experiments. Fundamental research into the dynamics and site selection of gaseous substrates is a leading approach towards the improvement of gas capture materials. This study clearly demonstrated that stepwise X-ray experiments are an effective strategy towards the identification of key adsorption sites and the interactions therein, enabling the rational design of capture materials.

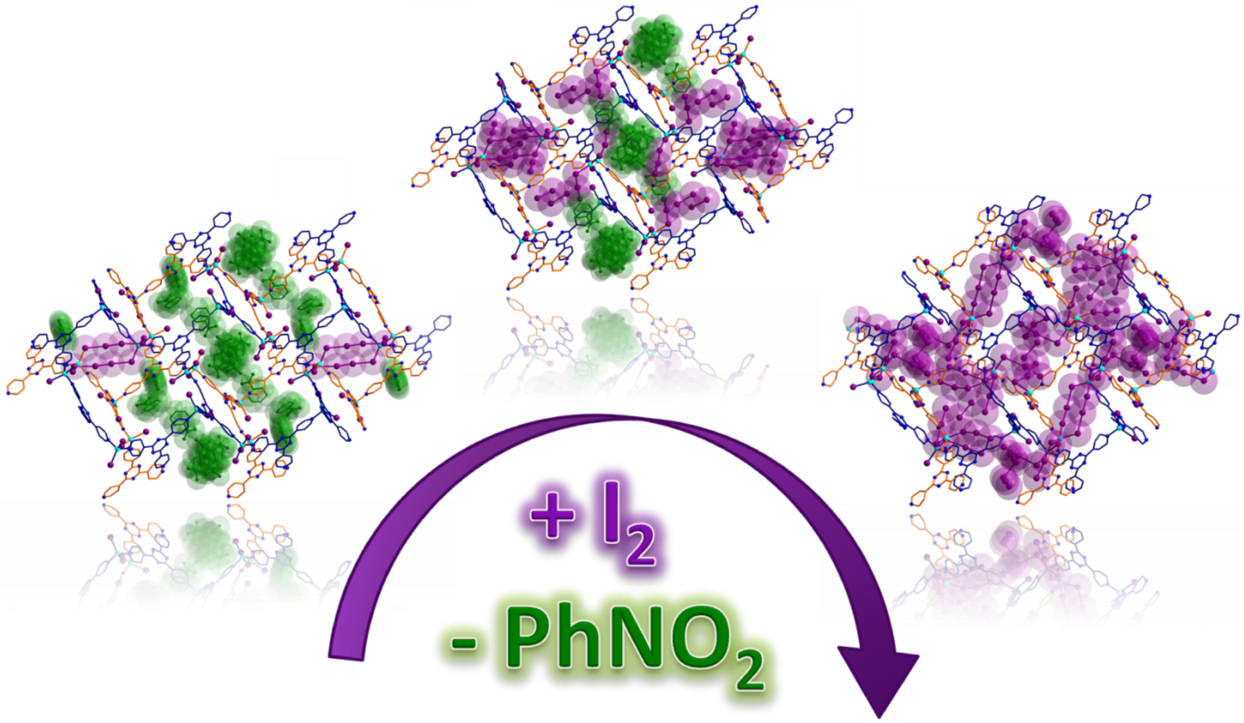

Figure 35: Schematic diagram demonstrating the stepwise crystallographic process employed for investigating the uptake of molecular iodine in compound **4**.

3.5 References

[1] Inokuma, Y.; Yoshioka, S.; Ariyoshi, J.; Arai, T.; Hitora, Y.; Takada, K.; Matsunaga, S.; Rissanen, K.; Fujita, M. *Nature* **2013**, *495*, 461.

[2] Biradha, K.; M. Fujita, *Angew. Chem. Int. Ed.* **2002**, *41*, 3392.

[3] *Statistical Review of World Energy 2015,* BP, http://www.bp.com.

[4] *Nuclear Power in the World Today*, World Nuclear Association, http://www.world-nuclear.org.

[5] Hou, X.; Malencheko, A. F.; Kucera, J.; Dahlgaard, H.; Nielson, S. P. *Sci. Tot. Environ.* **2003**, *302*, 63.

[6] Chapman, K. W.; Chupas, P. J.; Nenoff, T. M. *J. Am. Chem. Soc.* **2010**, *132*, 8897.

[7] Sava, D. F.; Rodriguez, M. A.; Chapman, K. W.; Chupas, P. J.; Greathouse, J. A.; Crozier, P. S.; Nenoff, T. M. *J. Am. Chem. Soc.* **2011**, *133*, 12398.

[8] (a) Yang, C.; Wang, X.; Omary, M. A. *Angew. Chem.* **2009**, *121*, 2538. (b) Vaidhyanathan, R.; Iremonger, S. S.; Shimizu, G. K. H.; Boyd, P. G.; Alavi, S.; Woo, T. W. *Science* **2010**, *330*, 650. (c) Zhou, H.-L.; Lin, R.-B.; He, C.-T.; Zhang, Y.-B.; Feng, N.; Wang, Q.; Deng, F.; Zhang, J.-P.; Chen, X.-M. *Nat. Commun.* **2013**, *4*, 1.

[9] Richardson, R. D.; Wirth, T. *Angew. Chem. Int. Ed.* **2006**, *45*, 4402.

[10] (a) Kojima, T.; Choi, W.; Kawano, M. *Chem. Commun.* **2014**, *50*, 13793. (b) Martí-Rujas, J.; Islam, N.; Hashizume, D.; Izumi, F.; Fujita, M.; Kawano, M. *J. Am. Chem. Soc.* **2011**, *133*, 5853.

[11] Li, M.-X.; Miao, Z.-X.; Shao, M.; Liang, S.-W.; Zhu, S.-R. *Inorg. Chem*. **2008**, *47*, 4481.

[12] Inokuma, Y.; Yoshioka, S.; Ariyoshi, J; Arai, T.; Fujita, M. *Nat. Protoc.* **2014**, *9*, 246.

[13] (a) Hewison, L.; Crook, S. H.; Mann, B. E.; Meijer, A. J. H. M.; Adams, H.; Sawle, P.; Motterlini, R. A. *Organometallics* **2012**, *31*, 5823. (b) Masuhara, N.; Nakashima, S.; Yamada, K. *Chem. Lett.* **2005**, *34*, 1352. (c) Le Bras, J.; Amouri, H.; Vaissermann, J. *Inorg. Chem.* **1998**, *37*, 5056.

[14] (a) Wu, H.; Zhou, W.; Yildirim, T. *J. Am. Chem. Soc.* **2009**, *131*, 4995. (b) McKinlay, A. C.; Xiao, B.; Wragg, D. S.; Wheatley, P. S.; Megson, I. L.; Morris, R. E. *J. Am. Chem. Soc.* **2008**, *130*, 10440. (c) Britt, D.; Tranchemontagne, D.; Yaghi, O. M. *PNAS* **2008**, *105*, 11623. (d) Bloch, E. D.; Queen, W. L.; Krishna, R.; Zadrozny, J.; Brown, C. M.; Long, J. R. *Science* **2012**, *335*, 1606. (e) Horike, S.; Dincă, M.; Tamaki, K.; Long, J. R. *J. Am. Chem. Soc.* **2008**, *130,* 5854.

[15] (a) Liu, Q.-K.; Ma, J.-P.; Dong, Y.-B. *Chem. Commun.* **2011**, *47*, 7185. (b) Zeng, M.-H.; Wang, Q.-X.; Tan, Y.-X.; Hu, S.; Zhao, H.-X.; Long, L.-S.; Kurmoo, M. *J. Am. Chem. Soc.* **2010**, *132*, 2561. (c) Zhang, Z.-J.; Shi, W.; Niu, Z.; Li, H.-H.; Zhao, B.; Cheng, P.; Liao, D.-Z.; Yan, S.-P. *Chem. Commun.* **2011**, *47*, 6425.

[16] Sava, D. F.; Chapman, K. W.; Rodriguez, M. A.; Greathouse, J. A.; Crozier, P. S.; Zhao, H. Y.; Chupas, P. J.; Nenoff, T. M. *Chem. Mater.* **2013**, *25*, 2591.

[17] Yan, Z.; Yuan, Y.; Tian, Y.; Zhang, D.; Zhu, G. Angew. Chem. Int. Ed. 2015, 54, DOI: 10.1002/anie.201503362.

Chapter 4

Metallocene and Organic Guest Inclusion in a Porous Coordination Network as Evidenced by the Crystalline Sponge Method for X-ray Analysis

Abstract

A channeled structured MOF was selected as the host for the inclusion of a number of metallocene compounds. The adsorbate structures of ferrocene and ferrocene carboxaldehyde were obtained from single-crystal X-ray diffraction using the crystalline sponge method. The packing and orientation of the organometallic guests is investigated, along with the influence of the aldehyde group on the guest-host interactions. The same strategy was also applied to a number of interesting organic guests with potential for further reactivity illustrating the efficacy of the up-and-coming crystalline sponge method. The present chapter aims to provide solid grounds for future works in terms of organometallic guest inclusion and reactivity inside the pores or channels of a MOF.

4.1 Introduction

Over the past two decades, the scientific community has witnessed an unprecedented development in a new class of crystalline materials capable of offering easily tunable porous structures. These solid-state materials, termed metal-organic frameworks (MOFs), can be designed by combining inorganic nodes (metal ions or clusters) with organic spacers leading to predictable molecular assemblies. Numerous highly porous MOF materials have been prepared which exhibit guest selectivity leading to exciting applications in gas separation,[1] catalysis,[2] drug delivery,[3] chemical sensing,[4] and crystallography.[5] Inherently, these application deal with the interactions between the host structure and the adsorbate (guest) molecules. Consequently, we became interested in examining the potential of incorporating magnetically relevant molecules inside the pores or channels of a MOF, and evaluating the impact of the host on the magnetic properties. The host-guest chemistry of MOFs loaded with organometallic molecules is scarcely reported,[6] however ferrocene appears to be a suitable molecular probe for potential organometallic guest inclusion.[7] While the loading of such guests can be confirmed by spectroscopic methods or by powder X-ray diffraction, an in-depth understanding of the guest-host interactions can only be truly achieved through single-crystal X-ray diffraction. Hence, our research efforts were directed towards the inclusion of ferrocene and its derivatives using the "crystalline sponge method" introduced by Fujita and co-workers,[5] which has seen some success in crystallographically identifying guest compounds. The selected crystalline sponge is synthesized by the slow diffusion of a solution of zinc iodide and tris(4-pyridyl)-1,3,5-triazine (TPT), leading to a doubly-intepenetrated network. Despite interpenetration, the selected MOF maintains high porosity and displays an inherent affinity for organic molecules, due to the availability of π–π and charge transfer interactions with the TPT ligand. Therefore, the process for guest selection also involved small organic molecules containing π electrons, thus permitting favorable interactions with the host structure. In order to put these results into perspective, a table summarizing metallocene inclusion in MOFs is presented in Table 8. It is clear from these results that obtaining adequate single-crystals of the inclusion compound is a significant challenge, with only one reported example to date. Herein, we present the single-crystal structures of two metallocene compounds imbedded in a porous MOF using a conventional laboratory diffractometer.

Table 8: Summary of metallocene uptake by MOFs.

MOF	Metallocene	Structural characterization method	Year
$[Cu_2(bdc)_2(dabco)]$[7c]	Ferrocene	PXRD, EA, EDX	2011
$[Cu_2(ndc)_2(dabco)]$[7c]	Ferrocene	PXRD, EA, EDX	2011
MOF-5[8]	Ferrocene	SCXRD (synchrotron radiation)	2006
MOF-5[8]	Ferrocene aldehyde	EA, ^{1}H-NMR	2006
MIL-47(V)[6b]	Cobaltocene	PXRD, FTIR	2010
MIL-47(V)[6b]	Ferrocene	PXRD, FTIR	2010
MIL-53(Al)[6b]	Ferrocene	PXRD, FTIR, ^{13}C–NMR	2010
MIL-53(Al)[6b]	1-formylferrocene	PXRD, FTIR	2010
MIL-53(Al)[6b]	1,1’-dimethylferrocene	PXRD, FTIR, ^{13}C–NMR	2010
MIL-53(Al)[6b]	1,1’-diformylferrocene	PXRD, FTIR, ^{13}C–NMR	2010
MIL-53(Al)[6b]	1,1’-diethylferrocene	PXRD, FTIR, ^{13}C–NMR	2010
MIL-53(Al)[6b]	Cobaltocene	PXRD, FTIR, ^{13}C–NMR	2010
$[Cu_4I_4\text{-}dabco_2]$[7b]	Ferrocene	CV, TGA, AAS	2013
$[Tb_{16}(tatb)_{16}]$[9]	Ferrocene	EA, ^{1}H-NMR	2007

*dabco: 1,4-diazabicyclo[2.2.2]octane, bdc: 1,4-benzene dicarboxylic acid, ndc: 1,4-naphtalene dicarboxylic acid, tatb: triazine-1,3,5-tribenzoic acid.

While the initial report of the crystalline sponge method by Fujita and co-workers gained a significant amount of interest in the scientific community,[5] difficulties pertaining to the quality of the crystallographic data has somewhat hindered further progress. As mentioned previously, this was highlighted by the incorrect stereochemical determination of miyakosyne A. Since then, very few research groups, other than Fujita’s, have displayed the utility of the crystalline sponge method. To the best of our knowledge, there have only been 3 compounds studied by this technique from research groups that are not affiliated with the innovators (Figure 36).[10] As a result, we wanted to contribute to the success of this method by demonstrating its applicability and reproducibility. Having previously demonstrated the incorporation of smaller molecules, such as iodine in a crystalline sponge, as was described in chapter 3, the present chapter focuses more closely on larger guests with dimensions nearing that of the pore size.

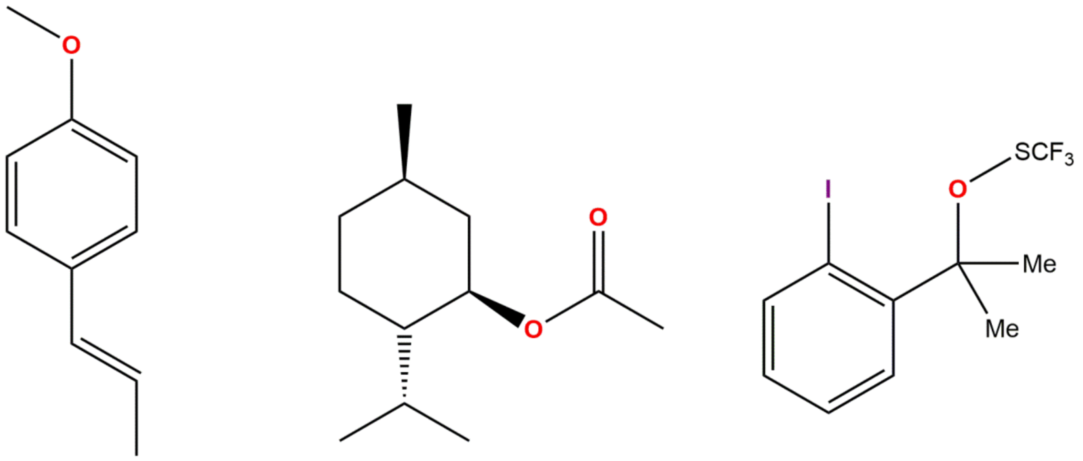

trans-anethole (1*R*)-(–)-menthyl acetate Trifluoromethylthiolation reagent

Figure 36: Compounds that were investigated using the crystalline sponge method, by groups other than the Fujita group.

4.2 Experimental section

4.2.1 Synthesis

The 2,4,6-tris(4-pyridyl)-1,3,5-triazine (TPT) ligand and the parent MOF, $\{[(ZnI_2)_3(TPT)_2]\cdot 5.5(C_6H_5NO_2)\}_n$, were synthesized according to previously reported methods.[11,12] The synthetic protocol of the TPT ligand is also described in the experimental section of Chapter 2.

Metallocene guests: Compound **8**, $\{[(ZnI_2)_3(TPT)_2]\cdot 0.5(Fc)\cdot 0.65(C_6H_{12})\cdot 0.25(PhNO_2)\}_n$, where Fc is ferrocene, was prepared by isolating single-crystals of the parent Zn-based MOF and immersing them in cyclohexane solutions of the respective guests. The MOF crystals were placed in a test-tube from which the mother liquor was carefully decanted in a manner to keep the crystals in solution at all times. In a separate vial, 40.8 mg of ferrocene was dissolved in 3 mL of cyclohexane and subsequently added to the MOF crystals. The test-tube was sealed and placed in an oven at 50 ^{o}C for a period of 5 days. The initially colorless MOF crystals turned dark-red and were immediately subjected to single-crystal X-ray diffraction when removed from solution. Selected IR (cm^{-1}): 3050 (w), 1617 (w), 1574 (w), 1514 (s), 1421 (w), 1372 (m), 1314 (m), 1212 (w), 1099 (w), 1058 (m), 1025 (m), 868 (w), 803 (s), 751 (w), 733 (w), 668 (m), 655 (s). NMR ^{1}H (DMSO, 400 MHz): δ 4.11 (s, ferrocene), 7.65 (d, $PhNO_2$), 7.82 (t, $PhNO_2$), 8.21 (d, $PhNO_2$), 8.62 (d, TPT), 8.92 (d, TPT). Compound **9**,$\{[(ZnI_2)_3(TPT)_2]\cdot 2.5(FcCHO)\cdot 1(C_6H_{12})\cdot 1(C_6H_6)\}_n$, where FcCHO is ferrocene carboxaldehyde, was obtained through a similar procedure as compound **8**. The difference arises from the modification of the solvent mixture; ferrocene carboxaldehyde (30 mg) was dissolved in 2 mL of cyclohexane and 2 mL of benzene. This yielded dark-red crystals suitable for X-ray diffraction. Selected IR (cm^{-1}): 2968 (w), 2924 (w), 1679 (w), 1624 (w), 1618 (w), 1575 (w), 1510 (m), 1421 (w), 1373 (m), 1314 (w), 1245 (w), 1213 (w), 1108 (w), 1058 (m), 1035 (w), 1025 (m), 803 (s), 733 (w), 655 (s), 527 (w). NMR ^{1}H (DMSO, 400 MHz): δ 4.25 (m, FcCHO), 4.55 (t, FcCHO), 4.75 (d, FcCHO), 7.37 (s, benzene), 8.63 (d, TPT), 8.92 (d, TPT), 9.96 (s, FcCHO).

Organic guests: The selected organic molecules have the additional advantage of being liquids at room temperature, and hence do not require any solvents for their dissolution. Compound **10**, $\{[(ZnI_2)_3(TPT)_2]\cdot 4.2(C_8H_{10})\}_n$, and compound **11**, $\{[(ZnI_2)_3(TPT)_2]\cdot 2.5(C_8H_8)\}_n$, were obtained in similar fashion as compound **8**, however the Zn-based MOF crystals were put directly in 3 mL of ethylbenzene and 3 mL of styrene, respectively. No visible change in the color of the crystals could be observed. Compound **10** selected IR (cm^{-1}): 3028 (w), 2967 (w), 2933 (w), 1618 (w), 1575 (w), 1510 (m), 1496 (w), 1453 (w), 1421 (w), 1373 (m), 1314 (w), 1213 (w), 1108 (w), 1058 (m), 1025 (m), 803 (s), 746 (w), 733 (w), 697 (w), 655 (s), 527 (w). NMR ^{1}H (DMSO, 400 MHz): δ 1.18 (t, ethylbenzene), 2.59 (m, ethylbenzene), 7.25 (m, ethylbenzene), 8.63 (d, TPT), 8.92 (d, TPT). Compound **11** selected IR (cm^{-1}): 3060 (w), 3027 (w), 1630 (w), 1618 (w), 1575 (w), 1510 (m), 1496 (w), 1449 (w), 1421 (w), 1373 (m), 1314 (w), 1213 (w), 1108 (w), 1058 (m), 1025 (m), 992 (w), 803 (s), 777 (w), 733 (w), 698 (w), 655 (s), 527 (w). NMR ^{1}H (DMSO, 400 MHz): δ 5.13 (d, styrene), 5.74 (d, styrene), 6.64 (m, styrene), 6.68 (t, styrene), 7.12 (d, styrene), 7.30 (t, styrene), 8.63 (d, TPT), 8.92 (d, TPT).

4.2.2 Physical measurements

Infrared spectra were recorded with a Varian 640 FTIR spectrometer equipped with an ATR in the 500–4000 cm^{-1} range.

4.2.3 Single Crystal X-ray Diffraction Studies

The single-crystal samples were mounted on thin glass fibers using paraffin oil. Prior to data collection, the crystals were cooled to 200 K. Data were collected on a Bruker AXS KAPPA single-crystal diffractometer equipped with a sealed Mo tube source (wavelength 0.71073 Å) APEX II CCD detector. Raw data collection and processing were performed with APEX II software package from BRUKER AXS.

4.3 Results and discussion

4.3.1 Synthesis

As-synthesized single-crystals of the zinc-based MOF contain nitrobenzene as guest molecules, and according to previous work by Fujita *et al.*,[13] such molecules would prevent the diffusion of target compounds into the pores owing to the strong *π*–*π* interactions between the nitrobenzene solvent molecules and the triazine-based ligand. The exchange of nitrobenzene by cyclohexane is therefore recommended, however, it was found that this additional step was unnecessary for the inclusion of the guests in compounds **8–11**. In the case of ethylbenzene and styrene, the MOF crystals were soaked in neat target guest molecules for the inclusion experiments. This process is strongly advised in order to ensure that a sufficient quantity of guests are incorporated in the crystal, otherwise poor data quality or low occupancy may lead to difficulties in locating and modeling the desired guest. It also serves to reduce the competition between a solvent molecule and the guest to be included in the pores of the MOF.

Table 9: Summary of the crystal structure data and refinement for compounds **8–11**.

Complex	**8**	**9**	**10**	**11**
Formula	$C_{46.4}H_{38.05}Fe_{0.5}I_6N_{12.25}O_{0.5}Zn_3$	$C_{151}H_{121}Fe_5I_{12}N_{24}O_5Zn_6$	$C_{278.3}H_{262.12}I_{24}N_{48}Zn_{12}$	$C_{72}H_{60}I_6N_{12}Zn_3$
FW, g mol^{-1}	1760.67	4545.98	8109.10	2050.83
Crystal system	monoclinic	monoclinic	monoclinic	monoclinic
Space group	*C*2/*c*	*C*2/*c*	*C*2/*c*	*C*2/*c*
T, K	200(2)	150(2)	150(2)	150(2)
a, Å	35.0063(17)	38.059(5)	35.2310(6)	35.3123(13)
b, Å	15.0958(7)	14.2182(11)	14.6393(3)	14.8552(3)
c, Å	30.2162(15)	34.848(6)	30.5671(7)	31.1739(13)
α, °	90	90	90	90
β, °	102.0881(19)	110.753(16)	100.253(2)	101.267(4)
γ, °	90	90	90	90
V, Å^3	15 613.6(13)	17 634(4)	15 513.5(5)	16 037.8(10)
Z	8	4	2	8
ρ_{calcd}, g cm^{-3}	1.498	1.712	1.736	1.699
μ (Mo, Kα), mm^{-1}	3.408	3.353	3.354	3.245
reflns collected	14 028	11 265	12 855	10 689
*R*1, *w*R2 (I > 2 σ (*I*))[a]	0.0807, 0.2359	0.0490, 0.0782	0.0426, 0.0471	0.0531, 0.0751
*R*1, *w*R2 (all data)	0.1060, 0.2556	0.1181, 0.1313	0.1227, 0.1264	0.1476, 0.1613

[a] $R = R1 = | |F_o| - |F_c|/|F_o|$; $wR2 = \{[w(F_o - F_c^2)^2] / [w(F_o^2)^2]\}^{1/2}$; $w = 1/[\sigma_2(F_o^2) + (ap)^2 + bp]$, where $p = [\max(F_o^2, 0) + 2 F_c^2]/3$; and $Rw = [w(|F_o| - | F_c|)^2 /w|F_o|^2]^{1/2}$, where $w = 1 / \sigma^2(|F_o|)$.

4.3.2 Ferrocene inclusion

It is worth noting that the selection of ferrocene as the organometallic guest species facilitates the confirmation of successful guest inclusion. The diamagnetic nature of the Zn-based MOF and of the low-spin iron centers in ferrocene permits characterization by NMR.

Consequently, the crystals were first analyzed through ^{1}H NMR. Following the soaking procedure, the crystals were then washed with a small amount of cyclohexane in order to remove any adsorption that would have occurred at the surface of the material. The ^{1}H NMR spectra of **8** is shown in Appendix G, confirming the uptake of ferrocene. The signals of the framework are not shifted, we observe the same two peaks corresponding to the TPT ligand at 8.92 and 8.62 ppm. Moreover, the signal of the Cp-rings, contained in ferrocene, is clearly identifiable at 4.11 ppm.

The results of the single-crystal X-ray measurements for **8** are summarized in Table 9. The successful solution and refinement of the structure revealed that there is approximately one ferrocene molecule per formula unit of the MOF exhibiting an occupancy of 50%. The symmetry of the unit cell remains the same, even with the incorporation of a new guest, and is best defined by the space group $C2/c$. The contraction of the a-axis (from 36.079(10) Å to 35.0063(17) Å) is accompanied by a 3.7% decrease in the unit cell volume, compared to the as-synthesized framework containing exclusively nitrobenzene solvent molecules. The relatively low ferrocene content can be partly explained by the competition between ferrocene and cyclohexane to be included in the porous framework. It is strongly expected that a more saturated solution of ferrocene in cyclohexane would help improve the content of the metallocene in the MOF, as would an increase in temperature for the soaking procedure. Nevertheless, the ferrocene molecules are well-defined and we can confirm that the uptake of metallocenes using the Zn-based MOF, **4**, is possible. Due to the presence of an inversion center, which resides near the middle of the channels of the MOF, there is only one crystallographically-independent ferrocene guest. Visualization of a single pore of the MOF reveals that there are two ferrocene molecules in close proximity to one another, with the closest Fe–Fe distance of 6.01 Å (Figure 37).

The crystalline sponge's ability to easily uptake guest molecules is displayed in compound **8** by only leaving a 3.9 % void volume following the inclusion of ferrocene. Careful inspection of the ferrocene guest reveals that the Cp-rings are almost eclipsed by one another. The average Fe–C and C–C distances for ferrocene were calculated to be 2.03 and 1.39 Å, respectively, which are very close to the expected values of 2.04 and 1.40 Å, respectively (Table 10).

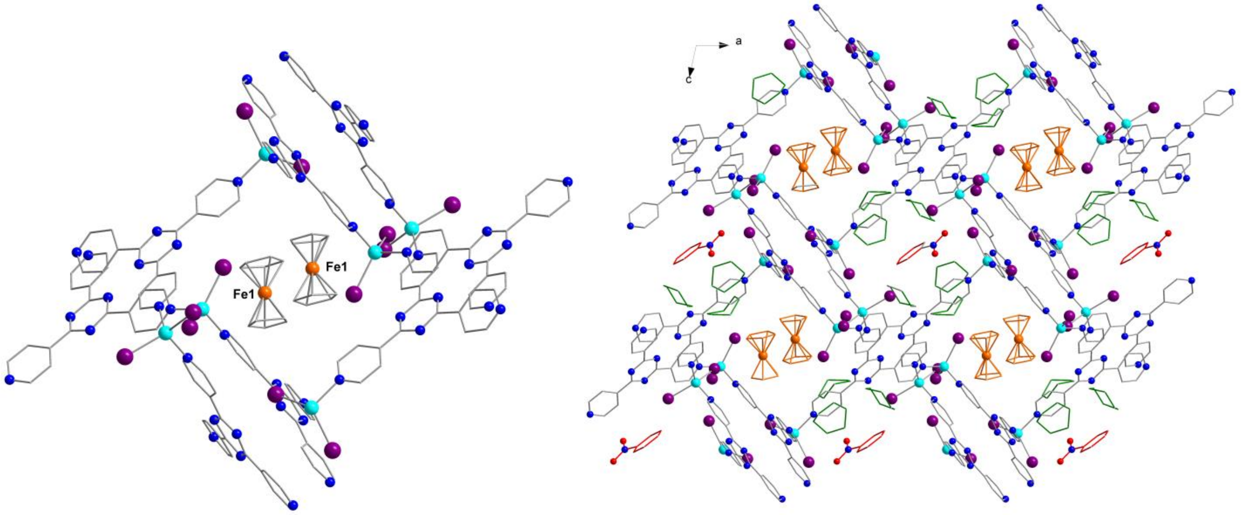

Figure 37: A view of two ferrocene molecules placed in the middle of the pores (left) and packing arrangement of **8** with the different guests molecules highlighted in different colors (right). Guest color coding: orange (ferrocene), red (nitrobenzene), green (cyclohexane). Disordered molecules and hydrogen atoms are omitted for clarity.

Table 10: Bond distances of ferrocene in compound **8**.

Fe–C bonds (Å)					
Fe1–C37	2.06	Fe1–C41	1.97	Fe1–C45	2.01
Fe1–C38	2.01	Fe1–C42	2.05	Fe1–C46	2.04
Fe1–C39	2.00	Fe1–C43	2.06		
Fe1–C40	2.04	Fe1–C44	2.01		
C-C bonds (Å)					
C37–C38	1.34	C37–C41	1.27	C45–C46	1.45
C38–C39	1.31	C42–C43	1.45	C46–C42	1.33
C39–C40	1.58	C43–C44	1.42		
C40–C41	1.34	C44–C45	1.38		

The slight distortion of the ferrocene molecule is evidenced by an angle of 2.32° between the planes of the Cp-rings. It is also interesting to note that the ferrocene guests are aligned nearly perpendicularly to the *b*-axis without *π*-stacking to the TPT ligand, however the existing short contacts of 3.58 and 3.64 Å between the Cp-ring and the pyridyl groups of TPT must be noted. The experimental procedure was replicated for cobaltocene, in the hope of obtaining a paramagnetic guest, however following numerous attempts to confirm guest inclusion crystallographically, no cobaltocene could be confirmed.

4.3.3 Ferrocene carboxaldehyde inclusion

Due to the success of ferrocene inclusion, we were interested in applying the same strategy to ferrocene carboxaldehyde since it carries a reactive functional group useful for a number of organic reactions.[14] The presence of ferrocene carboxaldehyde in the channels of the MOF were first confirmed by ^{1}H NMR spectroscopy after suitable washings with cyclohexane to remove any surface adsorption. As with compound **8**, the signals of the framework are not shifted; the two peaks corresponding to the TPT ligand are located at 8.63 and 8.92 ppm. The four signals corresponding to ferrocene carboxaldehyde (3 from the Cp-rings and 1 from the aldehyde group) are clearly defined.

The single-crystal X-ray structure is best refined in the *C*2/*c* space group and therefore, the symmetry of the as-synthesized MOF remains the same. While compound **8** only saw a minimal amount of ferrocene inclusion, the crystal structure of **9** reveals 5 ferrocene carboxaldehyde molecules per chemical formula. In fact, 3 crystallographically independent ferrocene carboxaldehyde guests can be identified (Figure 38), with Fe1 and Fe2 exhibiting full occupancies, while Fe3 is 50% occupied. It important to note that the ferrocene carboxaldehyde molecule corresponding to Fe2 is positionally disordered over two positions. This large increase in metallocene guests content is accompanied by a non-negligible increase of the unit cell volume from 16 217(8) to 17 634(4) Å^3, displaying the breathable nature of the MOF. This behavior was also demonstrated with the encapsulation of iodine, and is one of the key components for the exceptional versatility of the MOF towards guest inclusion.

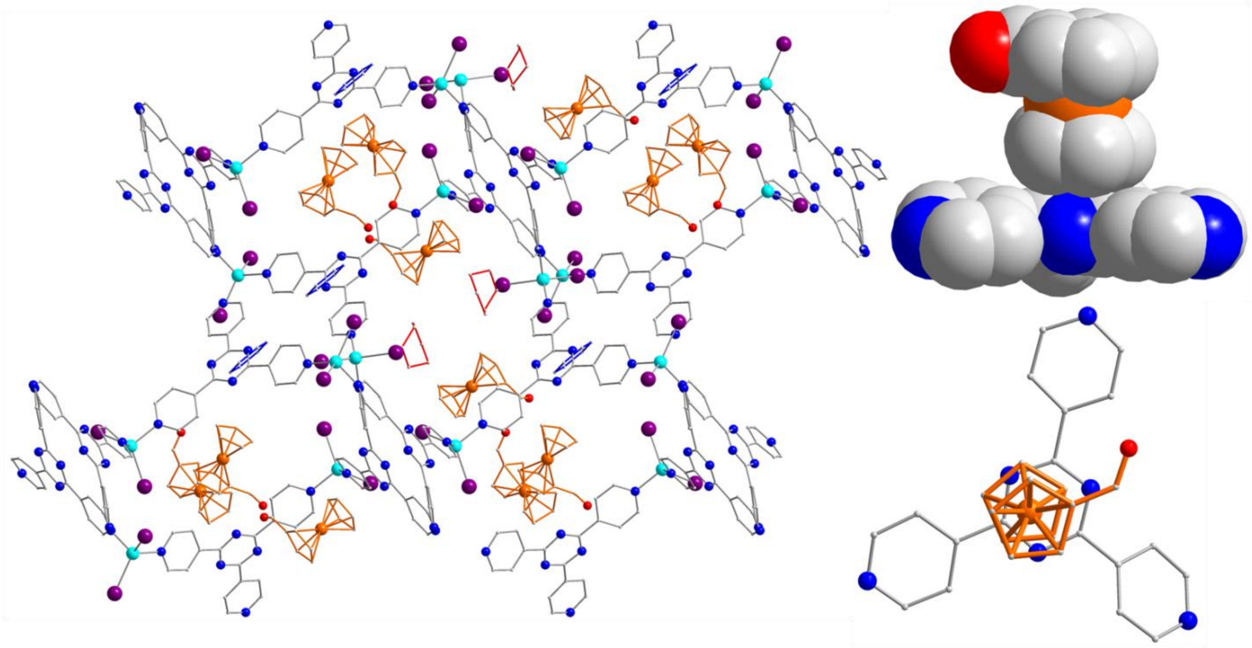

Figure 38: Packing arrangement of **9** along the *b*-axis (left) demonstrating the various guest molecules. Space-filling and ball-and-stick models illustrating the π-stacking of ferrocene carboxaldehyde with the TPT ligands (top and bottom right). Bond color coding: orange (ferrocene carboxaldehyde), red (cyclohexane), blue (benzene). Disordered molecules and hydrogen atoms are omitted for clarity.

The structure of **9** is in contrast to **8** where π-stacking of the metallocene guests with the triazine rings of the TPT ligand was observed. We can surmise that an increase in metallocene guest content results in their displacement towards the MOF framework to generate stronger interactions and provide additional spacing. While ferrocene carboxaldehyde takes up a significant portion of the channels, the remaining available void space is completed by 2 molecules of cyclohexane and 2 molecules of benzene (per chemical formula), leaving only 8.5% of the unit cell volume available for further uptake. The Cp-rings of the ferrocene carboxaldehyde guest molecules are very nearly eclipsed by one another. The average Fe−C and C−C bond distances for the aforementioned guest are 2.02 and 1.41 Å, respectively, and hence do not deviate much from their expected values even with the π−π interactions. We are currently investigating the reactivity of ferrocene aldehyde in the nanopores of the MOF.

4.3.4 Ethylbenzene and styrene inclusion

While the inclusion of metallocenes paved the way for interesting magnetic studies, the inclusion of organic guests can be just as fascinating, where the channels or pores of the MOF can be used as "microreactors". Indeed, we were intrigued by the potential of inducing polymerization inside the channels of a MOF, which in turn would alter the physical properties of the polymer itself. The idea of in-situ polymerization was evidenced following the successful incorporation of ethylbenzene, a simple aromatic compound. The structural similarity between ethylbenzene and styrene, the precursor to polystyrene, lead us investigate these two benzene-based compounds. In similar fashion to the metallocenes, ethylbenzene and styrene both contain aromatic rings, permitting favorable interactions with the MOF host, through π−π stacking with the TPT ligand. Spectroscopic analysis of crystals of **11** reveal easily identifiable peaks corresponding to the organic guest (Appendix H). The ^{1}H NMR peaks corresponding to the TPT ligand have not significantly shifted.

For compounds **10** and **11**, there are approximately 4.20 ethylbenzene and 2.50 styrene guest molecules per chemical formula, respectively, testifying to the efficacy of soaking procedures carried out in pure guests. There is also the notable absence of any solvent molecules for both inclusion compounds. From a crystallographic point of view, nitrobenzene resembles ethylbenzene and styrene, and therefore correct assignment of guest molecules may be challenging, however the nitro moiety of nitrobenzene would contain significant electron density compared to the two other guests, facilitating the refinement procedure. Hence, proper assignment of the electron densities contained in the void space of the MOF is ensured. As previously demonstrated with other inclusion compounds, the space group of the initial as-synthesized MOF remains the same following guest encapsulation (Table 9). The unit cell dimensions are also in a similar range which suggests that the host MOF does not have to undergo any significant structural modifications in order to accommodate ethylbenzene and styrene.

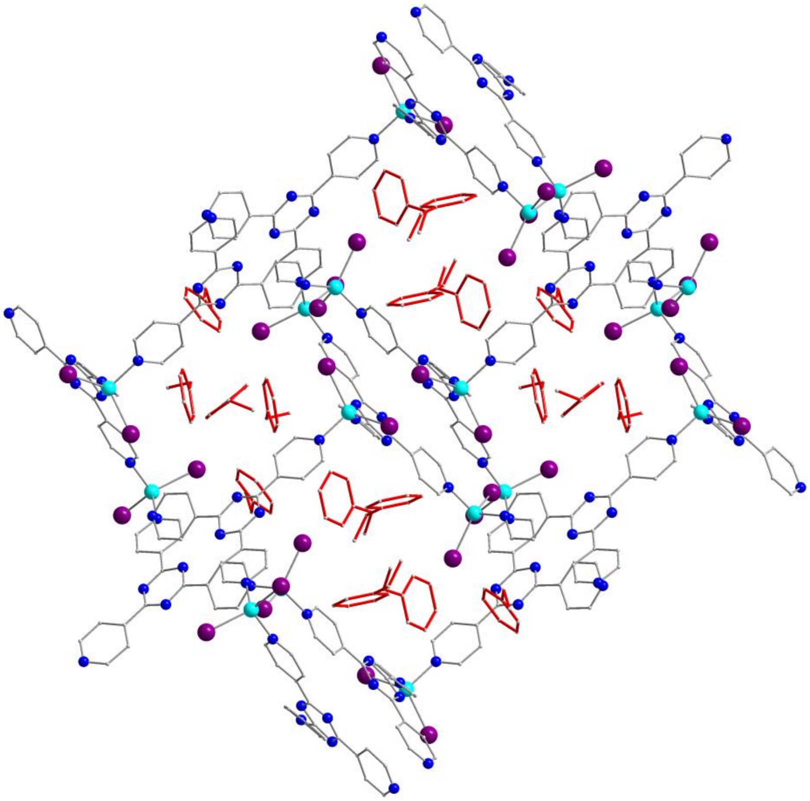

Figure 39: Packing arrangement of **10** along the *b*-axis illustrating the ethylbenzene guests in red. Molecular disorder and hydrogen atoms are omitted for clarity.

In the case of **10**, there are 5 crystallographically independent ethylbenzene molecules with four exhibiting full occupancies and one 50% partly occupied. Most interestingly, this is the first example of the present thesis where guest inclusion results in 0% of the unit cell volume being available. Therefore, the MOF is essentially saturated with ethylbenzene (Figure 39). It is equally important to note that the only significant short-contacts are between the ethyl "arms" of two ethylbenzene guests and that no π–stacking interations are observed. The closest intermolecular distance between ethylbenzene guests is between C98 and C101 at 2.30 Å.

The arrangement of the styrene guests in **11** are similar to ethylbenzene in **10**. There are 5 crystallographically independent styrene molecules, however, only two display full occupancies, for a total of 2.5 styrene molecules per chemical formula. The location of the styrene guests result in 0% of the unit cell volume being available for further uptake. The host framework remains unaltered, with minimal changes in the unit cell dimensions and subsequently, remains in the *C*2/*c* space group (Table 9). As with **10**, the styrene guests do not participate in π–π interactions with the TPT ligands, and only short contacts between the ethylene groups of two styrene molecules are clearly identified (Figure 40).

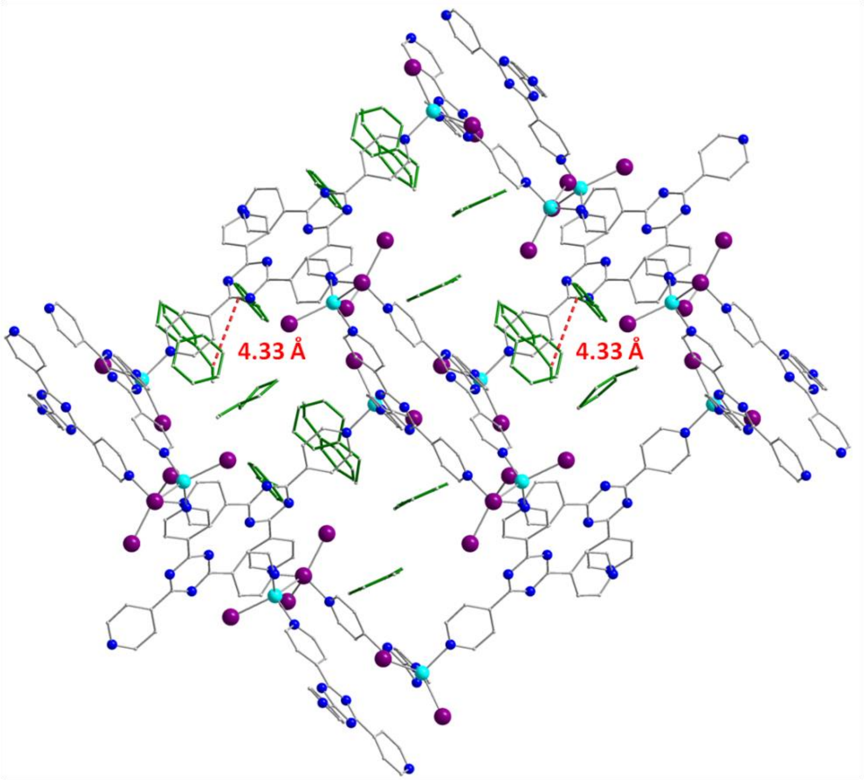

Figure 40: Packing arrangement of **11** along the *b*-axis illustrating the styrene guests in green and the closest intermolecular short contacts. Molecular disorder and hydrogen atoms are omitted for clarity.

4.4 Conclusion

In conclusion, we have successfully demonstrated the inclusion of two metallocene guests, along with two organic compounds, into a microporous Zn-based metal-organic framework. These preliminary results, based on structural analyses, provide important insights and confirm the potential for more in-depth studies involving physical properties. More specifically, the inclusion of organometallic species, which are presently the leading candidates in generating high energy barriers for slow relaxation of the magnetization, are under intense investigation following the encapsulation of the archetype Mn_{12} SMM in a MOF. It would be of high interest to the magnetic and materials community to see how such molecular species behave inside the nanopores of MOFs under various conditions.

4.5 References

[1] (a) Li, J.-R.; Kuppler, R. J.; Zhou, H.-C. *Chem. Soc. Rev.* **2009**, *38*, 1477. (b) Britt, D.; Furukawa, H.; Wang, B.; Glover, T. G.; Yaghi, O. M. *PNAS* **2009**, *106*, 20637. (c) Dybtsev, D. N.; Chun, H.; Yoon, S. H.; Kim, D.; Kim, K. *J. Am. Chem Soc.* **2004**, *126*, 32.

[2] (a) Lee, J. Y.; Farha, O. K.; Roberts, J.; Scheidt, K. A.; Nguyen, S. T.; Hupp, J. T. *Chem. Soc. Rev.* **2009**, *38*, 1450. (b) Schlichte, K.; Kratzke, T.; Kaskel, S. *Microporous Mesoporous Mater.* **2004**, *73*, 81. (c) Horike, S.; Dincă, M.; Tamaki, K.; Long, J. R. *J. Am. Chem. Soc.* **2008**, *130*, 5854.

[3] (a) Horcajada, P.; Serre, C.; Vallet-Regí, M.; Sebban, M.; Taulelle, F.; Férey, G. *Angew. Chem.* **2006**, *118*, 6120. (b) Rocca, J. D.; Liu, D.; Lin, W. *Acc. Chem. Res.* **2011**, *44*, 957.

[4] (a) Xie, Z.; Ma, L.; deKrafft, K. E.; Jin, A.; Lin, W. J. Am. Chem. Soc. 2009, 132, 922. (b) Chen, B.; Wang, L.; Xiao, Y.; Fronczek, F. R.; Xue, M.; Cui, Y.; Qian, G. *Angew. Chem., Int. Ed.* **2009**, *48*, 500.

[5] Inokuma, Y.; Yoshioka, S.; Ariyoshi, J.; Arai, T.; Hitora, Y.; Takada, K.; Matsunaga, S.; Rissanen, K.; Fujita, M. *Nature* **2013**, *495*, 461.

[6] (a) Meilikhov, M.; Yusenko, K.; Torrisi, A.; Jee, B.; Mellot-Draznieks, C.; Pöppl, A.; Fischer, R. A. *Angew. Chem., Int. Ed.* **2010**, *49*, 6212. (b) Meilikhov, M.; Yusenko, K.; Fischer, R. A. *Dalton Trans.* **2010**, *39*, 10990.

[7] (a) Meilikhov, M.; Yusenko, K.; Fischer, R. A. *Dalton Trans.* **2009**, 600. (b) Mazzeo, P. P.; Maini, L.; Braga, D.; Valenti, G.; Paolucci, F.; Marcaccio, M.; Barbieri, A.; Ventura, B. *Eur. J. Inorg. Chem.* **2013**, 4459. (c) Heck, R.; Shekhah, O.; Zybaylo, O.; Weidler, P. G.; Friedrich, F.; Maul, R.; Wenzel, W.; Wöll, C. *Polymers* **2011**, *3*, 1565.

[8] Kim, H.; Chun, H.; Kim, G.-H.; Lee, H.-S.; Kim, K. *Chem. Commun.* **2006**, 2759.

[9] Park, Y. K.; Choi, S. B.; Kim, H.; Kim, K.; Won, B.-H.; Choi, K.; Choi, J.-S.; Ahn, W.-S.; Won, N.; Kim, S.; Jung, D. H.; Choi, S.-H.; Kim, G.-H.; Cha, S.-S.; Jhon, Y. H.; Yang, J. K.; Kim, J. *Angew. Chem.* **2007**, *119*, 8378.

[10] (a) Ramadhar, T. R.; Zheng, S.-L.; Chen, Y.-S.; Clardy, J. *Acta Cryst.* **2015**, *A71*, 46. (b) Vinogradova, E. V.; Müller, P.; Buchwald, S. L. *Angew. Chem. Int. Ed.* **2013**, *53*, 3125.

[11] Biradha, K.; Fujita, M. *Angew. Chem. Int. Ed.* **2002**, *41*, 3392.

[12] Li, M.-X.; Miao, Z.-X.; Shao, M.; Liang, S.-W.; Zhu, S.-R. *Inorg. Chem.* **2008**, *47*, 4481.

[13] Inokuma, Y.; Yoshioka, S.; Ariyoshi, J.; Arai, T.; Fujita, M. *Nat. Protocols* **2014**, *9*, 246.

[14] (a) Rodriguez, J.-G.; Oñate, A.; Martin-Villamil, R. M.; Fonseca, I. *J. Organomet. Chem.* **1996**, *513*, 71. (b) Bucher, C.; Devillers, C. H.; Moutet, J.-C.; Royal, G.; Saint-Aman, E. *Coord. Chem. Rev.* **2009**, *253*, 21.

Chapter 5
Conclusion

5.1 Conclusion and outlook

The work presented herein aims to demonstrate the applicability and potential of the “crystalline sponge method”, a state-of-the-art technique for visualizing guest molecules in MOFs. While MOFs are well-known for their exceptional gas storage and separation properties, their applicability towards crystallography remains largely unexplored. Indeed, crystalline sponges permit the direct visualization of guests at the molecular level, providing unparalleled structural information regarding the interactions between the host and the guest. In turn, exhaustive studies on the physical properties exhibited by the MOF can be carried out, leading to higher performing materials.

In chapter 2, the stability of a crystalline sponge was assessed, which is crucial in determining whether a MOF is a suitable candidate for the “crystalline sponge method”. Our investigations led to the discovery of two key structural transformations of the parent Co-based MOF. The first transformation is induced by removing the MOF crystals from solution, resulting in the evaporation of solvent molecules, which occupied the pores of the material. Consequently, the MOF structure collapses and yields a non-porous green semi-amorphous material. During this process, the coordination environment of the cobalt metal centers changes from octahedral to tetrahedral, as evidenced by UV-Vis spectroscopy. Therefore, conventional MOF activation techniques are incompatible for this specific MOF, based on solid-state instability. The second transformation occurred by leaving the MOF crystals for an extended period of time in their mother liquors, resulting in an increase of the $Co(NCS)_2$ concentration. This increase leads to a single-crystal to single-crystal transformation, where the 3D porous network rearranges to form a stable 2D sheet-like structure. Hence, careful monitoring of the methanol layer, which contains $Co(NCS)_2$, is required to retain the integrity of the crystalline sponge. Although the Co-based MOF, **1b**, may be suitable for the incorporation of select guest compounds using proper solvent systems and conditions, the present study reveals structural transformations which would greatly affect the ability of the MOF to uptake guest molecules. To the best of our knowledge, only two crystalline sponges have been reported thus far, creating a high demand for porous MOFs with abilities to regularly order guest compounds.

Due to the instabilities of **1b** outlined in chapter 2, we focused our research efforts on the incorporation of small molecules using the more stable crystalline sponge, **4**. Chapter 3 deals with the direct visualization of a gaseous guest in the channels of a MOF permitting a comprehensive study on the interactions between the host and guest. Such studies continue to be the leading approach towards rationally improving the gas uptake capacities of porous materials due to the vital structural information that can be obtained. The difficulty lies in retaining adequate crystallinity following the inclusion of gaseous guests and often requires a flexible or breathable MOF. The Zn-based MOF displayed these features, and the stepwise uptake of molecular iodine was observed crystallographically. We successfully confirmed that chemisorption and physisorption, the two processes of adsorption, compete with one another to yield a MOF with an exceptional iodine uptake capacity. The interactions formed therein were evaluated by DFT calculations, allowing the unequivocal assignment of iodine species formed, ranging from simple I_2 to polyiodides such as I_3^- $[I_4]^{2-}$. The effect of the terminal iodide ions belonging to the host MOF on the uptake capacity of I_2 is currently under investigation, since they represent sites of chemisorption.

Chapter 4 was dedicated to laying the groundwork for future projects by demonstrating the wide variety of potential guests that can be incorporated in the selected crystalline sponge. As an example, ferrocene and ferrocene carboxaldehyde were both successfully encapsulated in the pores or channels of a MOF, demonstrating that the “crystalline sponge method” can also be applied to small organometallic and coordination complexes. This could prove to be particularly useful for magnetic studies which rely heavily on magneto-structural correlations in order to explain the observed behaviors. As an extension of this, the impact of the MOF on the physical properties of the molecular magnet could also prove to be an exciting area of research. Furthermore, the diamagnetic nature of **4** would make it an excellent MOF candidate for magnetic investigations. Other prospective areas of research include utilizing the crystalline sponges as “microreactors” for organic reactions, where the local environment of guests can be potentially controlled. The reactivity of ferrocene carboxaldehyde, which has been incorporated in a MOF, with amines is currently being investigated. Based on these results presented herein, it can be concluded that the “crystalline sponge method” provides a unique method of visualizing a wide variety of guest molecules. This process was demonstrated to be highly beneficial in assessing the interactions of gaseous substrates, particularly useful for a number of industrially relevant technologies. The design of new stable crystalline sponges, able to specifically accommodate desired guest compounds, can be envisioned. Larger pores or channels could lead to the “crystalline sponge method” being suitable for biologically active components, such as amino acid or even proteins, making such materials an extremely attractive field of study.

Appendix A

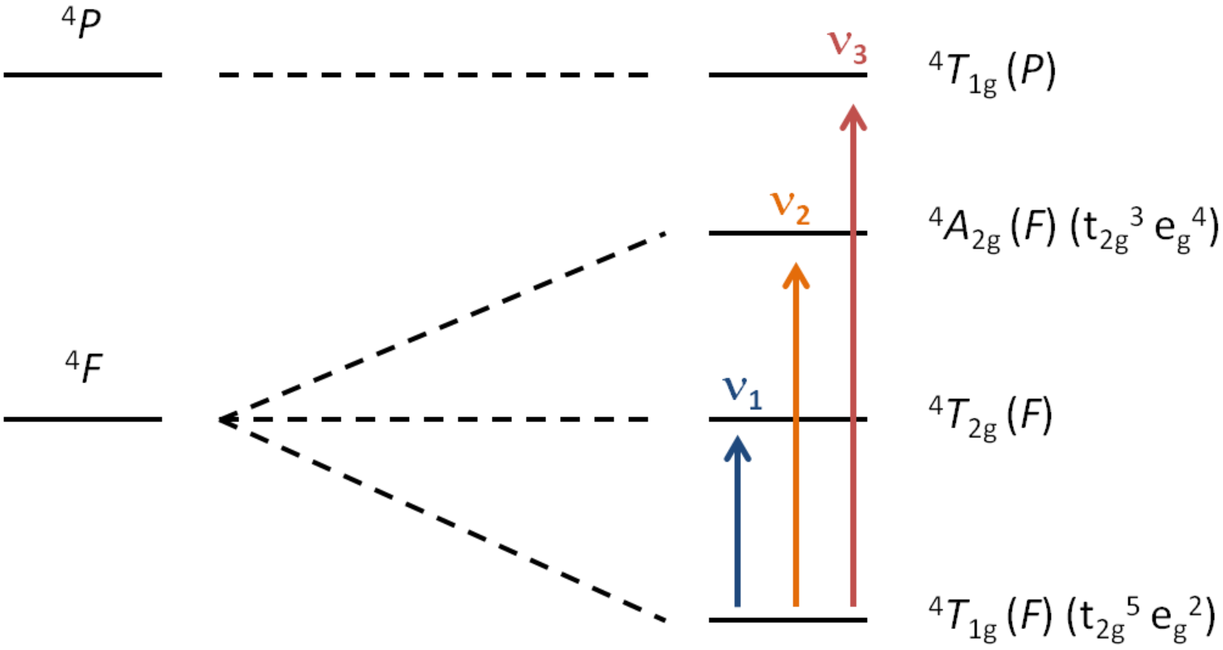

Figure A: Energy level diagram for an octahedral high-spin cobalt (II) complex and the three spin-allowed transitions.

Appendix B

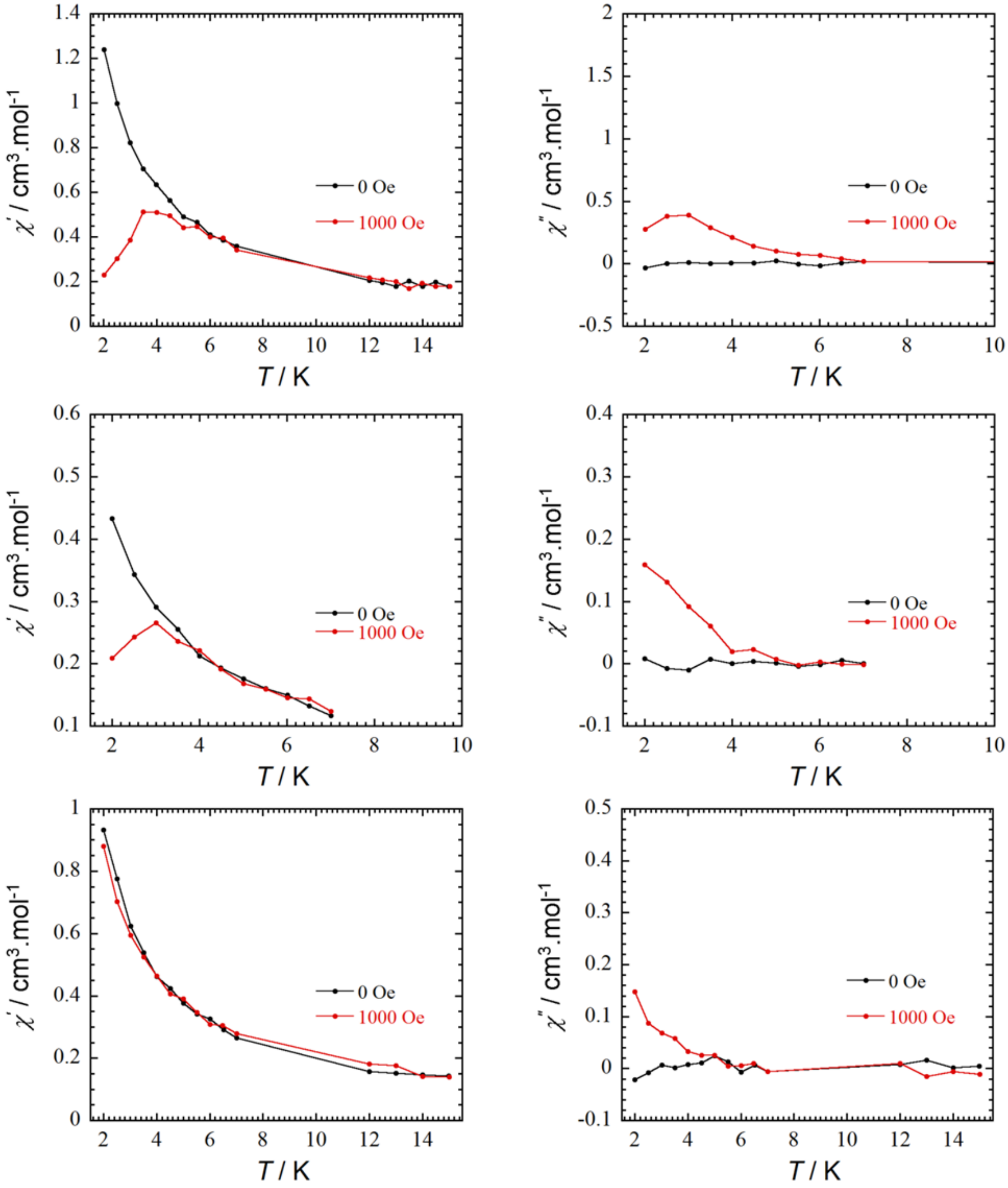

Figure B: Temperature dependence of the in-phase χ' (left) and out-of-phase χ'' (right) ac susceptibility signals under applied dc fields of 0 and 1000 Oe for compounds **1b**, **2** and **3**.

Appendix C

The initial structures for the DFT study of I_2 binding in a single pore of compounds **5** and **6** were taken from their X-ray diffraction (XRD) structures. All solvent molecules and disorder were removed from the XRD structures, along with the I_2 molecules from all pores except one. The positions of the hydrogen and iodine atoms belonging to the framework, as well as the I_2 guests, were allowed to relax, while the remaining atoms and cell vectors were fixed to the experimental XRD positions. The structure of a single pore obtained from DFT calculation of **5** is shown in the Figure C. The dihedral angle between I8–I13 and I14–I12 is close to zero, indicating that the I_2 guests are aligned towards the terminal I^- ions of the framework. The I8–I13, I14–I12, and I13–I14 distances are provided in Table C, and are in a good agreement with distances determined from XRD.

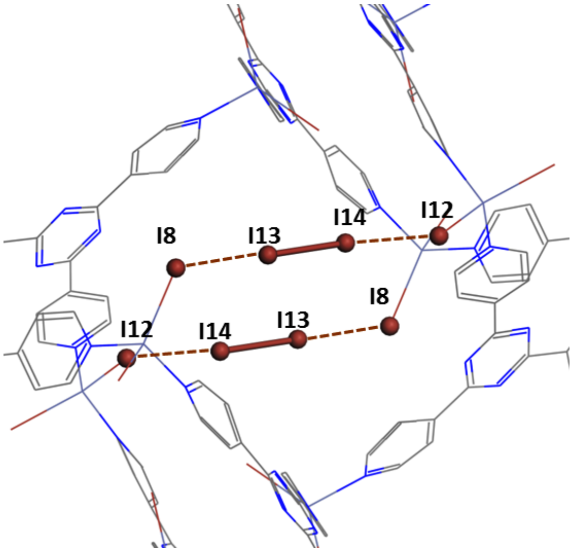

Figure C: Molecular structure of a single pore of **5** obtained from DFT calculations, emphasizing the alignment of the I_2 guest towards the terminal I^- ions of the MOF, effectively forming an $[I_4]^{2-}$ unit.

Similar calculations were performed on cases where the I_2 guests were placed perpendicular to the terminal I^- ions in the initial structures. Structural optimization resulted in the realignment of the I_2 guests along the I^- ions of the MOF. To investigate the DFT binding energy of I_2 in a single pore of **5**, DFT calculations were performed on the pore devoid of I_2

guests and using VASP to separately optimize the I_2 guest. The optimization process concerned the placement of a single I_2 molecule in an empty box, with dimensions larger than 12 Å, in order to respect the minimum image convention for I_2. Once the energies of the optimized structures were obtained, the binding energy was calculated to be 52.4 kcal/mol using the following equation:

$$E_{binding\ energy} = E_{MOF+guest} - E_{MOF} - E_{guest}$$

Table C: Assignment, occupancy, computational and experimental bond distances of iodine guests in compound **5**.

Iodine guest	**Occupancy**	**Assignment**	**Bond distances (Computational)**	**Bond distances (Experimental)**
I13–I14	1	I_4^{2-} (I8–I13–I14–I12)	I8–I13: 3.42 Å I13–I14: 2.82 Å I14–I12: 3.50 Å	I8–I13: 3.47 Å I13–I14: 2.76 Å I14–I12: 3.51 Å

Appendix D

Regarding the binding properties of I_2 in compound **6**, two configurations of the XRD structure of **6** were taken, as it included I_2 guests with different occupancies. The first configuration corresponds to a single pore of **6** containing two I_2 molecules with 88% occupancies, while the second configuration includes three I_2 molecules exhibiting 12% occupancies in the same pore. The DFT calculations for a single pore of **6** were carried out in similar fashion to compound **5**. Figure D depicts the structure of the first configuration, which was obtained from DFT calculations**.** As observed with compound **5**, the I_2 guests are in alignment with the terminal I^- ions of the framework. Bond distances for I8–I19, I19–I120 and I20–I10 are given in Table D, and are in good agreement with the distances determined from XRD. The binding energy was calculated to be 52.8 kcal/mol (26.4 kcal/mol per I_2 guest), indicating that there is a strong interaction between the I_2 guests and the terminal I^- of the framework. Figure D displays the structure of the second configuration which was obtained through DFT calculations. Although the optimized bond distance of I8–I21 is different from the one obtained through XRD, it is still in an appreciable range for $I\cdots I_2$ distances to support the formation of a chemisorbed I_3^- group. The bond distance between I23 and I10 was computed to be 3.89 Å, which is shorter than the sum of the van der Wals radii for two I atoms (4.3 Å), indicating the presence of a weak interaction between I23 and I10. To investigate the binding energy, we performed DFT calculations on the second configuration (12%) without the physisorbed I_2 molecule (I23 in Figure D), in order to quantitatively compare the two configurations. The DFT binding energy of this structure was 42.2 kcal/mol, which is 10 kcal/mol less than that of the first configuration, indicating that the formation of the $[I_4]^{2-}$ unit is more energetically favourable than an I_3^- moiety as long as no additional I_2 guests are inserted in the pore. This supports the initial formation of an $[I_4]^{2-}$ unit and a subsequent rearrangement into an I_3^- group. We also compared the energy of the first configuration with the energy of the second configuration using the equation below. The difference in the energy was calculated to be -9.6 kcal/mol, indicating that the $[I_4]^{2-}$ groups would relocate to uptake more iodine.

$$E = E_{Config2} - [E_{Config_1} + E_{I_2}]$$

$E_{Config2}$ corresponds to the energy of the second configuration that is obtained from DFT calculation (12% occupancy), while $E_{Config1}$ is the energy of the first configuration that is obtained from DFT calculation (88% occupancy). E_{I_2} represents the energy of a single I_2 molecules which accounts for balancing the number of I_2 guests in each configuration, since the second configuration has one additional guest compared to the first configuration.

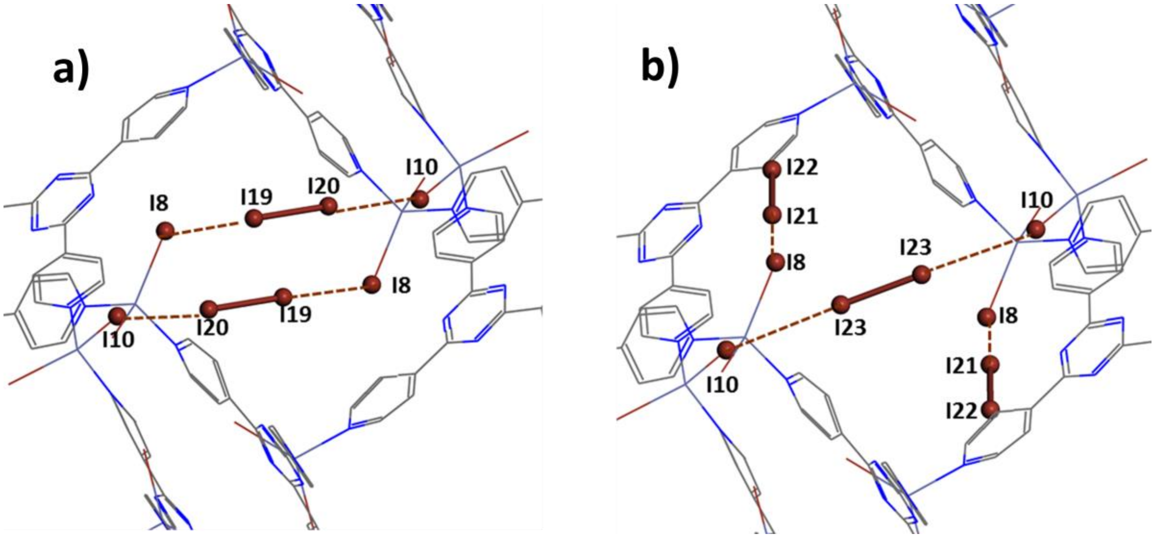

Figure D: Molecular structure of a single pore of **6** obtained from DFT calculations illustrating the two different configurations. a) I_2 guests with 88% occupancies and showing a similar $[I_4]^{2-}$ unit that was observed in **5**. b) I_2 guests with 12% occupancies, which are comprised of a chemisorbed I_3^- group along with an I_2 molecule in the middle of the pore.

Table D: Assignment, computational and experimental bond distances of iodine guests in the two configurations of compound **3**.

Iodine guest	**Assignment**	**Bond distances (Computational)**	**Bond distances (Experimental)**
I19–I20	I_4^{2-} (I8–I19–I20–I10)	I8–I19: 3.38 Å I19–I20: 2.81 Å I20–I10: 3.42 Å	I8–I19: 3.43 Å I19–I20: 2.75 Å I20–I10: 3.44 Å
I21–I22	I_3^- (I8–I21–I22)	I8–I21: 3.14 Å I21–I22: 2.79 Å	I8–I21: 2.52 Å I21–I22: 2.77 Å
I23	I_4^{2-} (I10–I23–I23–I10)	I23–I23: 2.77 Å I23-I10: 3:89 Å	I23–I23: 2.54 Å I23-I10: 4:00 Å

Appendix E

Determination of iodine content:

The following calculation was carried out in similar fashion to a previous publication regarding the uptake of iodine.[*] The density of **4** is 1.85 g/cm^3 according to the crystal data and exhibits a free volume of 60.0% giving a calculated density of I_2 of 3.09 g/cm^3. Theoretically, one gram of **4** can then uptake 1.67 g of iodine, which is consistent with the experimental data obtained by TGA (~1.73g/g).

[*] Zeng, M.-H.; Wang, Q.-X.; Tan, Y.-X.; Hu, S.; Zhao, H.-X. *J. Am. Chem. Soc.* **2010**, *132*, 2561.

Appendix F

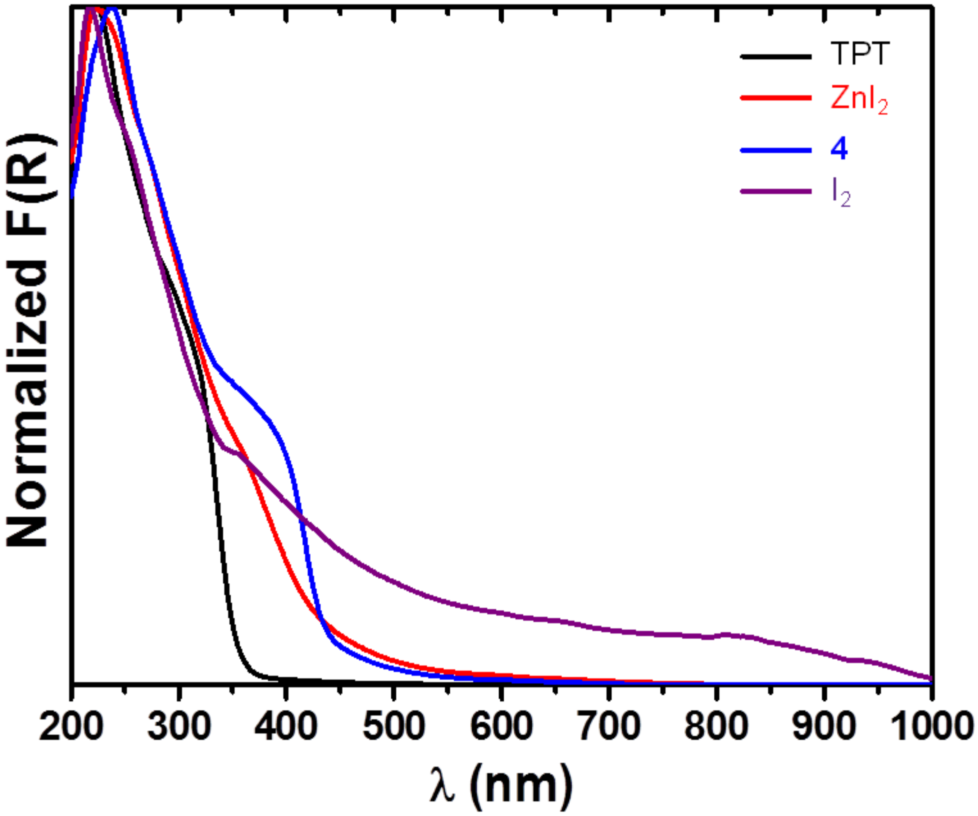

Figure E: Normalized Kubelka-Munk spectra of TPT, ZnI_2, **4** and I_2.

Appendix G

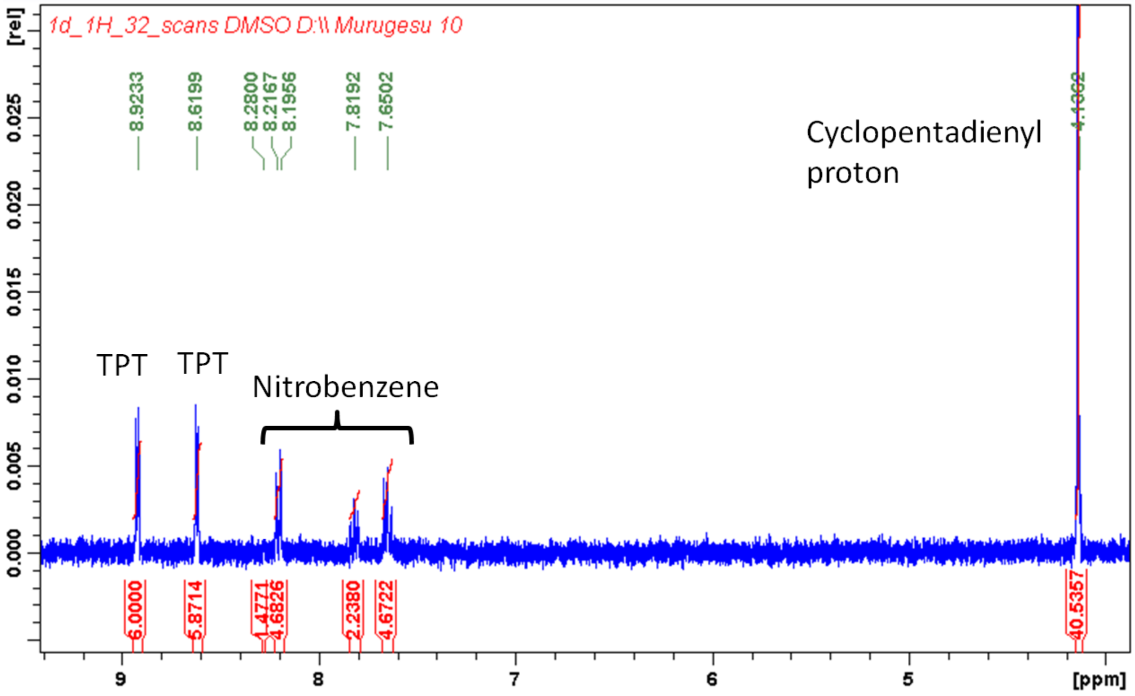

Figure G: Partial ^{1}H NMR spectra of compound **8** in DMSO. The cyclopentadienyl proton originates from the ferrocene guest.

Appendix H

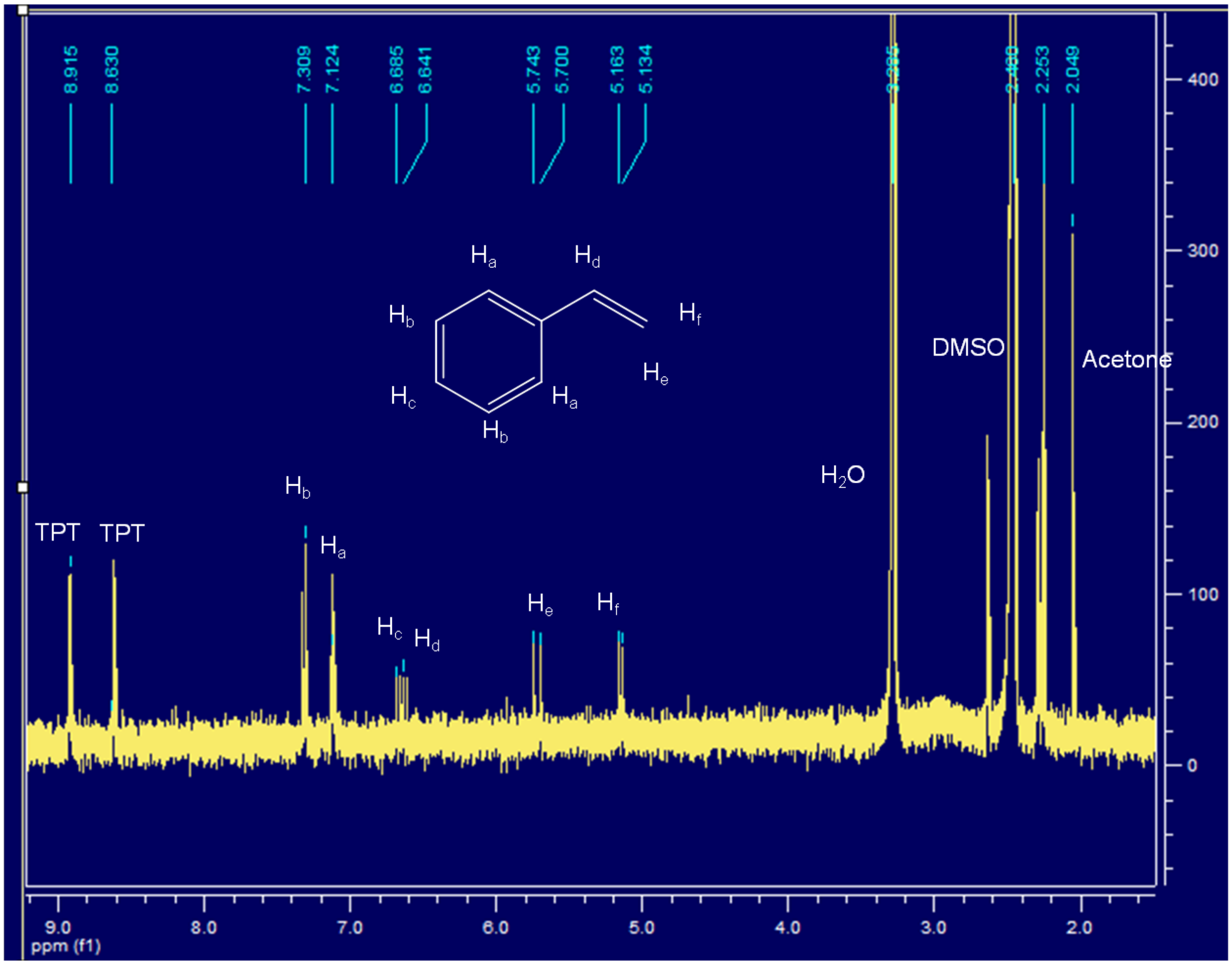

Figure G: Full ^{1}H NMR spectra of compound **11** in DMSO.